

Water purification using
zeolites prepared from clay
and ash - derived waste
materials

I V Joseph

PhD 2021

Water purification using zeolites prepared from clay and
ash - derived waste materials

IFEOMA VIRGINIA JOSEPH

A thesis submitted in partial fulfilment of the
requirements of Manchester Metropolitan University for
the degree of Doctor of Philosophy

Department of Natural Sciences
Faculty of Science and Engineering
Manchester Metropolitan University

2021

Supervisory team:

Dr. Aidan M. Doyle, Principal Supervisor

Department of Natural Sciences, Manchester
Metropolitan University

Dr. Lubomira Tosheva, Supervisor

Department of Natural Sciences, Manchester
Metropolitan University

Dr. Stuart Holmes

Department of Chemical Engineering and Analytical
Sciences, The University of Manchester

DECLARATION

I declare that this thesis has not been submitted or accepted for any other degree at any institution other than the degree of Doctor of Philosophy at the Manchester Metropolitan University.

ACKNOWLEDGEMENTS

I give thanks to God for all that happened during this research. The new things I learnt at every phase of this research and the research outputs made the whole process worthwhile.

Dr Doyle and Dr Tosheva were great supervisors who helped me stay afloat in the vast field of zeolites synthesis, characterisation, and application. I am grateful for their constructive criticism, invaluable support, insight, and their priceless contributions to my research outputs. Thank you.

The MMU John Dalton tower technical staff gave me indispensable assistance during my research. I particularly thank Dr Gary Miller for an innumerable acquisition of XRD data, Dr Hayley Andrews for particle imaging, and Dr Dave McKendry for heavy metals analysis.

My family helped me maintain my balance during this research and I appreciate their encouragements from

different parts of the world. Dr Francis Joseph (MD) fulfilled multiple long-distance roles as my brother and my unpaid 24/7 standby personal physician, *shukran habibi* for the remote doctoring. Nermine Noueihed, Anne Johnson, Patricia Williams, Julie Asumu, Elisabeth Forge, and Regina Hand, it has been an honour.

The Schlumberger Foundation provided the full financial support for this research, I am honoured to be a former employee and a part of the Schlumberger FFTF fellows.

To Him who makes it all worthwhile

LIST OF PUBLICATIONS

This thesis is based on the following publications:

Paper 1

I.V. Joseph, G. Roncaglia, L. Tosheva, A.M. Doyle, Waste Peat Ash Mineralogy and Transformation to Microporous Zeolites. *Fuel Processing Technology* 194 (2019) 106124.

Paper 2

I.V. Joseph, L. Tosheva, A.M. Doyle, Simultaneous Removal of Cd(II), Co(II), Cu(II), Pb(II), and Zn(II) Ions from Aqueous Solutions via Adsorption on FAU-Type Zeolites Prepared from Coal Fly Ash. *Journal of Environmental Chemical Engineering* 8 (2020) 103895.

Paper 3

I.V. Joseph, L. Tosheva, G. Miller, A.M. Doyle, FAU - Type Zeolite Synthesis from Clays and Its Use for the Simultaneous Adsorption of Five Divalent Metals from Aqueous Solutions. *Materials* 14 (2021) 3738.

Paper 4

I.V. Joseph, A.M. Doyle, A. Amedlous, S. Mintova, L. Tosheva, Scalable Solvent - Free Synthesis of Aggregated Nanosized Single-Phase Cancrinite Zeolite. *Manuscript in preparation.*

ABSTRACT

In this work, the synthesis of zeolites from waste materials such as coal fly ash and peat ash, as well as from natural clays was studied. Different approaches were used depending on the starting material, and the synthesis parameters were optimised for each system. The materials were characterised by X-ray diffraction (XRD), scanning electron microscopy (SEM), X-ray fluorescence (XRF), energy dispersive spectroscopy (EDS) and nitrogen adsorption isotherm measurements.

Coal fly ash was converted to zeolite X by alkali fusion at 600 °C, followed by stirring the fused material in different amounts of water and hydrothermal treatment at 80 °C. Alkali fusion was also used for the synthesis of zeolites from peat ash. Peat ash samples from both a domestic stove and an industrial boiler were investigated as raw materials for the synthesis of zeolites for the first time. The samples required pre-treatment via acid extraction to remove insoluble calcium and iron crystalline phases prior to alkali fusion. Zeolite P was prepared from pre-

treated peat ash samples, whereas zeolite A and zeolite X crystallised after the addition of sodium aluminate to the fused materials and optimising the synthesis conditions. Finally, a geophagic clay was explored as a raw material to prepare zeolites. Two approaches were used, alkali fusion followed by hydrothermal treatment or solvent-free synthesis, to prepare zeolites X and cancrinite, respectively.

The zeolites prepared were studied as adsorbents for the removal of five heavy metals in aqueous solutions. Batch adsorption studies were carried out for the simultaneous removal of cadmium (Cd), cobalt (Co), copper (Cu), lead (Pb), and zinc (Zn) from aqueous solutions to assess their performance. The general trend for the uptake of the metals by all the zeolites prepared was found to be of the decreasing order of $Pb > Cu > Cd > Zn > Co$.

TABLE OF CONTENTS

DECLARATION	IV
ACKNOWLEDGEMENTS	V
LIST OF PUBLICATIONS	VIII
ABSTRACT	X
TABLE OF CONTENTS	XII
LIST OF TABLES	XVIII
LIST OF FIGURES	XXI
LIST OF SYMBOLS AND NOTATIONS	XXVIII
1 GENERAL INTRODUCTION	1
1.1 Zeolites	1
1.1.1 Structure of zeolites	2
1.1.2 Synthesis	7
	xii

1.2	Characterisation Techniques	9
1.2.1	X-Ray Diffraction (XRD)	9
1.2.2	X-Ray Fluorescence (XRF)	12
1.2.3	Scanning Electron Microscopy (SEM)/ Energy Dispersive X-ray Spectroscopy (EDX)	13
1.2.4	Brunauer, Emmett and Teller (BET) surface area	17
1.2.5	Inductively Coupled Plasma Optical Emission Spectrometry (ICP-OES)	20
1.2.6	Transmission Emission Microscopy (TEM)	21
1.2.7	Applications	24
1.3	Zeolite Synthesis from Alternative Raw Materials	25
1.4	Fundamentals of Adsorption	27
1.4.1	Empirical adsorption isotherm equations	34
1.4.2	Adsorption kinetics	40
1.4.3	Model validation via statistical analysis	43
1.5	Removal of toxic heavy metals from water	43
1.5.1	Heavy metals removal from water using zeolites	47
1.6	Research background and motivation	49
1.7	Aims and Objectives	50
2	ZEOLITES FROM COAL FLY ASH (CFA)	53

2.1	Literature Review	53
2.2	Materials	59
2.3	Synthesis	62
2.4	Adsorption Studies	63
2.5	Results & Discussion	65
2.5.1	Characterisation of CFA	65
2.5.2	Zeolite synthesis using CFA	69
2.5.3	Nitrogen adsorption / desorption isotherms of zeolites from CFA	82
2.5.4	Simultaneous Removal of Heavy Metals	86
2.5.5	Adsorption kinetics	99
2.5.6	Adsorption isotherms	101
2.6	Conclusions	105
3	ZEOLITES FROM PEAT ASH	107
3.1	Literature Review	107
3.2	Materials	111
3.3	Synthesis	111

3.4	Adsorption Studies	114
3.5	Results & Discussion	115
3.5.1	Characterisation of peat ash samples	115
3.5.2	Acid Extraction	119
3.5.3	Alkali Fusion	121
3.5.4	GIS and LTA synthesis	123
3.5.5	FAU (NaX) synthesis	128
3.5.6	Simultaneous Removal of Heavy Metals	132
3.5.7	Adsorption isotherms	144
3.5.8	Adsorption kinetics	152
3.6	Conclusions	156
4	ZEOLITES FROM GEOPHAGICAL CLAY	158
4.1	Literature Review	158
4.2	Materials	162
4.3	Synthesis	162
4.4	Adsorption Studies	163
4.5	Results & Discussion	166
4.5.1	Characterisation of Clay	166
4.5.2	FAU - type zeolite: effects of clay pre - treatment	170

4.5.3	FAU - type zeolite: effects of ageing duration	173
4.5.4	FAU - type zeolite: effects of hydrothermal treatment	176
4.5.5	FAU - type zeolite: effects of water content and fusion temperature	180
4.5.6	FAU - type zeolite: effects of agitation during ageing	184
4.5.7	Simultaneous Removal of Heavy Metals	188
4.5.8	Adsorption kinetics	194
4.5.9	Adsorption isotherms	200
4.6	Conclusions	209
5	SOLVENT-FREE ZEOLITE SYNTHESIS	212
5.1	Literature Review	212
5.2	Materials	216
5.3	Synthesis	217
5.4	Adsorption Studies	218
5.5	Results & Discussion	220
5.5.1	Effects of NaOH	220
5.5.2	Time- and temperature- evolution	224
5.5.3	Synthesis scale-up	229
5.5.4	Simultaneous Removal of Heavy Metals	233

5.6	Conclusions	246
6	GENERAL CONCLUSIONS AND FURTHER WORK	248
6.1	General Conclusions	248
6.2	Further Work	250
	REFERENCES	252
	APPENDICES	302
	Appendix 1 (Paper 1)	302
	Appendix 2 (Paper 2)	303
	Appendix 3 (Paper 3)	304

LIST OF TABLES

Table 2-1	ASTM C618 requirements for coal fly ash [103].	54
Table 2-2	Chemical composition of CFA (mass %) [104].	55
Table 2-3	Fly ash to zeolite methods.	58
Table 2-4.	Si/Al ratios and textural results of prepared zeolites.	78
Table 2-5.	Si/Al ratios and textural characteristics of CFZ-68 samples prepared with different water content.	82
Table 2-6.	EDAX elemental analysis (mass %) of CFZ10-68 pre and post adsorption experiments for different adsorbent loadings.	98
Table 2-7.	Adsorption kinetics parameters for CFZ10 - 68 at adsorbent load of 5 g/L, $C_0= 200$ mg/L, and 90 min duration.	101
Table 2-8.	Langmuir adsorption isotherm parameters for CFZ10-68.	103
Table 2-9.	Langmuir adsorption isotherm parameters for ZRef – FAU.	104
Table 3-1.	BET surface areas and Si/Al ratio for extra synthesis step.	130
Table 3-2.	XRD oxides (mass %) of sample B FAU pre and post adsorption at 5 g/L adsorbent loading.	141
Table 3-3.	Comparison of metal uptake (%) by zeolites from coal fly ash and peat ash at initial $C_0 = 400$ mg/L, adsorbent loading of 5 g/L and 60 min duration.	143

Table 3-4. FAU-type and LTA zeolites adsorption isotherm parameters for Pb(II).	146
Table 3-5. FAU-type and LTA zeolites adsorption isotherm parameters for Cu(II).	147
Table 3-6. FAU-type and LTA zeolites adsorption isotherm parameters for Cd(II).	148
Table 3-7. FAU-type and LTA zeolites adsorption isotherm parameters for Zn(II).	150
Table 3-8. FAU-type and LTA zeolites adsorption isotherm parameters for Co(II).	151
Table 3-9. Adsorption kinetics parameters for sample B FAU.	155
Table 4-1. XRF chemical compositions (mass %) of reference zeolite (ZRef-FAU) and the optimal zeolite from clay (ZVK-FAU).	187
Table 4-2. Untreated VK clay loading variation ($C_0 = 200 \text{ mg L}^{-1}$ at 90 min) on the uptake (%) of divalent metals.	191
Table 4-3. ZVK - FAU loading variation ($C_0 = 300 \text{ mg L}^{-1}$ at 90 min) on the percentage uptake (%) of divalent metals.	194
Table 4-4. Kinetics parameters for ZVK - FAU.	198
Table 4-5. ZVK - FAU nonlinear adsorption isotherm parameters ($C_0 = 100$ to 500 mg L^{-1} at 90 min and 5 g L^{-1} adsorbent loading).	206

Table 4-6. ZRef - FAU nonlinear adsorption isotherm parameters ($C_0 = 100$ to 500 mg L^{-1} at 90 min and 5 g L^{-1} adsorbent loading).	208
Table 5-1. BET and XRD data for the scale-up experiment.	231
Table 5-2. Factorial design factors and levels.	234
Table 5-3. The removal efficiency (%) for the simultaneous uptake of five metals by CAN zeolite, $C_0 = 50$ to 400 mg/L, at 60 min and adsorbent loading of 10 g/L.	245

LIST OF FIGURES

Figure 1-1 Common zeolite <i>rings</i> [6].	4
Figure 1-2 PBU to zeolites [7].	5
Figure 1-3 SEM images of the typical morphologies of (a) FAU [11], (b) LTA [11], (c) GIS [12] , and (d) SOD [13] zeolites.	7
Figure 1-4. XRD instrument schematic [20].	11
Figure 1-5 XRD pattern of faujasite zeolite [19].	11
Figure 1-6. XRF atom excitation model [21].	13
Figure 1-7. Schematics of the SEM/EDX [23].	16
Figure 1-8 SEM micrograph of coal fly ash [14].	17
Figure 1-9. Micrometrics ASAP 2020 analyser [28].	19
Figure 1-10. ICP - OES instrument schematics [29].	21
Figure 1-11 TEM image and EDX spectrum of hematite in fly ash [30].	22
Figure 1-12. TEM equipment schematics [31].	23
Figure 1-13 Adsorption isotherms [55].	29
Figure 1-14 Types of hysteresis loops [27].	31
Figure 2-1 (a). XRD pattern and (b) SEM image of CFA. m mullite, q quartz.	67
Figure 2-2. The chemical composition of raw CFA by EDX.	68
Figure 2-3. SEM images of the evolution of NaX from CFA. (a) Raw CFA, (b) NaOH fused CFA, and (c) CFZ.	72
Figure 2-4. XRD patterns showing the crystalline phases of CFA transformation to FAU-type zeolite.	73

Figure 2-5. XRD patterns for water content of 1:4 to 1:10 and ageing duration of 24 h to 72 h.	74
Figure 2-6. SEM images of (a) CFZ4-24, (b) CFZ4-48, (c) CFZ4-68, (d) CFZ4-72, (e) CFZ10-24, (f) CFZ10-48, (g) CFZ10-68, and (h) CFZ10-72 for water content and ageing duration variation.	76
Figure 2-7. XRD patterns of samples prepared with different water contents (a) pre hydrothermal CFA and (b) zeolites CFZ.	80
Figure 2-8.(a) N ₂ adsorption/desorption isotherms (closed symbols, adsorption, open symbols, desorption) and (b) BJH Adsorption pore-size distributions of CFZ10-68, CFZ15-68, and ZRef-FAU samples.	85
Figure 2-9. The removal efficiency of raw CFA from 5 – 100 mg/L.	87
Figure 2-10. Simultaneous removal of five metals for 0 – 180 min at 5 g/L adsorbent loading and C ₀ =200 mg/L using (a) CZ10-68 and (b) ZRef-FAU.	90
Figure 2-11. Simultaneous removal of heavy metals for 100 – 500 mg/L at 90 min and adsorbent loading of 5 g/L using (a) CZ10-68 and (b) ZRef-FAU.	94
Figure 2-12. CFZ10-68 loading variation for 200 mg/L at 90 min for the simultaneous removal of five metals.	97
Figure 3-1. (a)Natural peatland and (b) stacks of peat in county Roscommon, Ireland.	108
Figure 3-2 Global peat distribution [131]	109

Figure 3-3. (a) XRD patterns and (b) SEM images of calcined samples.	118
Figure 3-4. XRD patterns of calcined and acid leached samples.	120
Figure 3-5. XRD patterns of sample A from acid leaching to NaOH fusion at different ratios.	122
Figure 3-6. XRD patterns of the zeolite products for NaOH variations of sample A. P represents GIS zeolite.	124
Figure 3-7. XRD patterns of LTA zeolites from sample A and sample B. A represents LTA, P GIS, and X NaX (FAU-type) zeolites.	126
Figure 3-8. SEM images of GIS and LTA zeolites for sample A (a and b) and sample B (c and d).	127
Figure 3-9. Sample A XRD patterns and SEM images for 0 to 4 days extra synthesis step.	129
Figure 3-10. Sample B XRD patterns and SEM images for 0 to 4 days extra synthesis step.	130
Figure 3-11. Removal efficiency at $C_0 = 100$ mg/L from 0 to 60 min and adsorbent loading of 5 g/L for (a-b) sample A LTA and FAU and (c-d) sample B LTA and FAU.	134
Figure 3-12. LTA and FAU removal efficiency at 60 min from 100 to 400 mg/L.	136
Figure 3-13. Efficacy of the simultaneous removal of five metals in aqueous solutions using sample B FAU at (a) 200 mg/L from 0 to 180 min and (b) 90 min for 100 to 500 mg/L.	137

Figure 3-14. Adsorbent loading variation for sample B FAU at 200 mg/L and 90 min.	139
Figure 4-1. 1:1 and 2:1 layer structure of clay minerals [144].	160
Figure 4-2. Characterisation of raw clay showing (a) image of clay before crushing, (b) XRD pattern of the crushed clay sample, k kaolinite, m muscovite, q quartz, and v vermiculite. The insert is the SEM image.	167
Figure 4-3. XRD pattern of the oriented clay sample oriented raw. k kaolinite, m muscovite, v vermiculite, q quartz.	168
Figure 4-4. XRD patterns and SEM images of a pure NaX phase (ZVK – FAU), a pure GIS (ZVK – P), and a mixed GIS and quartz phases (ZVK – PQ).	173
Figure 4-5. XRD patterns of FAU zeolite from VK for 24, 48, and 68 h ageing. Dashed lines represent the main FAU zeolite peaks.	174
Figure 4-6. SEM images of zeolitic products obtained at (a) 24 h ageing and (b) 48 h ageing.	176
Figure 4-7. XRD patterns of FAU zeolites from VK for hydrothermal treatment (HT) times from 0 h to 72 h. Dashed lines represent the main FAU zeolite peaks. Inserts contain SEM images of the corresponding samples.	180
Figure 4-8. XRD patterns FAU zeolites prepared using (a) fused sample to deionised (DI) water mass ratios of 1:5 to 1:15 and	

(b) different temperatures and times during the alkali fusion step. Dashed lines represent main FAU zeolite peaks.	183
Figure 4-9. XRD patterns of FAU zeolites from VK (ZVK – FAU) under stirred and static ageing. Dashed lines represent main FAU zeolite peaks.	186
Figure 4-10. Untreated VK metal uptake at 5 g.L ⁻¹ adsorbent loading for (a) C ₀ = 200 mg L ⁻¹ for 10 to 180 min and (b) C ₀ = 100 to 500 mg L ⁻¹ at 90 min.	189
Figure 4-11. ZVK – FAU simultaneous uptake of five metals at (a) 300 mg L ⁻¹ from 0 to 180 min and (b) 90 min for C ₀ =100 to 500 mg L ⁻¹ and 5 g L ⁻¹ zeolite loading.	192
Figure 4-12. ZVK – FAU nonlinear adsorption isotherms plots for the simultaneous removal of five metals at 90 min, C ₀ =100 to 500 mg L ⁻¹ and 5 g L ⁻¹ zeolite loading for (a) Pb, (b) Cu, and (c) Cd.	202
Figure 4-13. ZVK – FAU nonlinear adsorption isotherms plots for the simultaneous removal of five metals at 90 min, C ₀ =100 to 500 mg L ⁻¹ and 5 g L ⁻¹ zeolite loading for (a) Zn and (b) Co.	207
Figure 5-1. CAN zeolite viewed along 001 [175].	213
Figure 5-2. XRD patterns of synthesis (a) without NaOH at 80 °C and 180 °C, (b) with only clay and NaOH at 180 °C.	222
Figure 5-3. XRD patterns for the variation of NaOH to clay ratios. c CAN and a alunite.	224

Figure 5-4. XRD pattern intensities at location d_{101} for 180 °C from 0 to 72 h.	226
Figure 5-5. XRD pattern intensities at location d_{101} for 150 °C from 0 to 72 h.	228
Figure 5-6. (a). SEM image of optimal CAN zeolite at 40k magnification and (b). TEM image of the optimal CAN zeolite.	229
Figure 5-7. XRD patterns of scale up synthesis of CAN zeolite for 1X to 8X of the starting material.	230
Figure 5-8. N ₂ adsorption/desorption curves at -196 °C for 1X and 8X scale-up CAN zeolite, BJH pore size distribution in the insert. Opened symbols, desorption, closed symbols, adsorption. The isotherm for 8X was shifted by 150 units on the y – axis for clarity.	233
Figure 5-9. Normal probability plot for Co removal using CAN zeolite.	236
Figure 5-10. Pareto chart for Co removal using CAN zeolite.	238
Figure 5-11. Normal probability plot for Zn removal using CAN zeolite.	239
Figure 5-12. Pareto chart for Zn removal using CAN zeolite.	240
Figure 5-13. Normal probability plot for Cd removal using CAN zeolite.	240
Figure 5-14. Pareto chart for Cd removal using CAN zeolite.	241

Figure 5-15. Normal probability plot for Cu removal using CAN zeolite.	242
Figure 5-16. Pareto chart for Cu removal using CAN zeolite.	243
Figure 5-17. Normal probability plot for Pb removal using CAN zeolite.	243
Figure 5-18. Pareto chart for Pb removal using CAN zeolite.	244

LIST OF SYMBOLS AND NOTATIONS

BET	Brunauer – Emmett – Teller
BJH	Barrett, Joyner, and Halenda
CAN	Cancrinite zeolite
C_e	Equilibrium concentration
C_t	Equilibrium concentration at time t
CFA	Coal fly ash
FAU	Faujasite-type zeolite
GIS	Gismondine zeolite
ICP-OES	Inductively coupled plasma optical emission spectroscopy
K_F	Freundlich isotherm constant
K_H	Henry's law constant
k_{id}	Intraparticle diffusion rate constant
K_L	Langmuir isotherm constant
K_T	Tóth isotherm constant

k_{PFO}	Pseudo first-order kinetics rate constant
k_{PSO}	Pseudo second-order kinetics rate constant
K_{RP}	Redlich – Peterson isotherm constant
LTA	Linde type A zeolite
NaA	Linde type A zeolite
NaX	FAU type zeolite X
q_e	equilibrium sorption capacity
q_m	Maximum sorption capacity
q_t	Sorption capacity at time t
R^2	Coefficient of correlation
SEM/EDX	Scanning electron microscopy/energy dispersive X-ray spectrometry
SOD	Sodalite
TEM	Transmission emission microscopy
XRD	X-ray diffraction
XRF	X-ray fluorescence

1 GENERAL INTRODUCTION

1.1 Zeolites

In accordance with the IUPAC classification of porous materials based on their pore sizes, microporous materials have pore diameters below 2 nm, mesoporous between 2 nm and 50 nm, while macroporous materials have pore diameters above 50 nm. Zeolites are 3D aluminosilicates with ordered microporous crystalline structures and pores sizes that discriminate certain sizes of molecules. There are natural and synthetic zeolites with wide-ranging applications in the areas of adsorption, catalysis, and soil remediation. Some zeolites with commercial value include faujasites, mordenites, Linde type A, and Zeolite Socony Mobil - 5 (ZSM - 5) which belongs with the pentasil (MFI) zeolites.

The formation of natural zeolites has its origin from volcanic activities by the eruption of molten magma and the subsequent interaction of copious quantities of ash aluminosilicates with alkaline basins [1,2]. The reactions of hot lava and salty sea water over thousands of years

led to the formation of natural zeolites. On the other hand, synthetic zeolites are mainly prepared via hydrothermal processes using commercially sourced or natural raw materials as sources of aluminosilicates.

Zeolites were discovered in 1756 by the mineralogist Axel Frederik Cronstedt, who named them “zeolites” (meaning *boiling stone*) [3]. The name originates from the observation of steam upon heating a zeolite. Synthetic zeolites were developed in the 1940s and research into preparing new zeolite structures or optimising the characteristics of existing structures is continuing to date.

1.1.1 Structure of zeolites

Structurally, zeolites are composed of $[\text{SiO}_4]^{4-}$ and $[\text{AlO}_4]^{5-}$ tetrahedra with oxygen atoms connecting the tetrahedral units; extra framework cations (inorganic interchangeable cations such as Na^+ and K^+) are required to keep the structure neutral [4]. The classification of zeolites is based on their pore sizes, morphology, structure, and silicon to aluminium ratios (Si/Al). Zeolite frameworks can be differentiated by their chemical

composition, pore structure, Si/Al ratio, and the extra framework cation.

Zeolite structures are described by three-letter codes such as FAU, LTA, MFI, etc., which are not related to their chemical composition. The Zeolite Association (IZA-SC) is the body that currently approves new zeolite structures. As of 2021, there are 254 framework type codes [5].

Zeolites have primary or basic building unit (BBU), secondary building units (SBU), and composite building units (CBU) for more complex arrangements. The linking of periodic patterns of BBUs leads to many zeolite types. The BBUs are the tetrahedra in which the central atoms (like Si and Al) have low electronegativity while the atoms at the tetrahedra edges are oxygen anions (O^{2-}); the combination of the central and edge atoms are represented as $[SiO_4]$, $[AlO_4]$ or $[GeO_4]$ [6]. TO_4 is used to depict tetrahedra where T represents any of the central tetrahedra species. Linkage of BBUs give rise to non-chiral SBUs with their characteristic pores and channels, they contain up to 23 T atoms. Generally, any given unit

cell in a zeolite framework is composed of the same number of SBUs.

The simplest composite building units (CBUs) are called *rings*, zeolites are formed from a combination of rings of varied sizes; the most common ones are shown in Figure 1-1 and are 4, 5, 6, 8, 10, and 12 rings.

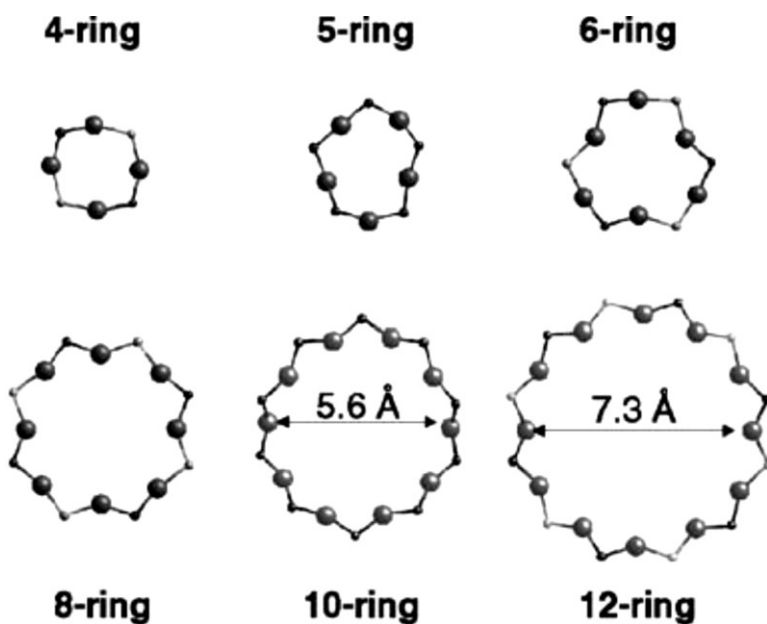


Figure 1-1 Common zeolite *rings* [6].

Larger and more complex CBUs are formed from structures containing n tetrahedral or n rings leading to the existence of cages. For example, 6 ring polyhedra have such narrow passages that only molecules smaller than water can go through [6]. The cubo-octahedron sodalite unit, also called a β cage, is a connection of 24 tetrahedra; various zeolite structures are formed from the sodalite SBU (Figure 1-2). The faujasite zeolite supercages (or α cage) are formed when sodalite units (β cages) are connected through their hexagonal faces.

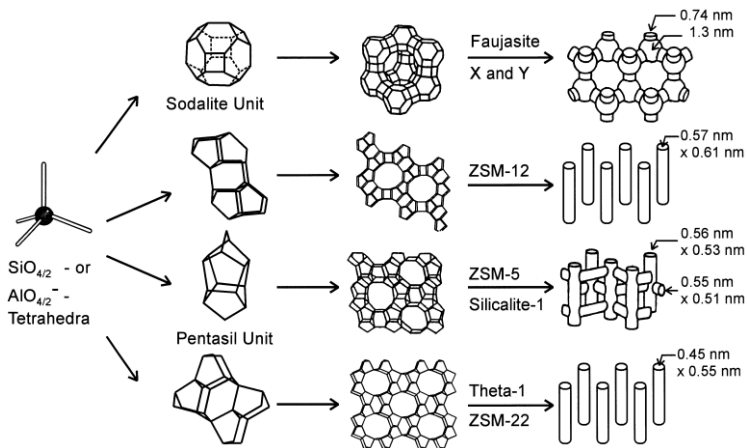


Figure 1-2 PBU to zeolites [7].

The Si/Al ratio of zeolites plays an important role in the surface properties of zeolites. The Si/Al ratio is indicative of the electronegativity of the zeolite framework; the lower the value, the more electronegative the surface is and hence a higher capacity for exchange of extra framework cations [8].

Faujasite zeolites with their characteristic octahedra morphology (Figure 1-3a) have pore diameter of 7.4 Å. The synthetic FAU-type zeolites first synthesised by Milton and Breck include zeolites X (NaX) with Si/Al ratio of 1.23 and zeolite Y (NaY) with a Si/Al ratio of 2.5 [3,8–10]. The Linde type A zeolite (LTA), also known as zeolite A, has Si/Al of ≈ 1 and a cubic crystal shape (Figure 1-3b). The synthetic analogue of the gismondine (GIS) zeolite, referred to as zeolite P or GIS, has a fibrous morphology (Figure 1-3c) with Si/Al of about 1. Sodalite (SOD), a secondary building unit upon which a myriad of zeolites are built upon by the formation of supercages, has a pore diameter of 2.3 Å and a wool-like morphology (Figure 1-3d).

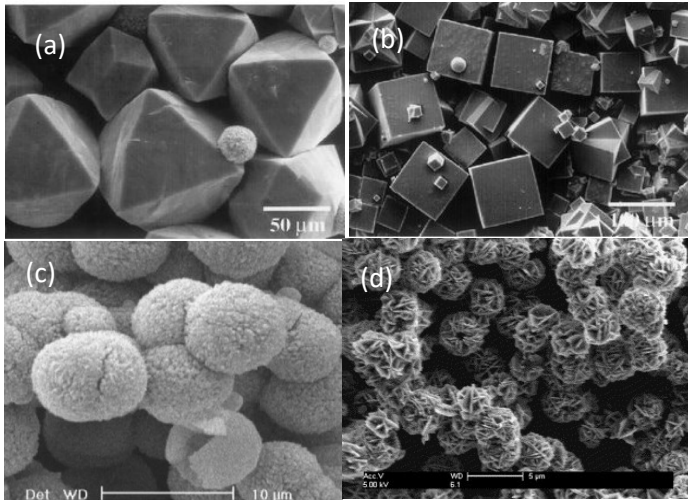


Figure 1-3 SEM images of the typical morphologies of (a) FAU [11], (b) LTA [11], (c) GIS [12] , and (d) SOD [13] zeolites.

1.1.2 Synthesis

Synthetic zeolites are generally prepared by the hydrothermal method. Within this method, variations have led to non-conventional synthesis methods like microwave assisted synthesis, sonication, and dry or molten salt processes. The type of zeolite that results from those methods depends on the variations in crucial parameters like temperature, pressure, water content,

Si/Al ratio of the starting material, precursor alkalinity, and starting materials to activation solution ratio [14].

The prerequisites for zeolite synthesis include sources of alumina and silica, in some cases organic structure directing agents (OSDAs), mineralising agents (most commonly OH^-), and solvent (water in most cases) [15,16]. Zeolites are typically synthesised at temperatures below 200 °C and autogenous pressures with varying synthesis durations [16,17].

The anions (OH^-) play an important role in the formation of silicates via the dissolution of the reactive species prior to the nucleation step [16]. Zeolite nucleation mechanism is categorised into primary and secondary nucleation. Primary nucleation could be directed by the solution (homogeneous) or catalysed by the materials in the amorphous gel formed prior to nucleation (heterogenous) [18]. On the other hand, secondary nucleation occurs as a result of added seed crystals or an in-situ crystal growth mechanically induced by shear forces in the fluid, attritive contact, and fracture which

enable the formation of crystals from the original. Nucleation is followed by crystallisation which occurs as materials are assimilated from the solution, the duration can be from a few hours to days depending on the synthesis method chosen [16,18]. Nucleation is the rate-limiting step since the crystallisation process proceeds at a fast rate once it starts [15].

1.2 Characterisation Techniques

1.2.1 X-Ray Diffraction (XRD)

In determining the crystallographic data of zeolites, the XRD is the most common technique used to identify and quantify the various phases present in the material. A reference database for the various zeolite types is published by the IZA as a collection of XRD patterns [19]. The equipment works by the bombardment of X-rays generated by a cathode ray tube onto the sample, the interactions of the incident rays with the various phases are recorded since various minerals have their signature interaction with X-rays as shown in the schematic of the XRD equipment in Figure 1-4.

These interactions produce constructive interference in accordance with Bragg's law which relates the wavelength of electromagnetic radiation (λ) to its angle of diffraction (θ) and the interplanar spacings between the lattices (d) as show in Equation 1. When the samples are scanned over a range of 2θ angles, all possible diffraction data are collected by the equipment. Thus, the diffraction of a beam of monochromatic X-rays with wavelength λ incident on parallel atomic planes with spacing d at a glancing angle of θ depend on λ and the interplanar spacing, d , which provides information on the structure.

$$2d\sin\theta = n\lambda$$

Equation 1

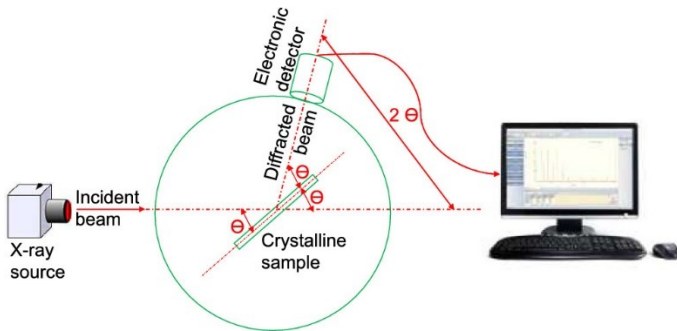


Figure 1-4. XRD instrument schematic [20].

Figure 1-5 shows a diffractogram of faujasite zeolite with the characteristic peak that starts at $6.19^\circ 2\theta$.

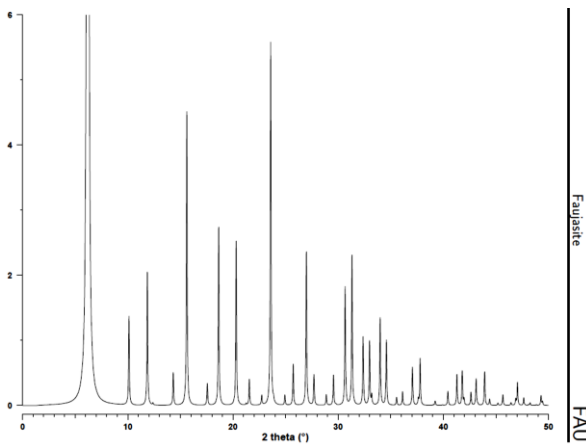


Figure 1-5 XRD pattern of faujasite zeolite [19].

1.2.2 X-Ray Fluorescence (XRF)

XRF is used for the non-destructive elemental compositional analysis of materials. The principle this equipment is based on is the energy – matter interaction of individual atoms when excited by an external energy source, emit X-ray photons with wavelength and intensity that are characteristic to each element. The excitation of atoms by a primary X-ray source in specimens involves the removal of inner shell electrons, characteristic fluorescence radiation (photons) is emitted by the outer shell electrons as they fill in the voids as shown in Figure 1-6. The elements in the specimen are identified and quantified by counting the number of photons emitted from the atoms when excited. In addition to being a non-destructive characterisation method, XRF is fast and applicable over a wide range of materials from powdered to liquid specimens.

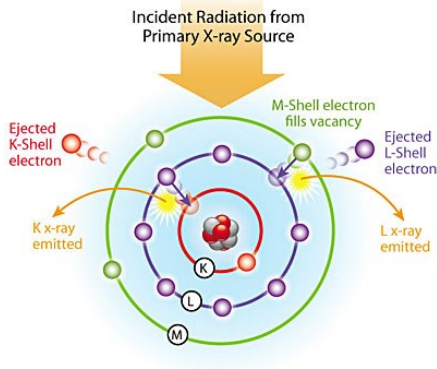


Figure 1-6. XRF atom excitation model [21].

1.2.3 Scanning Electron Microscopy (SEM)/ Energy Dispersive X-ray Spectroscopy (EDX)

Before the development of electron microscopes, light microscopes were used for imaging which have drawbacks of a maximum magnification of 1000x and the wavelength of light. These limitations were overcome using electrons. The SEM is a powerful tool in material characterisation, and it is used to obtain the topography of materials. Scanning a focused beam of electrons on a material from an area as little as 5 μm can generate a

high-resolution image of the material with magnification of up to 400,000x [22].

The components include an electron source, electron lenses, sample holding system, detectors, display unit, and additional units for power supply, vacuum system, and cooling. When the material is exposed to a beam of high kinetic energy electrons generated by an electron gun, signals are obtained when the electrons decelerate on impact with the sample with loss in kinetic energy. These signals are recorded, amplified, and displayed to give an image of the material.

The signals for imaging analysis include the secondary electrons (SE) generally used to determine the topography of the material, backscattered electrons (BSE) used in determining the distribution of elements in the material, and cathodoluminescence (CL) which provides information on structural defects [22]. The drawbacks of SEM include the requirement for specimens to be electrically conductive (some samples are coated

with gold to overcome this) and the specimen chamber need for high vacuum.

In connection with the SEM, the EDAX or EDX is used to determine the elemental composition of materials. The detector separates the signature X-rays given off by different elements into an energy spectrum which is used to obtain the abundance of each element in the material. Figure 1-7 shows the general schematic of SEM and EDX showing the locations for the electron source and the detectors for the secondary and back-scattered electrons.

The SEM image of coal fly ash is shown in Figure 1-8, here the morphology of the material can clearly be seen at 20,000x magnification.

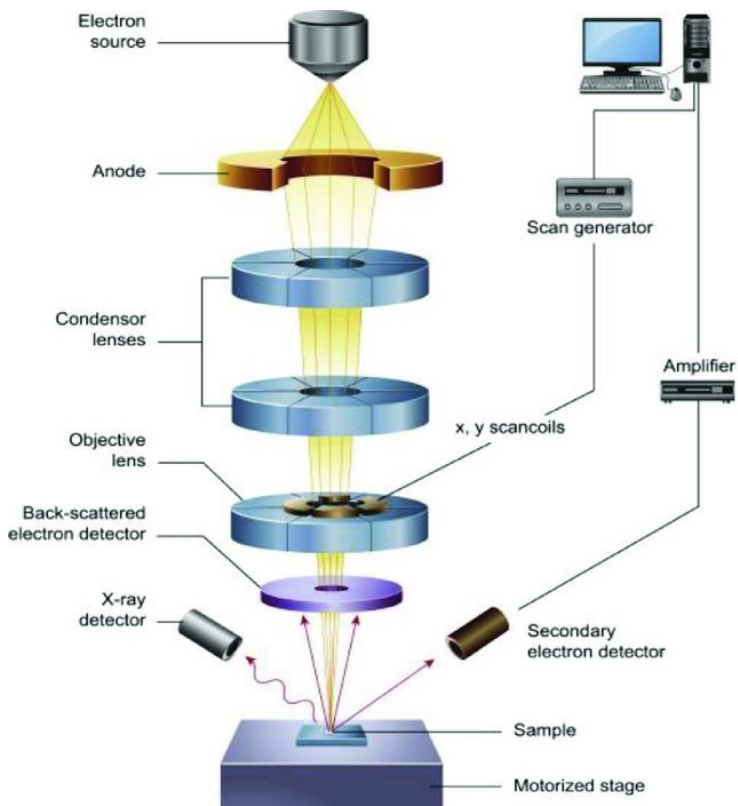


Figure 1-7. Schematics of the SEM/EDX [23].

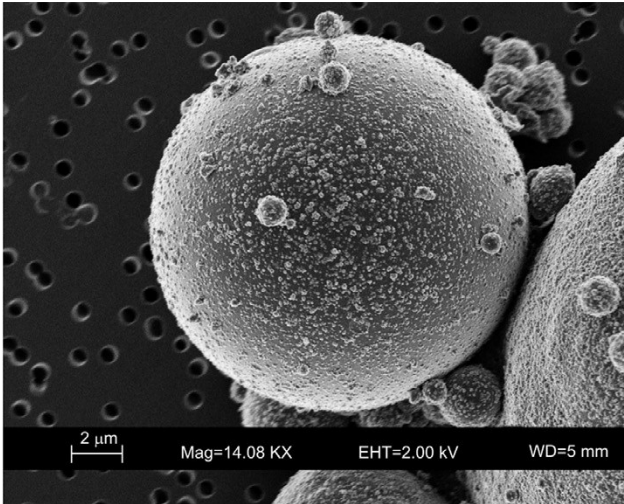


Figure 1-8 SEM micrograph of coal fly ash [14].

1.2.4 Brunauer, Emmett and Teller (BET) surface area

The BET method developed by Stephen Brunauer, Paul Emmett, and Edward Teller is typically used to measure the surface area of materials. It typically involves measurements of the adsorption of nitrogen at $-196\text{ }^{\circ}\text{C}$, the boiling point of nitrogen at atmospheric pressure, unto a carefully weighed powdered sample, at different relative pressures. The volume of the adsorbed gas on

multilayers of the sample is used to correlate to the total surface area of the material.

Brunauer, Emmett, and Teller hypothesised that the Langmuir theory of monolayer can still be applied for every layer, the adsorption of gas molecules on a solid is continuous, and there exists an interaction of the gas molecules in adjacent layers. The linear form of the BET equation for multilayer adsorption is given in Equation 2 [24,25] as:

$$\frac{P}{n(P^0-P)} = \frac{1}{n_m C} + \frac{C-1}{n_m C} \left(\frac{P}{P^0} \right) \quad \text{Equation 2}$$

where p and p^0 represent the equilibrium and saturation pressure of the adsorbate, n is the adsorbed amount, n_m represents the monolayer capacity, and C is the BET constant.

Measurement of the surface area (Figure 1-9) using the BET method is specified by the International Standard Organisation standard ISO 9277:2010, a revised standard (ISO/DIS9277) is currently under review [26]. The ISO 9277:2010 specifies the determination of the overall

specific and internal surface areas for porous materials via the adsorption of nitrogen using the BET method. The BET specific surface area (S , m^2/g) of the adsorbent is given by Equation 3 [27].

$$S = \frac{n_m \cdot L \cdot \sigma_m}{m \cdot V_0} \quad \text{Equation 3}$$

where n_m is the monolayer capacity, L is the Avogadro constant, σ_m is the area occupied by the adsorbate, m is the mass of the adsorbent, and V_0 is the molar volume of the gas at STP.

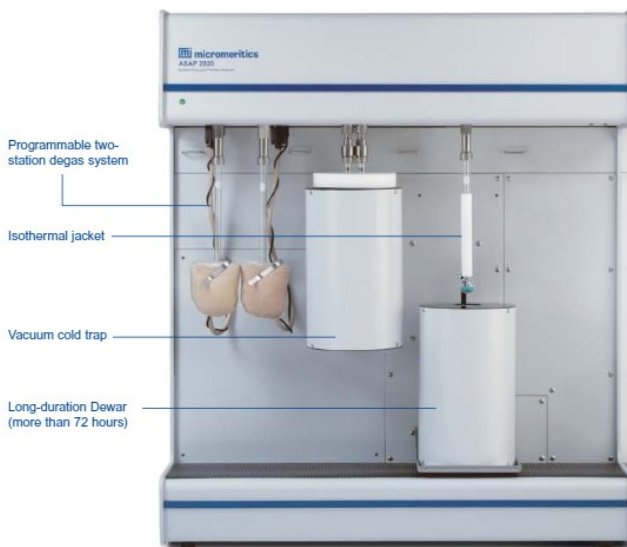


Figure 1-9. Micromeritics ASAP 2020 analyser [28].

1.2.5 Inductively Coupled Plasma Optical Emission Spectrometry (ICP-OES)

The ICP-OES is used to determine the elemental concentration in liquid samples. Elements in solid samples can be analysed only if they are first digested in aqua regia and the filtrate used for the analysis.

The solution to be analysed must be aerosolised first, this aerosol is moved to an argon plasma chamber. In that chamber, plasma is generated by the ignition of argon gas through collision between argon atoms and accelerated electrons from a quartz torch; this collision induces ionisation and the production of a stable plasma. With the high temperature plasma, the aerosols undergo processes that include atomisation and ionisation. When the excited accelerated electrons return to their ground state, the energy they liberate is emitted as photons in which different element has its own characteristic emission spectra which is measured and analysed. The schematics of the ICP-OES is shown in Figure 1-10.

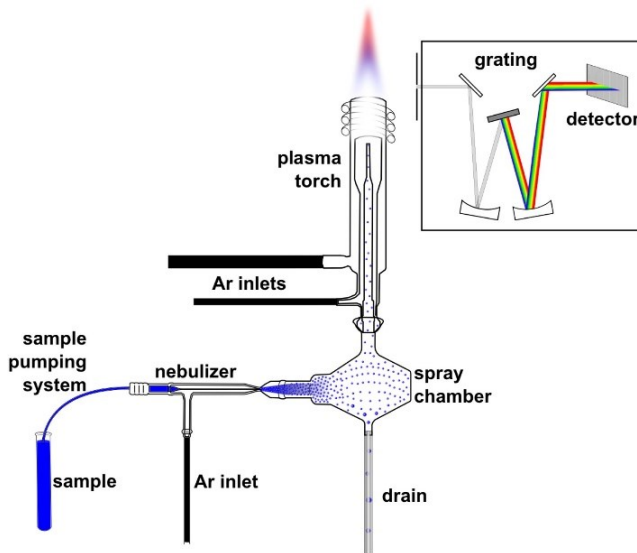


Figure 1-10. ICP - OES instrument schematics [29].

1.2.6 Transmission Emission Microscopy (TEM)

While SEM generates 3D images detected via reflected electrons, TEM generates 2D images from electrons transmitted through the sample. It is a vital tool in material characterisation. The main components are an electron gun, a specimen stage, electron lenses, aperture, and a vacuum system. The electron gun produces a focused electron beam with high energy

which strikes and is transmitted through the specimen to generate an image [22]. Vital information like structural defects, contamination, composition, and crystalline structure is obtained using this method. Figure 1-11 shows the high resolution TEM of the well-ordered hematite structures within coal fly ash particles, the EDX spectrum shows the distribution of elements. Figure 1-12 shows the schematics of a TEM equipment.

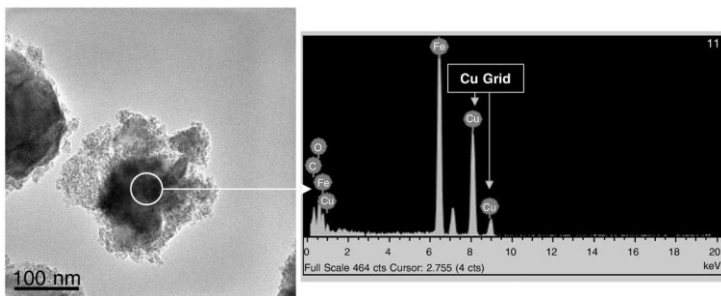


Figure 1-11 TEM image and EDX spectrum of hematite in fly ash [30].

Unlike SEM, sample preparation for TEM analysis is a laborious process. For instance, powdered samples have to be thoroughly mixed in an organic solvent, placed on a copper grid, and then evaporated in a desiccator prior to

analysis [22]. This can introduce artifacts to the sample and affect the image generated by the equipment.

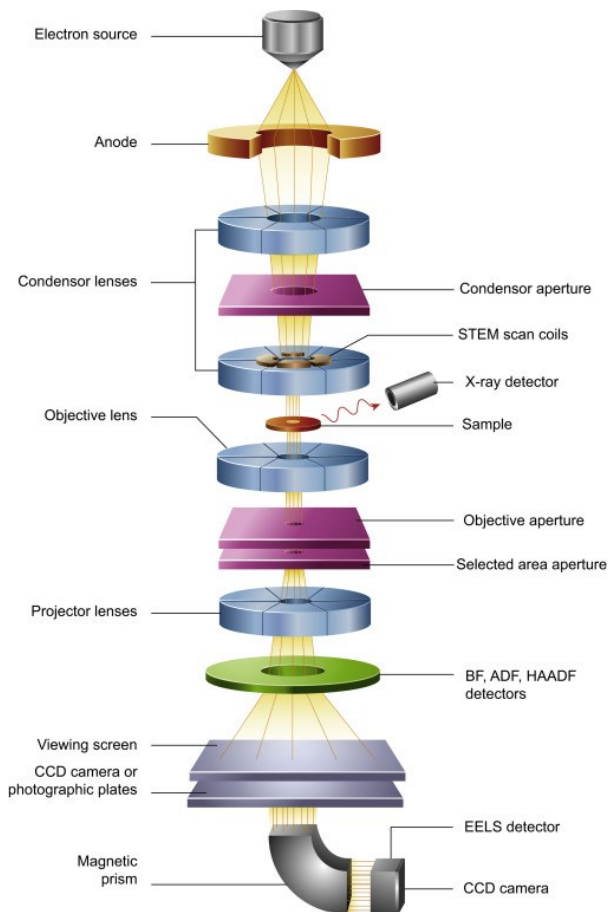


Figure 1-12. TEM equipment schematics [31].

1.2.7 Applications

1.2.7.1 Catalysis

One of the major industrial field of application of zeolites is in fluid catalytic cracking (FCC) of hydrocarbons in petroleum refining; FCC application accounts for more than 95% of the global usage of zeolites in catalysis [32]. The synthetic faujasite zeolites, zeolites X and Y, were found to be much more effective than the ones previously used in FCC units which spurred the usage of FAU-type zeolites as catalysts in petroleum and petrochemical industries [33]. The most important factor regarding zeolite catalytic activity is shape selectivity which is as a result of the diffusivity difference in reactants and products, the adsorption variation of reactants within the zeolite cavities, and the selectivity of the transition state [34]. Zeolites are also used in catalytic converters in diesel engine exhausts for NOx emission reduction and in methane dehydroaromatization.

1.2.7.2 Ion exchange

Zeolites are used as ion exchangers due to the negative charge of their framework, which is balanced by cations, which can be reversibly ion exchanged [7]. Important ion exchange processes where zeolites are used include water-softening, soaps, and detergents.

1.2.7.3 Adsorption

Zeolite crystals are porous with arrays of channels and cavities in the range of 3 – 20Å; these micropores can be filled with water or other molecules depending on size selectivity [35]. Application of zeolites in adsorption include removal of heavy metals in contaminated water, soil remediation, and gas separation.

1.3 Zeolite Synthesis from Alternative Raw Materials

The use of pure chemicals as starting materials in the preparation of synthetic zeolites leads to the development of zeolitic materials with less impurities and less likelihood for the nucleation of undesirable species.

The use of alternative raw materials that are sourced from the environment, be it environmental wastes or naturally occurring materials, is an attractive option. Using waste materials from the environment for zeolite synthesis offers a double fold benefit – waste reduction/elimination and cost-effective starting materials. Zeolites prepared from waste materials using a combination of alkali fusion and hydrothermal synthesis include coal fly ash zeolites NaX, NaY, NaA; ZSM-5 zeolite, NaA, NaX, NaY, sodalite from rice husk ash [14,36–43]. NaA, NaX, sodalite from aluminum wastes from primary and secondary industries; and NaA, NaX, sodalite from blast furnace sludge [42–47]. The synthesis of zeolites such as NaA, NaX, and sodalite have been reported using natural clays such as bentonite, kaolinite, vermiculite, illite, and montmorillonite [48–53].

In this research, coal fly ash (Chapter 2) and clays (Chapters 4 and 5), which are cheap and abundant materials, were used. Zeolites from peat ash, a material

rarely used for zeolite synthesis compared to fly ash, is discussed in Chapter 4.

1.4 Fundamentals of Adsorption

Adsorption is an important process whereby ions, atoms, or molecules adhere to the surface of a material it is in contact with. An adsorbate is the species that adheres to the adsorbing surface called the adsorbent. The adsorption process is divided into two major types: physisorption and chemisorption. As the name implies, physisorption does not involve a chemical reaction, instead weak Van der Waals forces of attraction exist when the adsorbate encounters the adsorbent surface [27,54]. On the other hand, chemisorption involves the interaction of intermolecular forces leading to the adsorbates and the adsorbents forming chemical bonds. The counterpart of adsorption is desorption where the adsorption process is reversed, the amount of the adsorbate on the adsorbent progressively decreases.

In addition to the IUPAC classification of porous materials as microporous, mesoporous, and macroporous ($d_p > 50$ nm), zeolites are often referred to in literature as *nanoporous*, a term that is used to describe materials with uniform pores such as zeolites, metal-organic frameworks and ordered mesoporous silica [27].

In mesopores, physisorption takes place mainly in three ways:- (i) *monolayer* adsorption where the adsorbate molecules are in contact with the adsorbent surface; (ii) *multilayer* adsorption where more than one layer of adsorbed molecules is formed which are not necessarily in direct contact with the adsorbent surface; and (iii) *pore* (or *capillary*) condensation. Capillary condensation occurs when the pore pressure is less than the saturation pressure of the bulk liquid, the adsorbate gas is condensed to a liquid state within the pore space.

The IUPAC classification of adsorption isotherms driven by physisorption is shown in Figure 1-13.

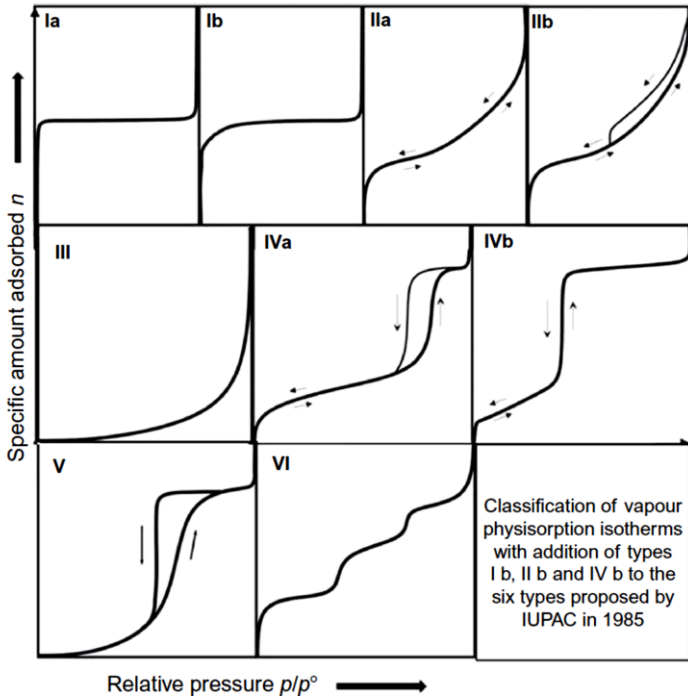


Figure 1-13 Adsorption isotherms [55].

Type I isotherm, subdivided into type 1a (narrow pores) and 1b (wide pores), is characteristic of microporous adsorbents with small external surface areas [27]. Type II is characteristic of macroporous or nonporous adsorbents, the middle of the quasi-linear portion of the curve represents the complete coverage of a monolayer

wherein the surface area can be estimated, the completion of a monolayer leads to the beginning of the development of a multilayer coverage. Type II is subdivided into type IIa and type IIb. The type IIa isotherm does not have a hysteresis loop, it is an indicator that the adsorption and desorption isotherms are totally reversible. Compared with the other isotherm types with hysteresis, the type IIb hysteresis is quite narrow due to inter-particle pore condensation. Presently, powdered materials with type II isotherms and H3 hysteresis loops are referred to as having a type IIb isotherm [55]. Type III represents the weak adsorbent – adsorbate interactions for macroporous or nonporous adsorbents. Type IV represents the behaviour of adsorbents with mesopores, in which pore condensation is preceded by monolayer – multilayer adsorption on the walls of the mesopores. When the pore width exceeds 4 nm, hysteresis accompanies the capillary condensation and is represented by type IVa adsorption isotherm. Pore widths below the critical value of 4 nm is represented by

Type IVb isotherm. Type V isotherms are rare, the hysteresis loop is for weak adsorbate – adsorbent interactions. The stepwise Type VI isotherm is also rare and is attributed to uniform nonporous materials like graphitised carbon.

Hysteresis loops which are attributed to capillary (pore) condensation are currently classified into types H1, H2(a), H2(b), H3, H4, and H5 as shown in Figure 1-14 [27,56].

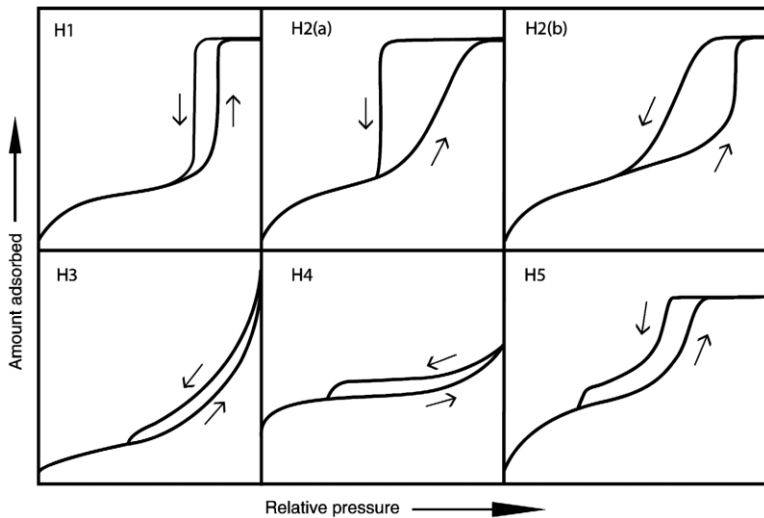


Figure 1-14 Types of hysteresis loops [27].

The type H1 physisorption hysteresis loop is characterised by almost vertical and steep adsorption and desorption curves that are parallel, the narrowness of the loop is an indication of delay in capillary (pore) condensation during adsorption [27,57]. The mesoporous materials exhibiting type H1 hysteresis do not have interconnecting channels with uniform clusters of spheres, they have a very narrow pore size distribution.

The materials that exhibit type 2 hysteresis have ink bottle-shaped network of pores which consists of a narrow neck region and a wider body which has to be filled up first until the pressure is reduced resulting in the evaporation of the neck region causing a delay in pore condensation [56]. Type 2 hysteresis is subdivided into type H2(a) and H2(b). Type H2(a) is characterised by either the blockage of pores or evaporation that is induced by cavitation, here the pore cavity is wider than the neck cavity in terms of size distribution [27,56]. In type 2(b), the hysteresis conditions are opposite that of

type H2(a), the neck cavity size distribution is wider than the pore cavity.

The type 3 hysteresis loop is usually exhibited by materials like clays which have non-rigid clusters of plate-like particles, here there are mainly macropores which are not saturated with pore condensates [27,57]. The plate-like particles give rise to slit-shaped pores.

The type H4 hysteresis loops are common in zeolites where the adsorption curve is a combination of the type I and type 2 adsorption isotherms while the desorption curve has its lower limit located at the pressure where cavitation is induced ($p/p^0 = 0.42$ for N_2 adsorption at $-196\text{ }^\circ\text{C}$) [27]. Compared to other hysteresis loops shown in Figure 1-14, type H4 hysteresis has the highest uptake of adsorbate at low p/p^0 resulting from the filling up of the pores.

Type H5 hysteresis is an uncommon type which is characterised by pore structures having partially obstructed and open mesopores [27].

1.4.1 Empirical adsorption isotherm equations

The experimental data obtained for physisorption can be interpolated or extrapolated using empirical equations and computer aided methods for curve fitting.

An important parameter, the equilibrium amount adsorbed, q_e (mg/g), is given by Equation 4.

$$q_e = \frac{(C_0 - C_e)}{m} V \quad \text{Equation 4}$$

where V (L) is the volume of the solution, m (g) is the mass of the adsorbent, while C_0 (mg/L) and C_e (mg/L) are the initial and the equilibrium concentrations, respectively.

1.4.1.1 Henry's isotherm

Henry's isotherm is a one-parameter model and the simplest isotherm that is applicable at low adsorbate concentrations [58]. This isotherm is based on Henry's law which states that at constant temperature, the amount of gas dissolved in a liquid is directly proportional to the partial pressure of the gas in equilibrium with the liquid. This is expressed by Equation 5.

$$q_e = K_H \cdot C_e \quad \text{Equation 5}$$

where K_H (L/g) is Henry's law constant.

1.4.1.2 The Langmuir isotherm

The Langmuir isotherm is a two-parameter isotherm commonly used to describe homogenous monolayer adsorption on finite adsorption sites without the interaction of the layers. The nonlinear and linear forms of the Langmuir adsorption model can be written as shown in Equations 6 and 7 [58,59].

$$q_e = \frac{q_m \cdot K_L \cdot C_e}{1 + K_L \cdot C_e} \quad \text{Equation 6}$$

$$\frac{C_e}{q_e} = \frac{1}{K_L \cdot q_m} + \frac{C_e}{q_m} \quad \text{Equation 7}$$

where K_L (L/mg) is the Langmuir isotherm constant, while q_e (mg/g) and q_m (mg/g) are the equilibrium and the maximum sorption capacity of the adsorbent, respectively.

The model assumes that the rate of adsorption and desorption are equal, that adsorption is limited to

monolayer, and that molecules are adsorbed on fixed localised sites with no interaction between the adsorbed molecules [58,60,61]. This isotherm is applicable to type I adsorption classification and reduces to Henry's law when the partial pressure is very low.

In some instances, the Langmuir adsorption isotherm, which is based on a single component system, cannot adequately describe the adsorption of multi component systems. A modified Langmuir isotherm, also called the Langmuir competitive adsorption model, that factors in the complexity of a multi component adsorption process is given in Equation 8 [62,63].

$$q_{e,i} = \frac{q_{m,i} K_{L,i} (C_{e,i} / \eta_i)}{1 + \sum_{j=1}^N K_{L,j} (C_{e,j} / \eta_j)} \quad \text{Equation 8}$$

where $q_{e,i}$ is the amount of any of the multicomponent 'i' per unit mass of the adsorbent, $q_{m,i}$ and $K_{L,i}$ are constants obtained by fitting the equilibrium data to the single component model for component 'i', η_i is a correction factor, and $C_{e,i}$ is the equilibrium concentration of 'i' in competitive adsorption with N components [63].

1.4.1.3 The Freundlich isotherm

The Freundlich isotherm, another two-parameter empirical model, is used to describe non-ideal reversible adsorption process and the model assumption is not restricted to the formation of a monolayer [60]. It is applicable to multilayer adsorption over heterogeneous surfaces [58,60,64] and is described by Equations 9 and 10:

$$q_e = K_F \cdot C_e^{1/n} \quad \text{Equation 9}$$

$$\log q_e = \log K_F + \frac{1}{n} \log C_e \quad \text{Equation 10}$$

where K_F is the Freundlich isotherm constant which indicates adsorption and n (>1) is a dimensionless parameter that symbolises adsorption density.

Due to the complexity in fitting equilibrium data to adsorption models, complex models with more than two model parameters have been postulated to give a better description of the adsorption process.

1.4.1.4 The Tóth isotherm

The Tóth isotherm, a three-parameter isotherm, is a modification of the Langmuir isotherm and is used for the description of heterogenous multilayer adsorption for both low and high concentrations [60]. The mathematical expression of Tóth isotherm [65,66] is given in the following equation:

$$q_e = \frac{K_T \cdot C_e}{(\alpha_T + C_e)^{1/t}} \quad \text{Equation 11}$$

where K_T is the Toth constant (mg/g) while α_T and t are also constants.

At $t = 1$, the equation reduces to the Langmuir isotherm model indicating heterogeneity of the adsorption process.

1.4.1.5 The Redlich-Peterson isotherm

Another three-parameter model is the Redlich-Peterson isotherm. The combination of the Freundlich and Langmuir isotherms resulted in this three-parameter empirical equation. It is more versatile than the two-parameter models, at very low concentration it

approaches Henry's law. The applicability of this model includes high and low concentrations and either homogeneity or heterogeneity [60,67,68]. The nonlinear expression is shown in Equation 12:

$$q_e = \frac{K_{RP} \cdot C_e}{1 + a_{RP} \cdot C_e^{b_{RP}}} \quad \text{Equation 12}$$

where b_{RP} is an exponent, whose values should lie between 0 and 1, while K_{RP} and a_{RP} are constants [58].

The Redlich – Peterson equation reduces to the Freundlich equation at very high concentration. When the exponent, b_{RP} , equals 1, the equation reduces to the Langmuir equation.

1.4.1.6 The Fritz–Schlunder isotherm

The Fritz–Schlunder [63,67] four parameter model, another model derived by the combination of the Freundlich and Langmuir isotherms, is mathematically expressed in Equation 13 as:

$$q_e = \frac{\alpha_1 \cdot C_e^{\beta_1}}{1 + \alpha_2 \cdot C_e^{\beta_2}} \quad \text{Equation 13}$$

where α_1 and α_2 are the model parameters, and the exponents, β_1 and β_2 , are ≤ 1 [69].

1.4.2 Adsorption kinetics

An indicator of the adsorption type and mechanism for the sorption process is determined by the adsorption kinetics. The consideration of adsorption kinetics is important in the design of adsorption systems since kinetics can predict the rate of adsorption. Some of the adsorption kinetics models include pseudo first and second order, the intraparticle diffusion model, and the Elovich model.

Similarly to adsorption isotherms, a mathematical expression of the adsorbate uptake by the adsorbent is shown in Equation 14.

$$q_t = \frac{(C_0 - C_t)}{m} V \quad \text{Equation 14}$$

where q_t (mg/g) is the amount of adsorbate adsorbed at time t , V (L) is the volume of the solution, m (g) is the mass

of the adsorbent, while C_0 (mg/L) is the initial concentration and C_t (mg/L) is the equilibrium concentration at time t .

1.4.2.1 Pseudo first - order (PFO) model

The PFO, also known as the Lagergren equation, is used to describe the adsorption capacity in solid liquid systems by the mechanism described in Equation 15 [70–72]. This model assumes that adsorption occurs only at localised sites with no interaction of the adsorbed components [73].

$$\log(q_e - q_t) = \log(q_e) - \left(\frac{k_{PFO}}{2.303}\right)t \quad \text{Equation 15}$$

where q_e (mg/g) and q_t (mg/g) are the adsorption capacities at equilibrium and time t , respectively, k_{PFO} (per min) is the PFO rate constant.

1.4.2.2 Pseudo second - order (PSO) model

The PSO model assumption is based on the proportional relationship of the rate of adsorption with the sites available for adsorption and is expressed by Equation 16 [71,72].

$$t/q_t = \left(\frac{1}{k_{PSO} \cdot q_e^2} \right) + t \left(\frac{1}{q_e} \right) \quad \text{Equation 16}$$

where k_{PSO} (g.mg)/(min) is the PFO rate constant and all the other terms are as previously defined.

1.4.2.3 Elovich model

This model assumes that adsorption occurs at localised sites with the interaction of the adsorbed components and an inverse proportion relation between the rate of adsorption and the amount of solute adsorbed [71,73]. This is expressed by Equation 17 [2].

$$q_t = \left(\frac{1}{\beta} \right) \ln(\alpha \cdot \beta) + \left(\frac{1}{\beta} \right) \ln t \quad \text{Equation 17}$$

where α (mg)/(g.min) is the initial rate of adsorption and β (g/mg) is related to the activation energy and the surface coverage [2].

1.4.2.4 Intraparticle diffusion model

This model is used to describe the diffusion within the pores of the adsorbents [70,74]. The uptake of the adsorbate is directly proportional to the half power of time as mathematically expressed in Equation 18 [72].

$$q_t = k_i \cdot t^{0.5} + C$$

Equation 18

where k_i (mg)/(g.min^{-0.5}) is the model rate constant.

1.4.3 Model validation via statistical analysis

The goodness of fit for adsorption isotherms and kinetics is usually determined by the coefficient of determination, R^2 , obtained by either linear or nonlinear regression of the equilibrium data.

Statistically, R^2 is expressed by Equation 19 where SS_{res} and SS_{tot} are the residual and the total sum of squares, respectively. The closer the value is to unity, the better the fit to the adsorption isotherm or kinetics.

$$R^2 = 1 - \left(\frac{SS_{res}}{SS_{tot}} \right)$$

Equation 19

1.5 Removal of toxic heavy metals from water

Water pollution is any chemical, physical, or biological change in the quality of water that has a harmful effect on any living thing that drinks or uses or lives in it. An

upsurge in the release of metals in the environment as a result of rapid industrialisation has resulted in an increment in water pollution problems; heavy metals, referring to transition metals with atomic mass and specific gravity more than 20 and 5 g/cm³ respectively, are the most toxic [75]. Trace amounts of heavy metals like copper, iron, and zinc are essential for metabolism in all living things; excess amounts of these essential metals can overwhelm the homeostatic mechanism of an organism [76,77].

The toxicity of Cd, Co, Cu, Pb, and Zn varies with their common factor being their capability of being lethal even in small concentrations due to bioaccumulation of said metals in humans. Toxic effects range from disruption of the nervous system to cancer.

Cadmium, a carcinogenic by inhalation with accumulation in kidneys, has a guideline value of 3 µg/L for humans [78,79]. In addition, the health problems related to an acute cadmium poisoning include elevated blood pressure, testicular tissue damage, and the

destruction of red blood cells; due to the chemical similarity of cadmium and zinc, the catalytic activity of enzymes are affected by the stereostructure alteration carried out by cadmium [80,81]. Tests done on rodents to determine the toxicity of cobalt showed that a short-term exposure of 1.9 µg/L lead to inflammation of the respiratory tract while 19 µg/L lead to necrosis; cobalt has been proven to affect the developmental and reproductive abilities in animals with similar possibilities for humans [82]. Copper, though an essential micronutrient for humans, was assigned a maximum contaminant level goal of 1.3 mg/L by the EPA due to the adverse effects on humans in causing gastrointestinal disturbances and liver toxicity [83]. Lead has been proven to cause mental retardation to children who are exposed to lead released in the environment [81]. Zinc, another essential nutrient in all living organisms, induces vomiting with the ingestion of more than 500 mg of its sulphate; zinc poisoning has been reported for the ingestion of alcoholic beverages packaged in galvanised containers,

the effects included fever, nausea, and even bleeding within 24 hours of acute poisoning.

The release of these toxic metals from industrial and non-industrial processes find their way to water available for consumption – humans, animals, flora and fauna. The availability of safe drinking water, devoid of harmful levels of heavy metals, is of vital importance. Due to the toxicity of heavy metals, regulatory bodies like the Environment Protection Agency (EPA) and the World Health Organisation (WHO) have established stringent limits for drinking water.

According to the Brundtland report, “Sustainable development is development that meets the needs of the present without compromising the ability of future generations to meet their own needs” [84]. Right now, the need of the present is quite compromised even before we could contemplate the needs of the future which is equally as important.

The techniques for the removal of toxic metals in water include ion exchange, adsorption (chemisorption and physisorption), coagulation, solvent extraction, and membranes. Among those methods, adsorption is the most effective it is versatile, cost effective, and easy to operate [39].

1.5.1 Heavy metals removal from water using zeolites

There is a wealth of literature on the uptake of toxic heavy metals like Cd, Co, Cu, Fe, Pb, and Zn from contaminated water by adsorption technique using natural and synthetic zeolites as adsorbents [39,49,92–97,50,85–91]. These zeolites include clinoptilolite, faujasites, GIS, and NaA.

Wingenfelder et al. reported the use of natural clinoptilolite for the removal of Fe, Pb, Cd, and Zn from acid mine water, they found that with that competing adsorption system, Pb was preferentially adsorbed [97]. Blanchard et al. used Na-exchanged natural clinoptilolite for the competitive adsorption of Cd, Co, Cu, Hg, Pb, NH₄, Ni, and Zn, they reported that the decreasing adsorption

trend was $Pb > NH_4 > Cu > Cd > Zn > Co > Ni > Hg$ [96]. Ting et al. prepared Linde type F zeolite from coal fly ash and used it for a quaternary adsorption system consisting of Cd, Cu, Ni, and Pb, they reported an overall trend of $Pb > Cd > Cu > Ni$ [98]. GIS was prepared from coal fly ash by Hamadi et al. for the removal of Cr, Pb, and Zn from aqueous solutions, the selectivity trend was $Zn > Pb > Cr$ with Langmuir isotherm adsorption capacities of 34.2, 25.6, and 10.4 mg/g, respectively [88]. Visa et al. used GIS synthesised from coal fly ash to remove Cd, Cu and methylene blue from a synthetic wastewater, they found that Cu was preferentially adsorbed in both one- and two-component adsorption systems [87]. Maksod et al. reported the use of LTA zeolite prepared from kaolin to remove Cu, Ni, and Pb from aqueous solutions, Cu and Pb were preferentially removed from the solutions [99]. Except for a few outliers, which depend on the pollutant or adsorbent matrix, uptake of heavy metals that include Pb usually lead to the preferential adsorption of Pb in multicomponent adsorption systems [96,100]. The high

adsorption affinity of zeolites for Pb in a multicomponent system could be as a result of the hydrated radii of the ionic species and the strength of the ionic potential for the inner-sphere complexation of the adsorbent and the metal cations [101].

1.6 Research background and motivation

Water pollution by toxic metals has impacts that transcend geographical locations. With the varied sources of toxic metals resulting from anthropogenic activities, zeolites can be synthesised from alternative materials sourced from the environment for the uptake of heavy metals that threaten water quality. This is a case of environmental problems being part of its solution.

The available literature lacks cohesion in the systematic method for the synthesis of faujasite and cancrinite zeolites and the purification of water contaminated with a multicomponent mix of heavy metals. This lack created a knowledge gap that needs to be filled to meet up to the challenge of the ever-changing fields of synthetic

adsorbent and multicomponent adsorption system development.

1.7 Aims and Objectives

This research was undertaken to address the issue of a systematic method for the synthesis of faujasite and cancrinite zeolites and their applicability in wastewater treatment.

The overall aim of this research was the optimal synthesis and characterisation of zeolites from coal fly ash, peat ash, and geophagic clay. The prepared zeolites were used for the removal of Cd (II), Co (II), Cu (II), Pb (II), and Zn (II) from aqueous solutions over a range of concentrations and adsorbent loadings. These five metals were selected because of their prevalence in literature to serve as a basis for comparison in multicomponent adsorption systems.

The aim was achieved through the following objectives:

1. Pre-treatment of the waste materials (coal fly ash and peat ash) via calcination and acid leaching.

2. Synthesis through alkali fusion and dissolution in basic medium followed by hydrothermal treatment for coal fly ash, peat ash, and clay.
3. Characterisation of materials pre and post synthesis using XRF, XRD, surface analysis, and SEM/EDX.
4. Batch adsorption tests using all the prepared zeolites as adsorbents for the simultaneous removal of heavy metals from aqueous solutions and the analysis of metal concentrations using ICP-OES.

Additional problems investigated in achieving the objectives were:

- i. The similarity of faujasite zeolites synthesised from different starting materials using the pre alkaline fusion and hydrothermal treatment synthesis route.
- ii. The similarity or dissimilarity of the optimal conditions for faujasite zeolite synthesis from coal fly ash, peat ash, and clay.

- iii. The performance of faujasite zeolites over other zeolite types synthesised in this work for the uptake of the five metals from aqueous solutions.

This thesis strives to significantly contribute to the understanding of a systematic and optimal faujasite and cancrinite zeolite synthesis from non-commercial starting materials and the removal of a multicomponent mix of heavy metals from contaminated water. This research incorporated practicalities in instrumentation, computer analysis, material development, characterisation, and optimisation. The significance of this research work is hoped to provide points of reference for both academia and industry involved in nanomaterial development and water purification.

2 ZEOLITES FROM COAL FLY ASH (CFA)

2.1 Literature Review

Coal fly ash is the particulate matter obtained from the combustion of coal, the coal could be anthracite, bituminous, subbituminous, or lignite depending on the organic and inorganic matter content [14]. From the pulverised coal used for combustion in thermal power stations, about 80% of all its ash are fly ash conveyed by flue gases into the exhaust stacks [14,102]. The ash is usually collected with electrostatic precipitators or cyclones before the flue gases exit the combustion system.

The ASTM C618 classification for coal fly ash into class C and class F [103] is based on the total amounts of SiO_2 , Al_2O_3 , and Fe_2O_3 present in the fly ash (Table 2-1). Subbituminous and lignite coal are geologically younger and have lower carbon content and heating value, the fly ash generated from such is called Class C. Fly ash from anthracite or bituminous coal which are geologically older and with higher heating values are called Class F. A

summary of the ASTM C618 standard for coal fly ash is shown in Table 2-1.

Table 2-1 ASTM C618 requirements for coal fly ash [103].

Requirements	Class C (max %)	Class F (max %)
$\text{SiO}_2 + \text{Al}_2\text{O}_3 + \text{Fe}_2\text{O}_3$	50	70
SO_3	5	5
Moisture content	3	3
Loss on ignition (LOI)	6	6

The chemical composition of CFA varies with geographical location and the coal source, for instance, Table 2-2 shows the composition of CFA from 3 different geographical regions as reported by Berkgaut and Singer [104]. Even though the coal fly ash from the three regions were from bituminous coal, their elemental composition varied. The reported phases in coal fly ash, identified by

XRD, include crystalline structures like mullite, calcite, hematite, and quartz [14,104].

Table 2-2 Chemical composition of CFA (mass %) [104].

Oxide / Location	Colombia	South Africa	West Virginia, USA
SiO ₂	61.6	44.7	57.3
Al ₂ O ₃	21.3	32.3	32.9
Fe ₂ O ₃	6.5	4.0	4.9
CaO	3.2	9.4	1.1
TiO ₂	1.0	1.5	-
K ₂ O	1.6	0.9	-
SO ₃	-	0.8	0.1
P ₂ O ₅	0.5	2.3	-
LOI	6.2	5.1	4.0

Due to the compositional similarity of CFA to volcanic ash, zeolites can be prepared from fly ash; Holler and

Wirsching published the first work on zeolite synthesis from fly ash in 1985 [105,106]. The reported literature on zeolites prepared from CFA include LTA, NaX, NaY, GIS, and chabazite [17,87,107,108].

In synthesising zeolites from CFA, hydrothermal and pre alkali fusion hydrothermal synthesis routes require the use of alkali solution for the dissolution of the crystalline phases in the starting material followed by the subsequent nucleation and crystallisation of zeolite phases after hydrothermal treatment. Since coal fly ash is one of the most extensively researched material in zeolite synthesis, there is a plethora of literature on its conversion to zeolites through various synthesis routes. The conventional method is mainly hydrothermal synthesis route and its variants which involves the reaction of CFA in alkaline media at a specified temperature while unconventional methods include microwave assisted technique and dry or molten salt conversion [17,38,109]. A summary of the methods is shown in Table 2-3.

Some of the reported synthesis via the conventional hydrothermal route involved heating CFA in varied NaOH or KOH or Na₂CO₃ to fly ash ratios (Table **2-3**) at autogenous pressure and a temperature range of 80 – 150 °C and activation duration of 3 to 96 hours [8,17,105]. In varying important factors like the alkali fusion temperature, liquid to solid mass ratio, ageing temperature and duration, and hydrothermal treatment temperature and duration, zeolite products like NaA, GIS, and sodalite were reported at yields of about 20 – 65 wt % of CFA [8,110,111].

Shigemoto et al. improved upon the traditional hydrothermal treatment method by adding an alkali fusion step before hydrothermal treatment [112]. With that method, CFA is mixed with different mass ratio of CFA to NaOH and the mixture is fused at temperature ranging from 400 - 750 °C, the fusion converts most of the crystalline phases into soluble aluminosilicates [104,111–115].

Table 2-3 Fly ash to zeolite methods.

Synthesis method	Liquid-solid ratio	Reagent	Temp. (°C)	Activation time (h)	Zeolite	Ref
Conventional hydrothermal	8	NaOH, KOH, Na ₂ CO ₃	90 - 150	24 - 96	Chabazite, GIS, phillipsite, sodalite, zeolites A, X, and Y	[108,113,116,117]
Microwave assisted hydrothermal	8	NaOH	100	0.25 - 2	GIS	[118-120]
Combined fusion and hydrothermal	10	NaOH or NaAlO ₂	500 - 650	1 - 2	Zeolites A and X	[15,104,112,113,121-123]
		H ₂ O	90 - 100	6		
Dry or molten salts	-	KOH, KNO ₃ , NaOH, NaNO ₃ , NH ₄ F, NH ₄ NO ₃	350	3 - 6	Sodalite	[124-126]
				24	Cancrinite	

The addition of water, aging under stirred or static conditions, and heating (hydrothermal treatment) results in the nucleation and crystallisation of zeolites.

The microwave assisted synthesis method is employed to reduce the time it takes for the completion of CFA to

zeolite synthesis. This involves an initial microwave heating of approximately 30 minutes prior to the conventional hydrothermal method although this is done at an early stage of the hydrothermal method to favour the initiation of the zeolitisation process [8,17].

The dry or molten salt method, developed by Park et al., involves the use of powder mixtures composed of CFA, NaOH, and NaNO₃ in place of an alkaline solution as the reaction media and treated at 350 °C to activate the zeolitisation process; the zeolitic products obtained were of higher purity than the products from the hydrothermal route [8,17,125].

The results from this chapter have been included in Appendix 2 (Paper 2).

2.2 Materials

Raw CFA was obtained from the Lethabo Power Station in South Africa; the coal from which the ash was generated has an average calorific value of 16 MJ/kg.

The list of chemicals used, purchased from Sigma Aldrich UK, is given below:

- i. Powdered sodium hydroxide NaOH, 99.99% trace metals basis, CAS 1310-73-2.
- ii. Copper (II) nitrate trihydrate $\text{Cu}(\text{NO}_3)_2 \cdot 3\text{H}_2\text{O}$, 99.999% trace metals basis), CAS 10031-43-3
- iii. Zinc nitrate hexahydrate $\text{Zn}(\text{NO}_3)_2 \cdot 6\text{H}_2\text{O}$, 99.999% trace metals basis), CAS 10196-18-6.
- iv. Cobalt (II) nitrate hexahydrate $\text{Co}(\text{NO}_3)_2 \cdot 6\text{H}_2\text{O}$, 99.999% trace metals basis, CAS 10026-22-9.
- v. Lead (II) nitrate $\text{Pb}(\text{NO}_3)_2$, 99.999% trace metals basis, CAS 10099-74-8.
- vi. Cadmium nitrate tetrahydrate $\text{Cd}(\text{NO}_3)_2 \cdot 4\text{H}_2\text{O}$, 99.999% trace metals basis, CAS 10022-68-1.

Powder X-ray diffraction (XRD) was carried out with a PANalytical X'Pert Powder diffractometer with a sample spinner and 1D detector in Bragg–Brentano geometry employing copper $\text{K}\alpha$ radiation ($\text{K}\alpha_1 = 1.5406 \text{ \AA}$ and $\text{K}\alpha_2 = 1.5444 \text{ \AA}$). Data collections from 4° to 120° coupled 2θ at 0.0131° with a time step of 88 sec were undertaken.

All other samples were presented as powders using top-loading sample holders. Data was processed using HighScore Plus version 4.9 with phase identification carried out using the Crystallography Open Database implemented within HighScore.

A Carl Zeiss Supra 40VP Scanning Electron Microscope was used to obtain SEM micrographs at magnifications between 5 Kx to 20 Kx while semi-quantitative chemical analysis was done with EDX. The nitrogen adsorption isotherms at -196 °C were obtained using a Micrometrics ASAP 2020 surface area analyser. Samples were degassed for 3 h at 300 °C prior to analysis. The Barrett-Joyner-Halenda (BJH) adsorption-desorption method was used to determine the pore size distributions, the surface areas were determined using the BET model while the micropore volumes and external surface areas were calculated using the t-plot method. The chemical composition of the samples prepared was obtained with a Rigaku NEX-CG X-ray Fluorescence spectrometer. The concentrations of metals in solution were determined

using the iCAP 63000 Duo series Thermo Scientific Inductively Coupled Plasma-Optical Emission Spectrometer. A LS500 EA3 Gerhardt Laboshake was used to shake samples for adsorption experiments.

2.3 Synthesis

CFA sample was weighed and mixed with powdered NaOH, at a CFA to NaOH mass ratio of 1:1.2 and fused in a furnace for 3 h at 600 °C [113,127]. After NaOH fusion, a mortar was used to grind the fused sample and precise amounts of the ground fused sample was mixed with deionised water in polypropylene reactors. The fused sample to deionised water ratios used for the experiment were 1:4, 1:10, 1:15, and 1:20. The solutions in the polypropylene reactors were aged for 24, 48, 68, and 72 h at ambient temperature while stirring with magnetic stirrers. Aged samples were transferred to a preheated oven for hydrothermal treatment at 80 °C for 24h. In some experiments, hydrothermal treatment was extended up till 72 h. After hydrothermal treatment the

samples were filtered, washed to remove excess NaOH, and dried overnight at 90 °C. The dried samples were calcined in a furnace at 550°C in air at 550 °C for 4 h at a furnace temperature ramp rate of 5 °C/min.

A reference synthetic faujasite zeolite, NaX, was prepared as reported by Valtchev et al. with a gel with a molar composition of 8NaOH: 0.2Al₂O₃:1.0SiO₂:200H₂O [127].

2.4 Adsorption Studies

To test the efficacy of the prepared zeolites, a stock solution of Cd, Co, Cu, Pb, and Zn salts (c.f. Section 2.2) at 1000 mg/L in each metal was prepared by adding appropriate amounts of the metal salts to deionised water in a 1 L volumetric flask. To obtain standard solutions, appropriate dilutions of the stock solution was made to obtain a concentration range of 100 to 500 mg/L in volumetric flasks.

Batch adsorption experiments for a competitive adsorption system involving quinary metal ions were carried out at 25 °C in triplicates. Appropriate amounts of the adsorbents (the optimal FAU zeolite, CFZ10-68, and the reference zeolite, ZRef-FAU) were added to aliquots of the standard solutions to test for the effects of the adsorption duration, adsorbent loading, and concentration of the adsorbate. In testing for the optimal adsorption duration, adsorbent loads of 5 g/L were mixed with the appropriate volume of standard solution (initial concentration of 200 mg/L) in 120 mL polypropylene (PP) sample bottles, the bottles were shaken in a circular motion using a Gerhardt Laboshake for intervals between 10 to 180 min. In assessing the effects of adsorbent loading at the optimal duration determined from the previous experiments, standard solutions having initial concentrations of 200 mg/L were mixed with the adsorbents (CFZ10-68 and ZRef-FAU) and the adsorbent loadings varied from 5 to 15 g/L for 90 min. The effects of the initial concentration of the five metals in a

competitive adsorption system was carried out with an adsorbent loading of 5 g/L for 90 min at a concentration range of 100 to 500 mg/L. At the completion of each experiment, each sample was centrifuged for 4 min at 3800 rpm and the supernatant analysed for heavy metal concentration using ICP-OES.

The amount of heavy metal removed during the adsorption process, expressed in percentage, is given in Equation 20:

$$\text{Removal efficiency (\%)} = \left(\frac{C_i - C_e}{C_i} \right) 100 \quad \text{Equation 20}$$

where C_i and C_e (mg/L) are the initial and equilibrium concentrations, respectively.

2.5 Results & Discussion

2.5.1 Characterisation of CFA

Coal fly ash (CFA) sample was mainly composed of quartz and mullite, which is common in bituminous coals [104]. Figure 2-1 (a) and (b) show the crystalline phases by XRD

and the morphology by SEM, respectively. The XRD patterns obtained for the raw CFA was verified using the locations of the characteristic quartz peaks at d_{100} ($20.86^\circ 2\theta$) and d_{101} ($26.65^\circ 2\theta$) reflections. Quartz and mullite are the main crystalline phases present in the sample as shown by the well-defined Bragg peaks in Figure 2-1(a). Figure 2-1(b) shows that the raw CFA has spherical shaped particles which is characteristic of coal fly ash samples, the smooth glassy layer of aluminosilicates is covered by needle shaped particles which is indicative of mullites [128,129].

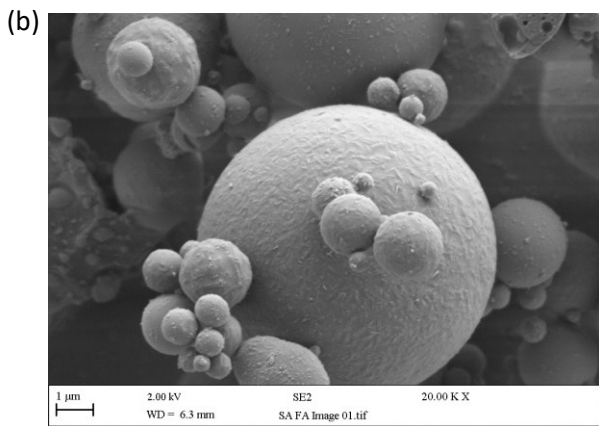
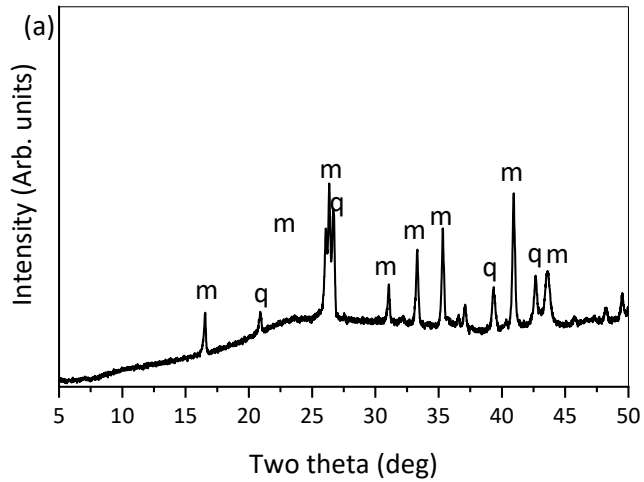


Figure 2-1 (a). XRD pattern and (b) SEM image of CFA. m mullite, q quartz.

The chemical composition of CFA, determined by EDX, is shown in Figure 2-2 where the major elements are SiO₂ (or Si) and Al₂O₃ (or Al). The major XRF mass composition of the oxides is 59 % SiO₂, 37.5 % Al₂O₃, 4.86 CaO, and 2.61 Fe₂O₃, the Si/Al ratio was 1.34. This coal fly ash is a class F fly ash in accordance to ASTM C618 classification [103] (c.f. Table 2-1). The BET surface area of CFA was 2.0 m²/g and an average pore width of 4.94 nm.

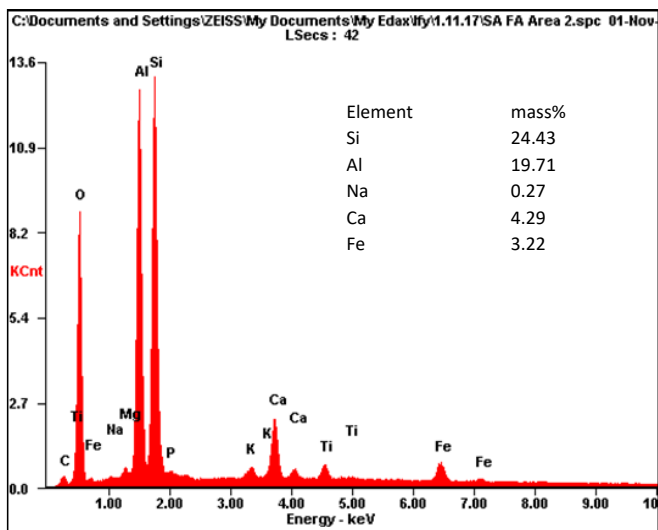


Figure 2-2. The chemical composition of raw CFA by EDX.

2.5.2 Zeolite synthesis using CFA

Zeolite syntheses was carried out using the alkali fusion prior to hydrothermal treatment route. Experimental conditions varied were the amounts of deionised water added and the duration of ageing. CFAw - t or CFZw - t were used to denote samples where w is the ratio of the amount of deionised water in the precursor ($w = 4, 10, 15, 20$), and t is the ageing duration (24 h, 48 h, 68 h, 72 h). CFAw - t is the fused and aged sample, CFZ w – t is the zeolite product. For instance, CFZ10 – 24 means the zeolite was prepared with a fused sample to deionised water ratio of 10 and aged for 24 h at ambient temperature before a 24 h thermal treatment in an oven.

2.5.2.1 morphological and crystalline phase changes

Figure 2-3 and Figure 2-4 shows the morphological and crystalline phase changes accompanying the transformation of raw CFA to NaX zeolites. With the fusion of CFA with NaOH at a ratio of 1:1.2, the particles lose their smooth surface appearance in addition to the

disappearance of the needle-like mullite particles, they now have a dense fuzzy-looking exterior as shown in Figure 2-3(a) and (b). By mixing the samples in deionised water for pH measurement, it was found that the raw CFA had pH in the range of 10.71 to 10.81 while the alkali fused sample (without washing) had a pH of 13.9 to 13.96 at 25 °C, which provides a very basic environment. Mixing the fused CFA with deionised water at a ratio of 1:10, ageing for 68 h and then washing and drying (without thermal treatment) gave the amorphous phases of the XRD pattern, CFA10 – 68, shown in Figure 2-4. In Figure 2-4, the dotted lines highlight the remarkable disappearance of most of the crystalline phases in the XRD pattern for raw CFA to the pattern for CFA10 – 68 which is indicative of the dissolution of the crystalline aluminosilicate phases. With a 24 h thermal treatment at 80 °C, the morphology and the amorphous phases reorganised into distinct crystalline structures. Figure 2-3(c) shows the morphology of the NaX zeolite formed which is devoid of any spherical shape that characterised

CFAs. The sphericity has now given way to structures with jutting sharp edges which have the octahedral shapes that faujasite zeolites are known for. Diffraction pattern-wise, the pattern CFZ10 – 68 now has the characteristic Bragg peaks for faujasite zeolites located from $d_{111}(6.10^\circ 2\theta)$ to $d_{993}(47.36^\circ 2\theta)$ as compared to the reference sample, ZRef – FAU (Figure 2-4).

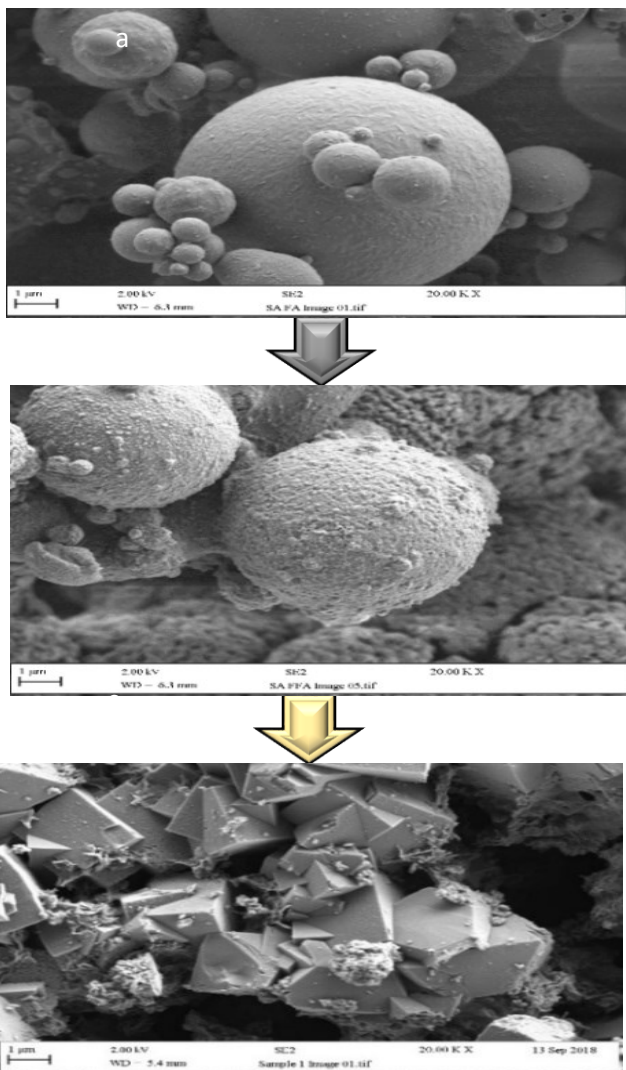


Figure 2-3. SEM images of the evolution of NaX from CFA. (a) Raw CFA, (b) NaOH fused CFA, and (c) CFZ.

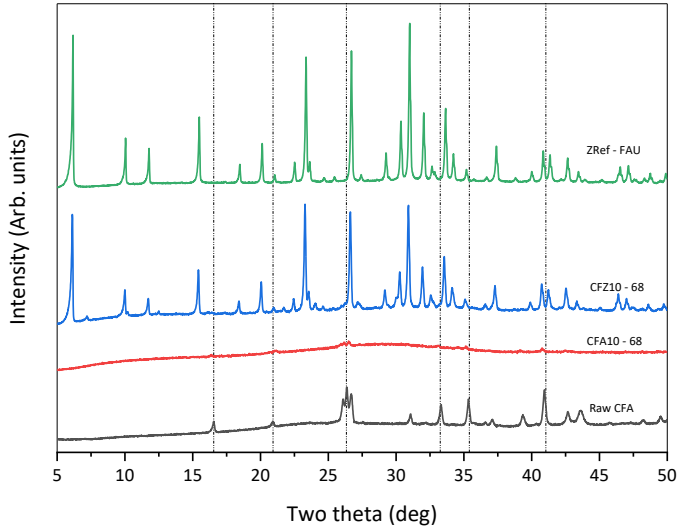


Figure 2-4. XRD patterns showing the crystalline phases of CFA transformation to FAU-type zeolite.

2.5.2.2 effects of precursor water ratio and extent of ageing

The use of water as a solvent in the hydrothermal synthesis of zeolites is a necessity. In testing the effects of the amounts of water added to the precursor and the extent in which samples are aged under ambient temperature followed by thermal treatment, the

experimental results are shown in the XRD patterns in Figure 2-5 with the corresponding SEM images in Figure 2-6.

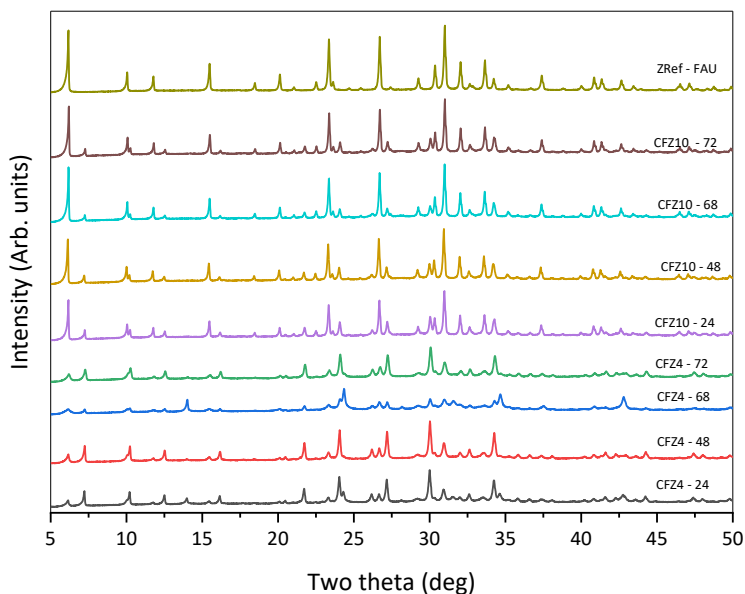


Figure 2-5. XRD patterns for water content of 1:4 to 1:10 and ageing duration of 24 h to 72 h.

Sample CFZ4 – 24, the zeolite resulting from the 1:4 water content, 24 h ageing, and 24 h hydrothermal treatment

at 80 °C, had a hodgepodge of zeolites that included low Bragg peak intensities for characteristic FAU XRD patterns (Figure 2-5), zeolite A (LTA) (d_{200} 7.18° 2 θ) and impurities of sodalite (d_{110} 14.1° 2 θ). This can be clearly seen in the SEM image of Figure 2-6(a) where sodalite particles resembling a thread ball are present together with FAU crystals. Using the same water content at a ratio of 1:4 but extending the ageing duration from 24 h to 48 h (CFZ4 – 48), 68 h (CFZ4 – 68) and 72 h (CFZ4 – 72), Figure 2-5 and Figure 2-6 (b-d) show the disappearance of SOD phases with only FAU and LTA zeolites present in the SEM images.

An increase in the water content from 1:4 to 1:10 ratio for 24 h (CFZ10 – 24), 48 h (CFZ10 – 48), 68 h (CFZ10 – 68), and 72 h (CFZ10 – 72) resulted in the progressive suppression of LTA and a more defined FAU crystallinity as shown in Figure 2-6 (e-h). Just as in the case of 1:4 water ratio, 24 h ageing even at a higher water content of 1:10 still produced SOD crystals as impurities as seen

by the thread ball - shaped particle beside the signature FAU octahedral shape in Figure 2-6 (e).

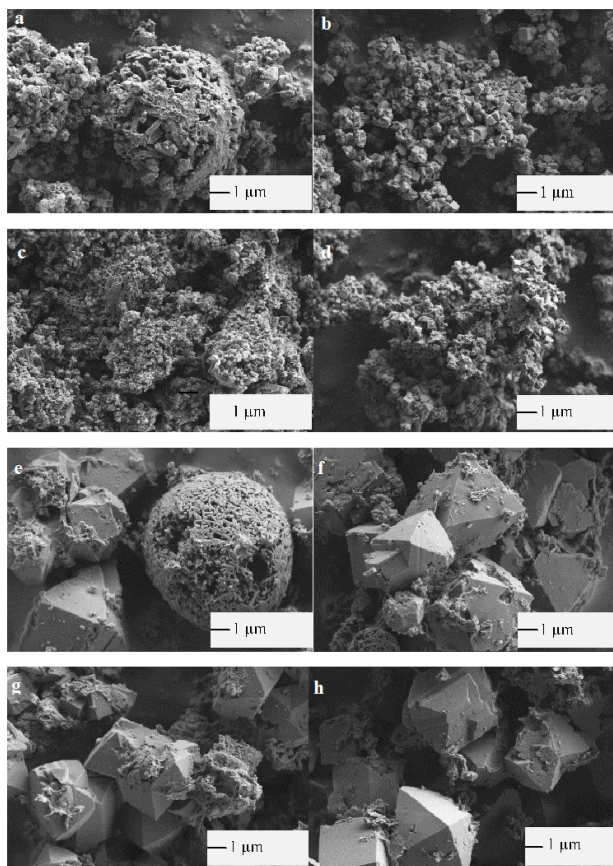


Figure 2-6. SEM images of (a) CFZ4-24, (b) CFZ4-48, (c) CFZ4-68, (d) CFZ4-72, (e) CFZ10-24, (f) CFZ10-48, (g) CFZ10-68, and (h) CFZ10-72 for water content and ageing duration variation.

Table 2-4 shows the Si/Al and BET results for the samples in Figure 2-5 and Figure 2-6 where Si/Al is the silicon to aluminum ratio, SA (m^2/g) is the surface area, SA_{ext} (m^2/g) is the external surface area, and V_{micro} (m^3/g) is the micropore volume. For all the prepared zeolite samples, Si/Al ratios were similar within the range of 1.22 to 1.28 which is comparable to the reference material, ZRef – FAU. The sample prepared using the lowest water content and the shortest ageing duration, CFZ4 – 24, had the lowest surface as should be expected since the SOD zeolite, in addition to LTA zeolite phases, almost overshadowed the FAU phase. SOD has a surface area between 17 to 20 m^2/g and the combination of the various crystalline particles gave a BET surface area of 83 m^2/g Table 2-4. The increase in water content and ageing duration of up to 1:10 and 68 h led to an increase in surface areas, micropore volumes, and the external surface areas. A 1:10 water content at 72 h of ageing resulted in a decrease in the surface area which could be because of the presence of LTA in the sample.

In terms of crystallinity, morphological and textural parameters, CFZ10 – 68 was selected as the optimal FAU (NaX) zeolite. This sample was used for adsorption experiments.

Table 2-4. Si/Al ratios and textural results of prepared zeolites.

Sample	Si/Al	SA (m ² /g)	SA _{ext} (m ² /g)	V _{micro} (cm ³ /g)
CFZ4-24	1.34	83 ± 1	49	0.017
CFZ4-48	1.25	151 ± 3	66	0.044
CFZ4-68	1.26	183 ± 3	63	0.058
CFZ4-72	1.22	205 ± 4	78	0.065
CFZ10-24	1.23	322 ± 8	78	0.126
CFZ10-48	1.28	389 ± 8	81	0.148
CFZ10-68	1.25	432 ± 9	76	0.172
CFZ10-72	1.27	397 ± 10	78	0.164
ZRef - FAU	1.16	626 ± 21	43	0.304

Thus, the water content and the ageing duration are very important parameters that affect the nucleation and crystallisation of fly ash zeolites. An increase in the ageing duration yields zeolites with more defined structures as does an increase in the water content.

In addressing the extent of water for the optimal duration of 68 h, a comparative study was made using fused fly ash to water mass ratios of 1:4, 1:10, 1:15, and 1:20. Figure 2-7 (a) and (b) shows the XRD patterns of post-aged (pre hydrothermal) and the zeolites subsequently formed after hydrothermal treatment, respectively.

In Figure 2-7 (a), due to the sufficient dissolution of crystalline phases, all the aged samples had a similar XRD pattern irrespective of the water content used. All showed a similar extent of dissolution of most of the aluminosilicate crystalline phases. Increasing the water content from 1:10 (CFZ10 – 68) to 1:15 (CFZ15 – 68) led to a product with higher FAU phase purity, higher Si/Al ratio and surface area (Table 2-5), hence a further

suppression of the LTA zeolite impurities (d_{200} 7.18° 2 θ) shown in Figure 2-7 (b).

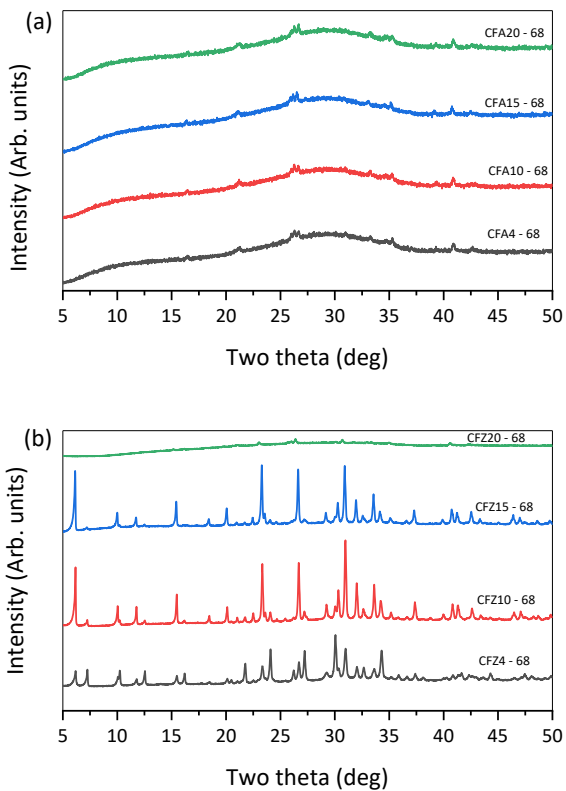


Figure 2-7. XRD patterns of samples prepared with different water contents (a) pre hydrothermal CFA and (b) zeolites CFZ.

CFZ15 – 68 FAU had an insignificant presence of LTA zeolite. The 1:20 ratio (CFZ20 – 68) showed no presence of any FAU crystals. Instead, it looked more like any of the pre hydrothermal samples in Figure 2-7 (a), a collection of amorphous products of aluminosilicates dissolution with a surface area of 27 m²/g, a conclusive indicator of the complete absence of FAU crystals. As seen in Table 2-5, increasing the water content from 1:4 to 1:15 ratio resulted in a progressive increase in the textural characteristics of the prepared zeolite. There exists a point of inflexion between 1:15 and 1:20 ratios in which zeolite nucleation is impossible to achieve.

Thus, the extent of water addition for CFA to FAU zeolite synthesis is 1:15. Above that ratio, the conditions to jumpstart zeolite nucleation and crystallisation process during hydrothermal treatment would be missing.

Table 2-5. Si/Al ratios and textural characteristics of CFZ-68 samples prepared with different water content.

Sample	Si/Al	SA (m ² /g)	SA _{ext} (m ² /g)	V _{micro} (cm ³ /g)
CFZ4-68	1.24	183 ± 3	63	0.058
CFZ10-68	1.25	432 ± 9	76	0.172
CFZ15-68	1.33	465 ± 13	88	0.194
CFZ20-68	1.27	27 ± 0.5	14	0.007

2.5.3 Nitrogen adsorption / desorption isotherms of zeolites from CFA

Since CFZ10 – 68 and CFZ15 – 68 were somewhat similar, their N₂ adsorption and desorption isotherms and BJH (Barrett, Joyner, and Halenda) derived pore size distributions were compared with the reference material, ZRef – FAU as shown in Figure 2-8(a).

ZRef – FAU has the characteristic type 1 physisorption isotherm indicative of microporous materials, the

structure is confirmed as a fully crystalline material without the presence of amorphous contaminants as evidenced by a pore volume of 0.304 cm³/g (Table 2-4). In contrast to the shape of the isotherm for ZRef – FAU, both CFZ10 – 68 and CFZ15 – 68 had isotherms that contained hysteresis loops (Figure 2-8a). These isotherms are type IIb instead of type IV(a) due to the absence of a plateau at high p/p⁰ [27,54,57]. The hysteresis for the two isotherms is characteristic of H3 loops suggesting the presence of slit-shaped pores, inter-particle pore condensation resulted in the narrow hysteresis loops. For CFZ10 – 68 and CFZ15 – 68, microporosity is indicated by the abrupt increase in the volume of adsorbed gas at low p/p⁰ where the micropore volumes (V_{micro}) were 0.172 and 0.194 cm³/g, respectively. The pore capacity of the prepared samples differed from the reference material; this is not so unexpected since the reference sample was prepared from pure sources of aluminosilicates. The BJH pore size distributions confirmed similarities in the pore structures of CFZ10 – 68 and CFZ15 – 68 as shown in

Figure 2-8(b). Although CFZ10-15 showed a slight improvement in FAU zeolite crystallinity as indicated by the XRD pattern and the higher micropore volume, both CFZ10-68 and CFZ15-68 had similar characteristics. Thus CFZ10 – 68 was chosen as the optimal FAU zeolite over CFZ15-68 in a bid to reduce water wastage. CFZ10 – 68 was used for the adsorption experiments.

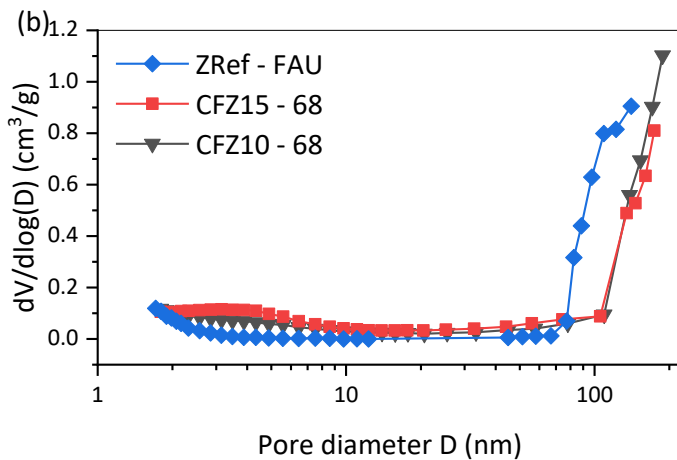
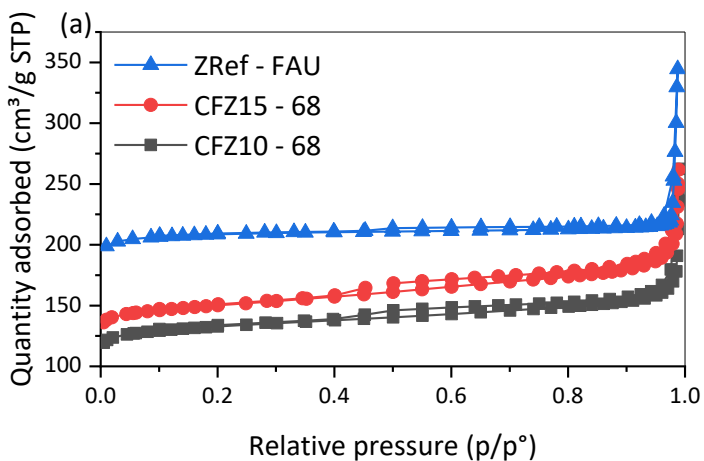


Figure 2-8. (a) N₂ adsorption/desorption isotherms (closed symbols, adsorption, open symbols, desorption) and (b) BJH Adsorption pore-size distributions of CFZ10-68, CFZ15-68, and ZRef-FAU samples.

2.5.4 Simultaneous Removal of Heavy Metals

In testing the efficacy of the prepared adsorbents, adsorption experiments were first carried out using raw CFA as an adsorbent to serve as a basis for comparison with the optimal FAU zeolite (CFZ10 – 68, Section 2.5.3) and the reference zeolite (ZRef – FAU).

The simultaneous removal of Cd(II), Co(II), Cu(II), Pb(II), and Zn(II) from aqueous solutions with initial concentrations from 5 to 100 mg/L is shown in Figure 2-9. Using an adsorbent loading of 5 mg/L, raw CFA indicated an adsorption preference of Pb(II) over the other cations when the initial concentration was above 20 mg/L with the trend $\text{Pb(II)} > \text{Cu(II)} > \text{Cd(II)} > \text{Zn(II)} > \text{Co(II)}$. Below that concentration, the decreasing adsorption trend was $\text{Cu(II)} > \text{Pb(II)} > \text{Zn(II)} > \text{Co(II)} > \text{Cd(II)}$. At the maximum concentration of 100 mg/L, the adsorption sites on CFA were not sufficient to accommodate the increased concentration of the competing cations. The low surface area of CFA resulted in the low removal efficiency of all the metals at 100 mg/L; none had up to 30 % removal at

that concentration. At 100 mg/L the percentage removed were Pb(II) 26.8 %, Cu(II) 18.3 %, Cd(II) 15.8 %, Co(II) 14.2 %, and Zn(II) 14.1 %.

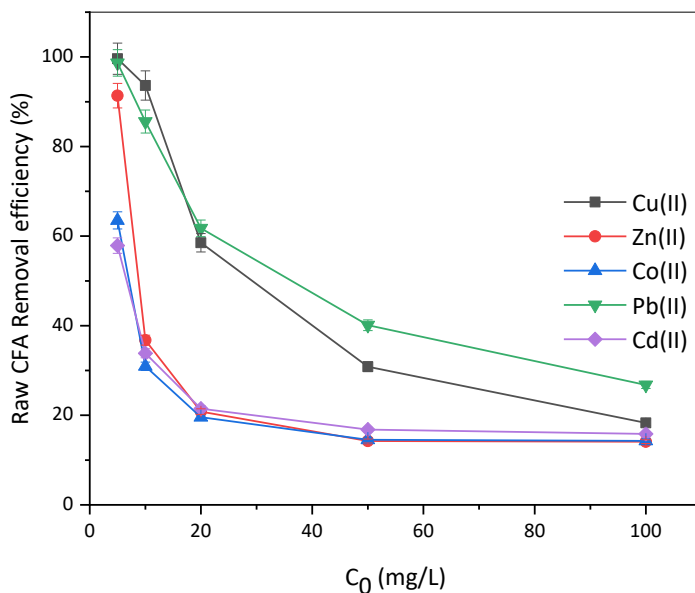


Figure 2-9. The removal efficiency of raw CFA from 5 – 100 mg/L.

The conversion of CFA to FAU zeolite resulted in the structural rearrangement of the CFA from a low surface area and spherical morphology to a FAU zeolite octahedral shape with its superior pore network system

and surface area. This is evidenced by the much-improved adsorption plots in Figure 2-10 and Figure 2-11.

To determine the effects of sorption duration on the competitive adsorption process, experiments were carried out from 10 to 180 min at an adsorbent (CFZ10 – 68 and ZRef – FAU) loading of 5 g/L and initial metal concentration of 200 mg/L in each metal (Figure 2-10). Within 10 min, CFZ10 – 68 achieved a removal efficiency almost 100 % for Pb(II), 83 % for Cu(II), 73 % for Cd(II), 43 % for Zn, and almost 29 % for Co(II) establishing a short interval trend of Pb(II) > Cu(II) > Cd(II) > Zn(II) > Co(II). On the other hand, the reference material (ZRef – FAU) achieved a removal efficiency of 97 % for Pb(II), 85 % for Cd(II), 72 % for Cu(II), 53 % for Zn(II), and 35 % for Co(II) with the 10 min adsorption interval trend of Pb(II) > Cd(II) > Cu(II) > Zn(II) > Co(II). As the adsorption proceeds, more cations occupy the adsorption sites until the sites are saturated leading to an equilibrium condition where no more cations can adhere to either the surface of the adsorbent or within the zeolite pore network.

Figure 2-10 (a) shows that for CFZ10 – 68, 10 min was sufficient to remove most of the Pb(II) but more time was required to remove a considerable amount of the other four cations.

Cu(II), Cd(II) and Co(II) achieved equilibrium to an extent by 90 min. Zn(II) seemed to be an outlier and did not fully achieve equilibrium even at 180 min, the percentage removal at 90 min was 72 %, 120 min was almost 76 %, 150 min 79 %, and 180 min 82 %. If that progression from 90 min is extrapolated, to achieve an almost 90 % theoretical removal of Zn(II) will require about 230 min. Taking all that into consideration, 90 min was chosen as the optimal duration for all five cations. In the case of ZRef – FAU Figure 2-10(b), equilibrium was achieved within 60 min but in order to make allowances for Co(II), 90 min was also chosen for the reference material; beyond that interval, no sufficient amounts are removed from the solution.

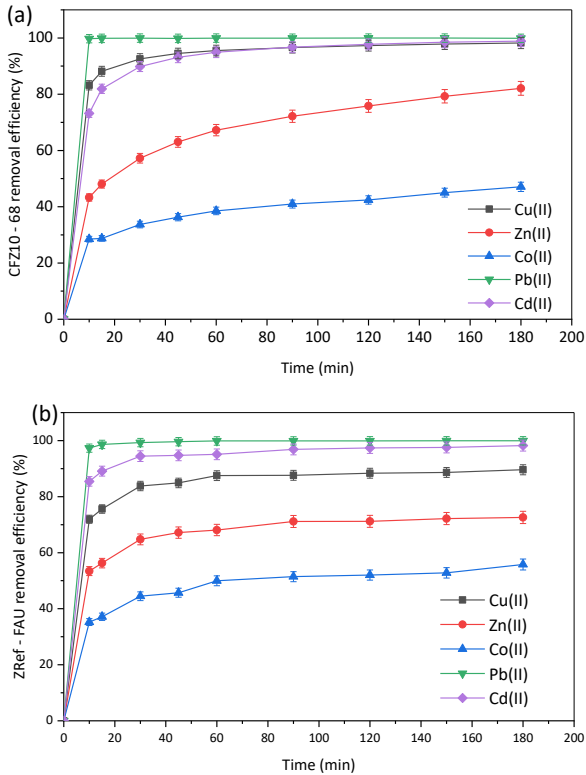


Figure 2-10. Simultaneous removal of five metals for 0 – 180 min at 5 g/L adsorbent loading and $C_0=200$ mg/L using (a) CZ10-68 and (b) ZRef-FAU.

Thus at the optimal duration of 90 min, CFZ10 – 68 achieved a removal efficiency 100 % for Pb(II), 96.6 % for

Cu(II), 96.7 % for Cd(II), 72 % for Zn, and almost 40 % for Co(II). Meanwhile ZRef – FAU achieved 100 % for Pb(II), 96.9 % for Cd(II), 87.6 % for Cu(II), 71.2 % for Zn(II), and 51.4 % for Co(II). Both adsorbents had the same trend for 10 min and 90 min. CFZ10 – 68 showed a selectivity of Cu(II) over Cd(II) while the opposite was the case for ZRef – FAU. Despite the similarities of the two adsorbents, the disparity in selectivity could be because of the subtle differences in their chemical compositions, CFZ10 – 68 that was prepared from a waste material had 2.19 mass % Fe_2O_3 and 3.45 mass % CaO while ZRef – FAU was devoid of those extras. The general selectivity of Pb (II) over the other four cations for the two adsorbents could be due to the radii sizes of the hydrated cations. For the adsorption of metals, it has been described that the relative adsorption affinity of Cd(II) is above that of Zn(II) and Cu(II) is higher than Co(II) [101]. The ability of the cation to form an inner sphere complex with the surface of the adsorbent, its hydrated ionic radii, and the

electronegativity are all factors that affect the selectivity of cation in a multicomponent adsorption system.

To determine the effects of initial concentration on the adsorbents, a quinary mix of the five metals was prepared with initial concentrations of 100 to 500 mg/L. The adsorption experiments at 90 min and 5 g/L adsorbent loading for CFZ10 – 68 and ZRef – FAU are shown in Figure 2-11(a) and (b), respectively. At the lowest concentration of 100 mg/L, both adsorbents had a substantial improvement in the percentage of metals removed in the multicomponent adsorption system. Figure 2-11(a) shows that at 100 mg/L, CFZ10 – 68 achieved the removal of 99.9 % Pb(II), 99.6 % Cu(II), 99.9 % Cd(II), 99.6 % Zn(II), and 96.5 % Co(II) from the aqueous solution establishing the trend Pb(II) > Cu(II) > Cd(II) > Zn(II) > Co(II). From Figure 2-11(b), ZRef – FAU achieved the removal of 100 % Pb(II), 99.7 % Cu(II), 99.9 % Cd(II), 99.7 % Zn(II), and 99.2 % Co(II) from the aqueous solution establishing the trend Pb(II) > Cd(II) > Cu(II) > Zn(II) > Co(II). The performance of the two adsorbents at 100

mg/L is similar for all the metals although ZRef – FAU removed almost 3 % more of Co(II) than CFZ10 – 68.

As the initial concentration was increased from 100 mg/L to 500 mg/L, both adsorbents showed signs of decline in efficiency as the concentrations of the five competing cations increased, saturating the available adsorption sites until no appreciable adsorption can be achieved. Since most of Pb(II) is adsorbed within the first 10 min, added to the preferential selectivity of Pb(II) over the other four competitors, Figure 2-11(a) and (b) shows the consistent total removal of Pb(II) over all the concentration range. With the other four cations in fierce competition for the adsorption sites that are not occupied by Pb(II), CFZ10 – 68 started declining rapidly below 90 % when the initial concentration got to 150 mg/L with 66% removal for Co(II), 200 mg/L with 72% removal for Zn(II), and at 350 mg/L with removal of 82.8 % Cu(II) and 75.5 % Cd(II) from the aqueous solutions.

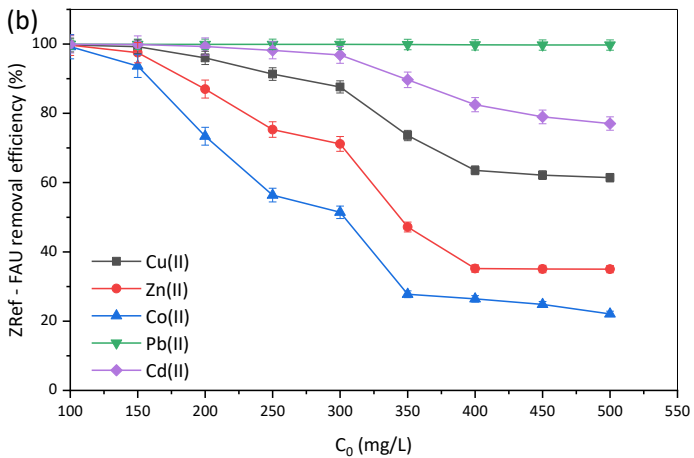
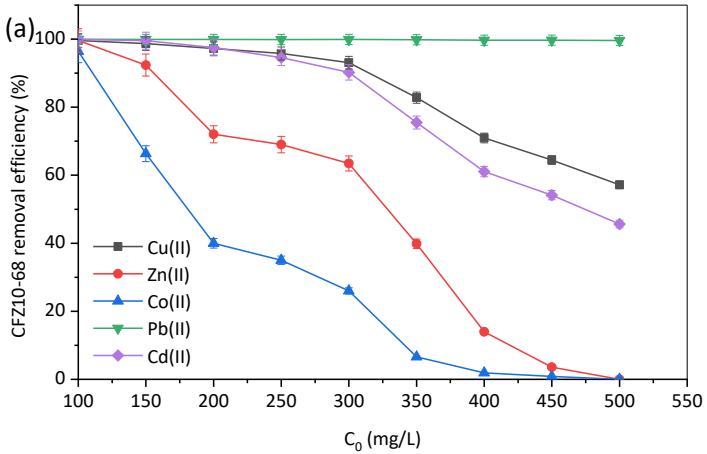


Figure 2-11. Simultaneous removal of heavy metals for 100 – 500 mg/L at 90 min and adsorbent loading of 5 g/L using (a) CZ10-68 and (b) ZRef-FAU.

With Pb(II) having a prime allocation of the adsorption sites, among the four competitors, Cu(II) followed by Cd(II) were preferentially adsorbed making Co(II) much less of a priority at 150 mg/L (where Cu(II) was 98.7 %, Cd(II) was 99.6 %, and Zn(II) was 92.4 %). At an initial concentration of 200 mg/L where Zn(II) became much less of a priority in the competition, Cu(II) was 97.3%, Cd(II) 97.5%, and Co(II) 40 %. Even though the first selectivity priority was Pb(II), at certain initial concentrations, other cations progressively attained lower selectivity.

All the previous experiments were carried at an adsorbent loading of 5 g/L. To determine the effects of different adsorbent loadings on CFZ10 – 68, Figure 2-12 shows the efficiency of that adsorbent when the loading was doubled and tripled at an initial concentration of 200 mg/L and 90 min duration. As usual, Pb(II) reached peak removal even with the lowest adsorbent loading of 5 g/L and so the loading effects on the least adsorbed, Co(II) and Zn(II), will be focussed on. From Figure 2-12, doubling

the adsorbent loading (from 5 g/L to 10 g/L) resulted in a 50 % increase for Co(II) and 30 % for Zn(II). The increase was as a result of the availability of more adsorption sites, these sites allowed the uptake of more of the cations with lower selectivity. In tripling the initial adsorbent loading to 15 g/L, there was no relevant effect on the uptake of Zn(II) because doubling the initial loading met the adsorption site quota for the removal of Zn(II) in a fiercely competitive multicomponent adsorption system. On the other hand, the extra available adsorption sites were relevant for most of Co(II) ions in the aqueous solution as shown in Figure 2-12.

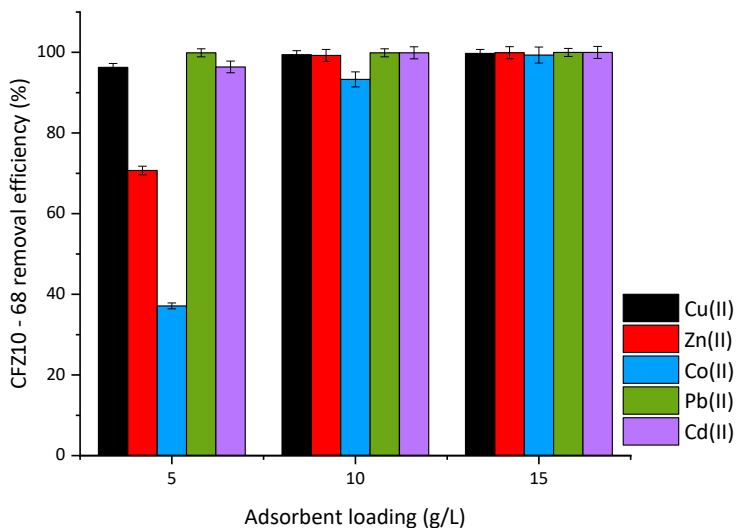


Figure 2-12. CFZ10-68 loading variation for 200 mg/L at 90 min for the simultaneous removal of five metals.

Table 2-6 shows the EDAX elemental composition of the adsorbent, CFZ10 – 68, before adsorption and after adsorption using the three loading variations. It shows the absence of the five metals in the adsorbent and their presence after the adsorption experiments indicating that sorption occurred. The results showed an inverse proportional relationship between the mass % of the

metals and the adsorbent loadings. This is because the more adsorption sites are available (from more adsorbents), there should (theoretically) be less adsorbates on any small portion of the adsorbent.

Table 2-6. EDAX elemental analysis (mass %) of CFZ10-68 pre and post adsorption experiments for different adsorbent loadings.

Element	CFZ10-68	5 g/L	10 g/L	15 g/L
Si	21.09	17.49	19.29	14.71
Al	17.28	14.84	17.03	12.24
Cu	-	1.99	1.50	1.00
Cd	-	1.71	1.19	0.76
Co	-	1.92	1.18	0.74
Pb	-	1.99	1.30	1.17
Zn	-	1.75	1.33	0.78

2.5.5 Adsorption kinetics

In fitting the adsorption data from CFZ10 – 68 to kinetic models, the correlation coefficient, R^2 , was used to validate the best model. Although the experimental data was fitted to five kinetics models, three of the models are presented in Table 2-7. Comparing second – order to pseudo second – order, the latter had a better fit than the former for all five metals which indicates physisorption as opposed to chemisorption as the sorption mechanism [27]. The second-order kinetics equation is an indicator that the rate of adsorption is directly proportional to the concentration squared hence the linear plot of $1/C_t$ vs t with k_2 as the slope which is the rate constant. In this instance, that relationship could be applicable as evidenced by the R^2 (Table 2-7) but the pseudo second-order had R^2 values that were much closer to unity. The pseudo second – order (PSO) rate constant (k_{PSO}), an indicator of how fast the adsorption occurs, has the highest value for Pb(II) at 0.89 g.mg/min which agrees with adsorption selectivity trend mentioned previously

for CFZ10 – 68. The difference between the theoretical and the experimental amount adsorbed at equilibrium (q_e) was below $\pm 2\%$, within a limit that underpins the validity of the PSO model. For instance, experimental q_e for Pb(II) was 39.97 mg/g while the theoretical value from the empirical PSO model was 40.0 mg/g. Another comparison is the experimental value for Cu(II) of 38.91 mg/g and PSO value of 39.68 mg/g as shown in Table 2-7. The intraparticle diffusion model gave a linear relationship for all the metals with R^2 in the range of 0.92 – 0.99 (Table 2-7).

Table 2-7. Adsorption kinetics parameters for CFZ10 - 68 at adsorbent load of 5 g/L, C₀= 200 mg/L, and 90 min duration.

Metal	Second - order		Pseudo second - order			Intraparticle diffusion	
	k_2 (L.min/mg)	R ²	q _e (mg/g)	k _{PSO} (g.mg/min)	R ²	k _{id} (mg.min ^{0.5} /g)	R ²
Pb(II)	0.100	0.972	40.000	0.893	1.000	0.412	0.971
Cd(II)	0.002	0.967	40.323	0.007	1.000	0.408	0.972
Cu(II)	0.001	0.997	39.683	0.012	1.000	0.3823	0.921
Zn(II)	0.000	0.997	34.722	0.002	0.997	0.478	0.986
Co(II)	0.000	0.961	19.531	0.004	0.995	0.852	0.989

2.5.6 Adsorption isotherms

The adsorption data had the best fit to the linearised form of the Langmuir isotherm and the model parameters obtained for a concentration range of 100 to 500 mg/L at 90 min and 5 g/L adsorbent loading shown in Table 2-8 and Table 2-9 for CFZ10 – 68 and ZRef – FAU, respectively. R², the criterion for the model validity, was almost unity for all the metals. Additional model validity

criterion is the agreement between the experimental data and the theoretical data. In this instance, there was a close agreement between the two, within an acceptable tolerance of $\pm 2\%$. For CFZ10 – 68, the maximum amount adsorbed at equilibrium, q_{\max} , for Cu(II) was 58.0 mg/g from the experiment while the Langmuir model gave 57.8 mg/g. q_{\max} followed the same previously established selectivity trends for both CFZ10 – 68 and ZRef – FAU (Section 2.5.4).

For both CFZ10 – 68 and ZRef – FAU, the q_{\max} for Pb(II) and Cu(II) were similar as shown in Table 2-8 and Table 2-9. ZRef – FAU q_{\max} for Cd(II) was about 38.5 % higher, 14.3 % for Zn(II), and more than doubled for Co(II) albeit still a low value compared to the adsorption of other metals.

Table 2-8. Langmuir adsorption isotherm parameters for CFZ10-68.

Metal	$q_{\max}(\text{mg/g})$	$K_L(\text{L/mg})$	R^2
Pb(II)	109.890 ± 1	3.250	0.987
Cd(II)	53.476 ± 0.5	1.222	0.999
Cu(II)	57.803 ± 3	0.700	1.000
Zn(II)	36.765 ± 2	0.324	0.979
Co(II)	12.240 ± 1.5	0.075	0.974

In comparison to literature on the use of zeolites from coal fly ash for water treatment, Visa et al. [87,89] found that the q_{\max} for Cu(II) and Cd(II) in a binary adsorption system was 58.1 mg/L and 16.1 mg/L, respectively while in a five metal system with Cu(II), Cd(II), Ni(II), Pb(II), and Zn(II), Pb(II) had the highest q_{\max} of 88.3 mg/L. Another study for the removal of Cu(II), Cd(II), Ni(II), and Pb(II) from aqueous solutions, Pb(II) was preferentially adsorbed with q_{\max} of 46.5 mg/L [98].

The Langmuir constant, K_L , is an indicator of the extent of interaction between the cations and the adsorption sites, the higher it is, the stronger the interaction. In both Table 2-8 and Table 2-9, the magnitude of K_L did not follow the selectivity trend. For CFZ10 – 68 (Table 2-8), K_L was of the decreasing order $Pb(II) > Cd(II) > Cu(II) > Zn(II) > Co(II)$ while in the adsorption selectivity order, $Cu(II)$ was preferred over $Cd(II)$. The K_L trend for ZRef – FAU (Table 2-9) was $Pb(II) > Cd(II) > Zn(II) > Cu(II) > Co(II)$ while the adsorption selectivity trend has $Cu(II)$ preferred over $Zn(II)$.

Table 2-9. Langmuir adsorption isotherm parameters for ZRef – FAU.

Metal	$q_{max}(mg/g)$	$K_L(L/mg)$	R^2
Pb(II)	103.093 ± 2	4.409	0.990
Cd(II)	74.074 ± 1	0.408	0.993
Cu(II)	57.803 ± 1	0.221	0.988
Zn(II)	42.017 ± 2	0.381	0.991
Co(II)	30.211 ± 1	0.092	0.996

This shows that even though there is a strong interaction between the adsorbent surface and the adsorbates, that does not necessarily imply immediate adsorption; other factors come into play. So in the case of Cu(II) for both adsorbents, even though K_L dictates otherwise, Cu(II) is still preferentially adsorbed over Cd(II).

2.6 Conclusions

Using pre alkali fusion hydrothermal synthesis route, CFA was used to prepare FAU zeolites where the effects of ageing, synthesis duration and the ratio of fused sample to water in the precursor were determined. The optimal FAU (NaX) zeolite, CFZ10-68, having a BET surface area of 432 m²/g and a micropore volume of 0.172 cm³/g was tested for its adsorption efficacy in a competitive simultaneous adsorption of five metals and compared to a reference zeolite, ZRef. The results proved that in a multicomponent adsorption system consisting of Pb(II), Cu(II), Co(II), Cd(II), and Zn(II) ions, FAU zeolite prepared from CFA can simultaneously remove five heavy metals

from aqueous solutions with high selectivity for Pb(II), Cu(II), and Cd(II) at high and low concentrations. CFZ10 – 68 had a removal trend of Pb(II) > Cu(II) > Cd(II) > Zn(II) > Co(II) while ZRef – FAU was Pb(II) > Cd(II) > Cu(II) > Zn(II) > Co(II). The adsorption mechanism was controlled by the pseudo second-order kinetics and intraparticle diffusion, the adsorption data was best fitted using the Langmuir isotherm.

The novelty of this work included the following:

- i. The maximum amount of water to successfully form faujasite zeolite from fly ash via alkaline fusion was determined.
- ii. Five metals were simultaneously adsorbed in a single step process.
- iii. Adsorption selectivity decreased in the order: Pb(II) > Cu(II) > Cd(II) > Zn(II) > Co(II).
- iv. Similar levels of each of the five metals were present on the zeolite after adsorption.

3 ZEOLITES FROM PEAT ASH

3.1 Literature Review

Peat is the sedentary accumulation of organic fuel formed by the partial decomposition of about 30% organic matter under waterlogged anaerobic and acidic conditions over extended periods [130,131]. In regions with temperatures below freezing points during winter periods, peat is formed from the prevailing vegetation like shrubs and mosses while peat from humid regions is formed from trees from the rain forest. Peatlands, areas with at least 20 cm layer depth where peat deposits are found at the surface, are necessarily covered with vegetation. The energy content of water drained, and ash free peat is between 20 – 22 MJ/kg of peat. Figure 3-1 shows a peatland (left) covered with vegetation and harvested peats (right) stacked in a count Roscommon, Ireland. The three areas of usage of peat are as fuel for power or heat generation, in the field of agriculture/horticulture, and as a source material in some

commonly used products like antibiotics and in balneotherapy (mineral baths).



Figure 3-1. (a)Natural peatland and (b) stacks of peat in county Roscommon, Ireland.

Globally, peatlands occupy approximately 2-3% total land area with appreciable deposits found in Russia, Canada, United States, Indonesia, United Kingdom, and Ireland among other countries as shown in Figure **3-2** [132].

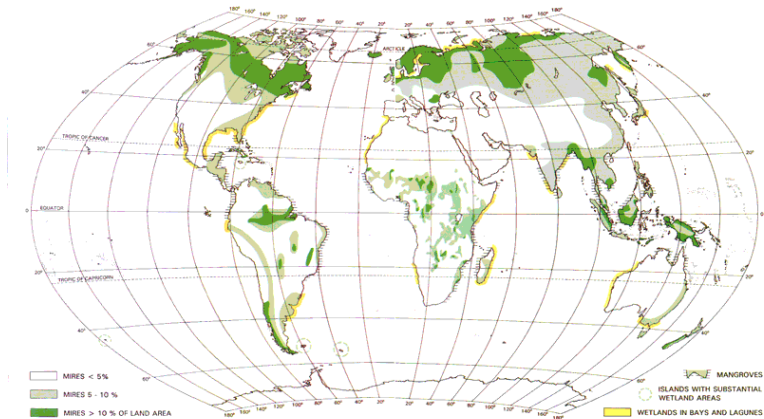


Figure 3-2 Global peat distribution [131]

About a decade ago, the three largest peat users in the European Union – Finland, Ireland, and Sweden, recorded a total use of 99% peat as fuel source for central heating power, condensing power, district heating, and residential heating [131,133]. In Ireland, the major use of peat is in heat and power generation; 8.5% of Ireland’s electricity from thermal power plants use peat as fuel source [134].

With the combustion of fossil fuels comes its detritus – in this case, peat ash which are presently disposed in landfills. The composition of peat ash includes minerals

that contain compounds of aluminium, iron, calcium, and various toxic metals like arsenic and cadmium [135,136].

Even though peatlands support the growth of vegetation and are excellent carbon sinks, such cannot be said of the carbon balance disruption from the production of peat ash from peat combustion for fuel. From an environment standpoint, the conversion of this silica-alumina waste into useful products that includes zeolite production will serve a multipurpose – the removal of hazardous wastes from the environment and the use of the converted product in environmental remediation.

Whereas zeolites have been produced from other combustion waste products such as coal fly ash and rice husk ash, none has been reported for peat ash. In this chapter, the first preparation of zeolites from peat boiler ash is reported; Appendix 1 (Paper 1) was based on the results from this chapter.

3.2 Materials

The chemicals used for zeolite synthesis and the adsorption experiments are as previously mentioned (Section 2.2). In addition to that, oxalic acid (CAS 144-62-7, 98% purity), acetic acid (CAS 64-19-7, analytical standard), and sodium aluminate NaAlO_2 (CAS 1302-42-7) 99.999% trace metals basis, were purchased from Sigma Aldrich. Nitric acid (HNO_3 , 70% w/w) and hydrochloric acid (HCl , >37% w/w) were purchased from Fluka. For zeolite syntheses, the two raw peat ash samples (samples A and B) used for the experiments were obtained from Ireland. Sample A was an industrial boiler waste, with added lime, from Bord na Móna PLC while sample B was the waste generated from the combustion of peat sods using domestic stoves in county Roscommon, Ireland.

Instrumental analysis was as previously mentioned in Section 2.2.

3.3 Synthesis

Pre-treatment involved calcination and acid leaching. Raw sample A was calcined at 600 °C to remove

carbonaceous materials. Sample A had more than 40 mass% calcium compounds ($\text{CaO} + \text{CaCO}_3$) as determined by XRF necessitating acid leaching (extraction). Acid leaching was attempted using hydrochloric acid, oxalic acid, acetic acid, and nitric acid at 85 °C, 95 °C, 90 °C, 100 °C, 105 °C, 110 °C, 120 °C, and at ambient temperature. For the bulk of this work, nitric acid was successfully used for Sample A at a sample to acid ratio of 1:16 at ambient temperature, a one - step extraction process. This was done by preparing a 5M nitric acid solution which was then poured into the calcined sample and stirred inside a fume cupboard for 5 h. Raw sample B was calcined at 800 °C and acid leached using 1:16 5M HCl acid reflux at 95 °C for 5 hours. After acid extraction, the products were washed, filtered, and dried in an oven at 80 °C. Dried samples were crushed using a mortar and pestle prior to alkali fusion.

Alkali fusion was performed using the acid leached samples (sample A and B) and NaOH in ratios of 1:1.2, 1:1.5, 1:1.8, 1:2.1, and 1:2.4. The well mixed mixture of

acid leached sample and powdered NaOH was placed in a furnace that was pre-heated for fusion at 600 °C for 3 h. In other experiments, sodium aluminate was added to decrease Si/Al ratio to 5, 2.5, and 1.

The NaOH fused sample was aged in polypropylene reactors by stirring a 1:5, 1:10, and 1:12 fused sample to deionised water ratios for specified durations at ambient temperature. The bulk of the work focused on a fused sample to deionised water ratio of 1:10. The duration for ageing was 0, 1, 3, and 7 days. In some experiments with Si/Al ratio of 1 for the precursor, after 3 days of agitated ageing by stirring, an additional step was added by static ageing in a 35 °C oven for 0, 1,2,3,4, and 5 days.

At the completion of ageing, the samples were transferred into an oven for hydrothermal treatment at 90°C for 24 h. In some experiments, hydrothermal treatment was extended to 48 and 72 h. Synthesis product recovery was by vacuum filtration followed by overnight drying in an oven. Finally, the zeolite samples were calcined in air at 550 °C for 4 h at a furnace

temperature ramp rate of 5 °C/min. The reference FAU zeolite was prepared as described in Section 2.3.

3.4 Adsorption Studies

A stock solution was prepared as previously discussed in Section 2.4. Appropriate amounts were diluted for standard solutions having concentrations of 100 to 400 mg/L. In 50 mL polypropylene bottles, 20 mL of the standard solutions and 0.1 g of each of the four adsorbents (sample A LTA/FAU and sample B LTA/FAU) were mixed and shaken for specified durations at ambient temperature. Initially an aqueous solution with the five metals having an initial concentration of 100 mg/L was used for the adsorption experiment for 60 min and adsorbent loading of 5 g/L. In another experiment, the initial concentration was increased from 100 mg/l to 400 mg/L. Additional experiments were also carried out using sample B FAU for a concentration range of 100 to 500 mg/L at 90 min and for an initial concentration of 200 mg/L from 10 to 180 min at adsorbent loading of 5 g/L.

At the end of the specified durations, the samples were filtered, and the metal concentration determined by ICP – OES.

The effect of adsorbent loadings was tested at 200 mg/L for 5, 10, and 15 g/L sample B FAU.

3.5 Results & Discussion

3.5.1 Characterisation of peat ash samples

Characterisation by XRD and SEM for calcined sample A and sample B is shown in Figure 3-3. Although both samples were peat based, their diffraction patterns and morphology were markedly different, some phases were exclusive to a particular sample. For instance, lime (CaO), merwinite ($\text{Ca}_3\text{Mg}(\text{SiO}_4)_2$), and calcite (CaCO_3) phases were found in sample A but no trace of them were seen in sample B as shown in Figure 3-3(a). The major XRF elemental composition (in mass%) of sample A was SiO_2 9.47 %, Al_2O_3 1.63 %, CaO 53.9 %, Fe_2O_3 4.81 %, and MgO 2.2 %. The presence of lime in sample A was due to its prior addition to peat to control alkalinity, sample A was

from an industrial boiler while sample B was from a domestic stove thus the high composition of CaO and CaCO₃ from XRF analysis. On the other hand, the magnetite (Fe₃O₄) phases shown in Figure 3-3(a) for Sample B was not found in sample A. XRF indicated that the major elemental composition (in mass%) of sample B is SiO₂ 12.7 %, Al₂O₃ 6.58 %, CaO 21.2 %, Fe₂O₃ 22.0 %, MgO 10.4 %, and P₂O₅ 1.87 %. The physical appearance of sample B was a bright reddish colour which comes from its high Fe content. Quartz (SiO₂) and anhydrite (CaSO₄) were the only phases in common between sample A and sample B. Anhydrite, lime, and calcite contributed to the high Ca presence in sample A while only anhydrite was the source of Ca in sample B. Magnetite singularly contributed to the high Fe content in sample B, compared to sample A, sample B had more than four times the amount of Fe in its composition than sample A. Hence the need to remove Ca and Fe impurities before zeolite synthesis.

The 20 kx SEM images of the calcined samples in Figure 3-3(b) show that the morphology is not well defined. The BET surface area and Si/Al ratio was 6 m²/g and 4.94, respectively for sample A. For sample B, the surface area was 22 m²/g while the Si/Al ratio was 1.64.

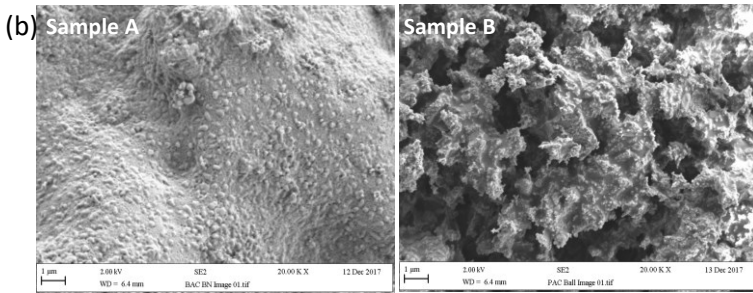
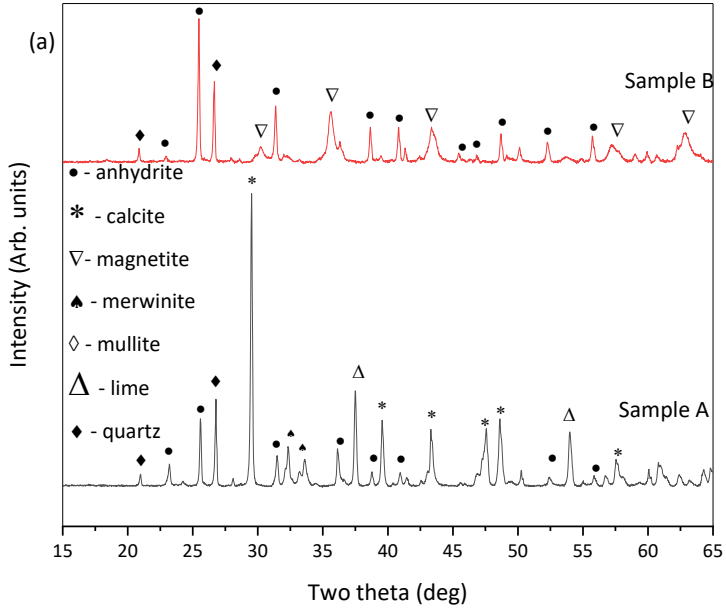


Figure 3-3. (a) XRD patterns and (b) SEM images of calcined samples.

3.5.2 Acid Extraction

Acid extraction (leaching) aimed at significantly reducing the amounts of Fe and Ca in samples A and B. The priority for sample A was the reduction of Ca while that of sample B, which had less than half the Ca of sample A, was the reduction of both Ca and Fe.

For sample A, the optimal condition with no additional heat requirement (i.e., at ambient temperature) was found to be 5M HNO₃ with calcined sample to acid ratio of 1:16 in a single step. The XRF elemental composition for acid leached sample A (mass %) was SiO₂ 71.4 %, Al₂O₃ 2.55 %, CaO 0.81 %, Fe₂O₃ 1.29 %, and MgO 0.21 %. With the room temperature acid leaching, the composition of CaO was reduced from 53.9 mass % to 0.81 mass %. Sample B Fe could not be significantly reduced using HNO₃, after attempts with many acids, the optimal condition was found to be heat-refluxed acid extraction at 95 °C using HCl at a 1:16 sample to acid ratio. The XRF elemental composition for acid leached sample B was

SiO₂ 76.9 %, Al₂O₃ 3.77 %, CaO 0.77 %, Fe₂O₃ 0.61 %, and MgO 0.35 %.

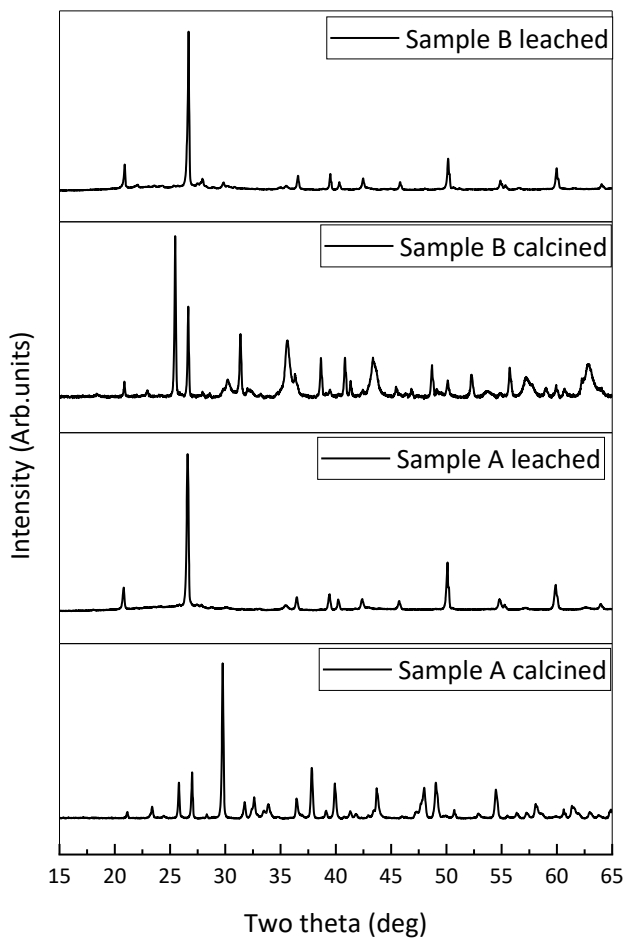


Figure 3-4. XRD patterns of calcined and acid leached samples.

Figure 3-4 shows the phase changes that accompanied acid leaching of the calcined samples. In comparing Figure 3-4 with the phase labels in Figure 3-3(a), the phases bearing Ca and Fe are noticeably absent in the acid leached samples. This confirms the results obtained from XRF regarding the considerable reduction of Fe and Ca in sample A and sample B.

The aggressive acid leaching of both samples to reduce the amounts of Ca and Fe led to an appreciable increase in the Si/Al ratio (sample A 28.0 and sample B 20.4). For FAU/LTA/GIS zeolite synthesis, that ratio had to be reduced by the addition of an alumina source.

3.5.3 Alkali Fusion

Alkali fusion requires an optimal sample to NaOH ratio to ensure the decomposition of quartz phases from the samples. This ratio was determined using varied amounts of the acid leached samples with NaOH. The ratios used were 1:1.2, 1:1.5, 1:1.8, 1:2.1, and 1:2.4. The ratio of 1:1.2 is the optimal ratio for CFA and it served as a reference point for peat ash [114,137].

Figure 3-5 shows the XRD patterns of the progressive dissolution of crystalline phases in sample A from the acid leached sample to the NaOH fusion at different ratios.

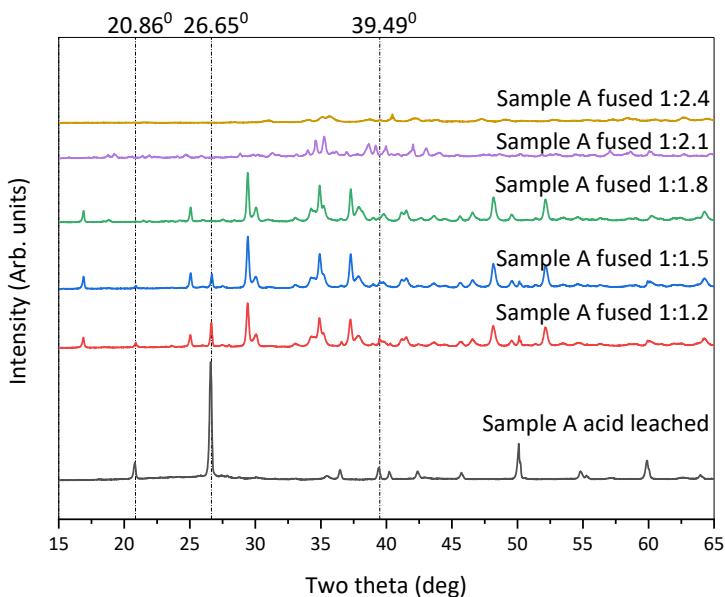


Figure 3-5. XRD patterns of sample A from acid leaching to NaOH fusion at different ratios.

The characteristic quartz phases shown in Figure 3-5, most especially the d_{101} (26.65° 2θ) reflection had a progressive reduction in intensity from 1:1.2 to a total

dissolution at 1:2.4 ratio. At 1:1.8 ratio, even though quartz peaks had significantly reduced, other crystalline phases were still present. Thus, a ratio of 1:2.4 was selected as the optimal NaOH fusion ratio.

Similarly, sample B was tested for varied ratios and the optimal NaOH ratio was found to be 1:2.4.

3.5.4 GIS and LTA synthesis

For sample A, after NaOH fusion experiments, deionised water was added to samples from the 1:1.2 to 1:2.4 (Section 3.5.3) at a sample to water ratio of 1:10, aged by stirring at ambient temperature for 68 h, and finally a 24 h hydrothermal treatment at 90 °C. It is noteworthy that the Si/Al ratio was not altered for the experiments here.

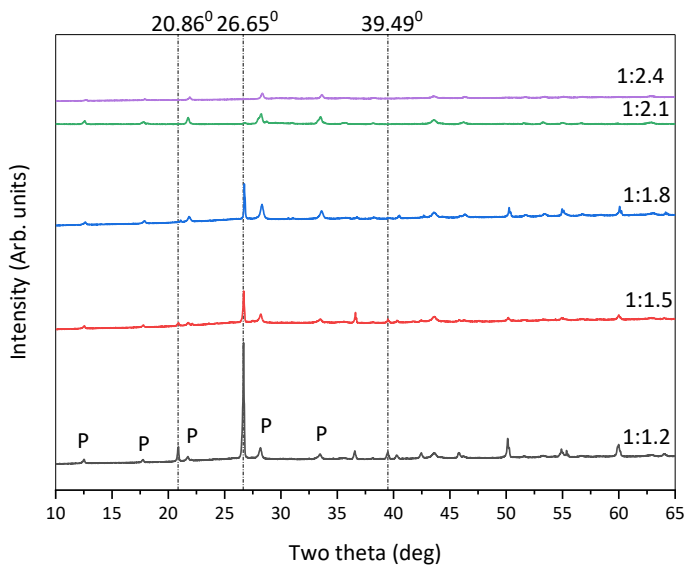


Figure 3-6. XRD patterns of the zeolite products for NaOH variations of sample A. P represents GIS zeolite.

In Figure 3-6, the zeolite synthesis of sample A fused with different ratios of NaOH yielded a mixed phase of GIS from 1:1.2 NaOH ratio until 1:2.1. At 1:2.4, most of the quartz phases had been dissolved during alkali fusion leading to a single GIS phase, albeit of a low intensity.

Similarly, sample B also yielded a mixed phase of quartz and GIS and a single-phase GIS when quartz was completely dissolved from the fused sample (ratio of 1:2.4).

Reducing the Si/Al ratios was done by the addition of sodium aluminate to obtain Si/Al ratios of 5, 2.5, and 1 prior to alkali fusion followed by ageing and hydrothermal treatment. For sample A, Figure 3-7 and Figure 3-8 (a) show a pure GIS phase for Si/Al ratio of 5, as the ratio reduced to 2.5, a mixed phase of GIS and LTA zeolites emerged. The GIS is characterised by its somewhat spherical and woolly morphology while the LTA is cubic. At the lowest ratio of 1, sample A produced a single LTA phase while sample B was a mixture of LTA (zeolite A) and NaX (zeolite X) as shown in Figure 3-7 and Figure 3-8 (b-d). LTA zeolite from sample B shows an intergrowth of NaX zeolite as can be seen in Figure 3-8(d) where one half of NaX octahedron shapes have developed on some of the LTA zeolites cubic morphology.

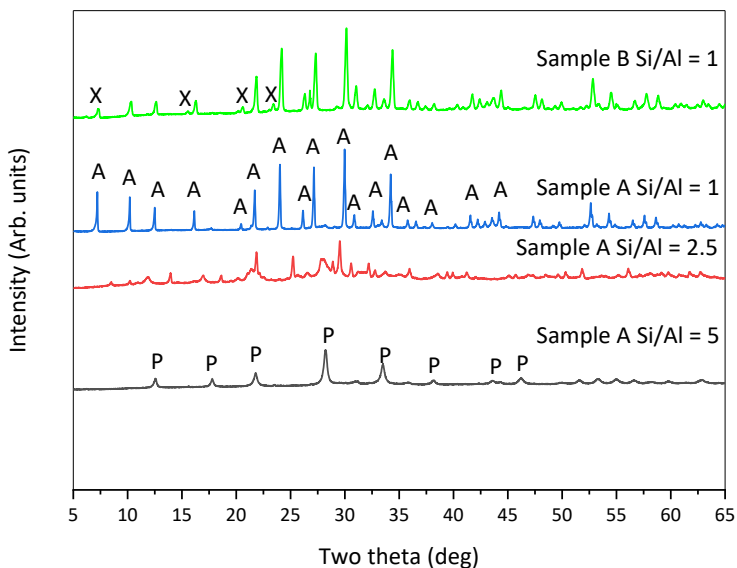


Figure 3-7. XRD patterns of LTA zeolites from sample A and sample B. A represents LTA, P GIS, and X NaX (FAU-type) zeolites.

That is an indicator of the possibility of crystalline phase change with the adjustment of synthesis conditions as will be seen in the next section. It is noteworthy that when the amount of deionised water used in the precursor was halved (from 1:10 to 1:5), sample A gave a product with a mixed phase of sodalite and LTA zeolite. The evolution of sodalite with LTA where synthesis water

is insufficient is related to what was observed in the preparation of FAU - type zeolites from coal fly ash (Section 2.5.2.2). For sample A, GIS had a surface area of 77 m²/g and Si/Al ratio of 2.83. Sample B on the other hand, had GIS surface area of 104 m²/g and Si/Al ratio of 2.83.

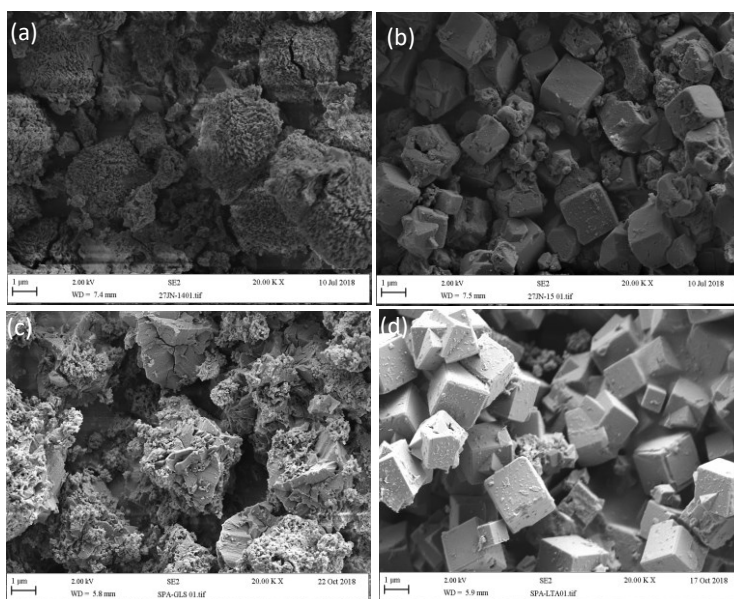


Figure 3-8. SEM images of GIS and LTA zeolites for sample A (a and b) and sample B (c and d).

3.5.5 FAU (NaX) synthesis

Additional synthesis step was carried out by ageing the Si/Al ratio of 1 sample A and sample B at 35 °C for 1 to 5 days and then hydrothermal treatment at 90 °C. The additional synthesis differed from the previous method via above ambient temperature ageing. Where the previous method involved ageing by stirring at ambient temperature for 68 h followed by hydrothermal treatment, in the additional step the samples were aged by stirring at ambient temperature for 68 h followed by static ageing at 35 °C for 1 to 5 days. That led to the formation of NaX zeolites for both sample A and sample B as shown in Figure 3-9 and Figure 3-10, only 0 to 4 d data are shown. The XRD pattern for the reference FAU-type zeolite, ZRef – FAU, is included for peak-by-peak comparison.

In both Figure 3-9 and Figure 3-10, without 35 °C, both samples mainly consisted of LTA zeolites. At 2 days extra synthesis step, there is a marked change in the crystallinity and morphology of both samples where NaX

zeolites begin to dominate, which was more pronounced in sample A than sample B. This marked change is also evidenced by the jump in the surface area of sample A from 84 m²/g to 471 m²/g as shown in Table 3-1.

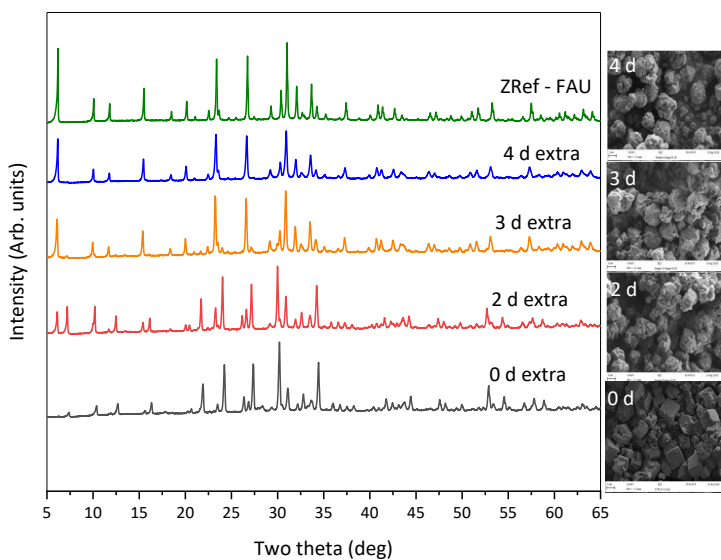


Figure 3-9. Sample A XRD patterns and SEM images for 0 to 4 days extra synthesis step.

Table 3-1. BET surface areas and Si/Al ratio for extra synthesis step.

Extra step	BET SA (m ² /g)		Si/Al	
	Sample A	Sample B	Sample A	Sample B
0 d	84.22	55	1.35	1.35
2 d	471.5	60.5	1.31	1.27
3 d	473.35	-	1.38	-
4 d	486.15	319.2	1.32	1.35
5 d	473.5	145.4	1.33	1.19

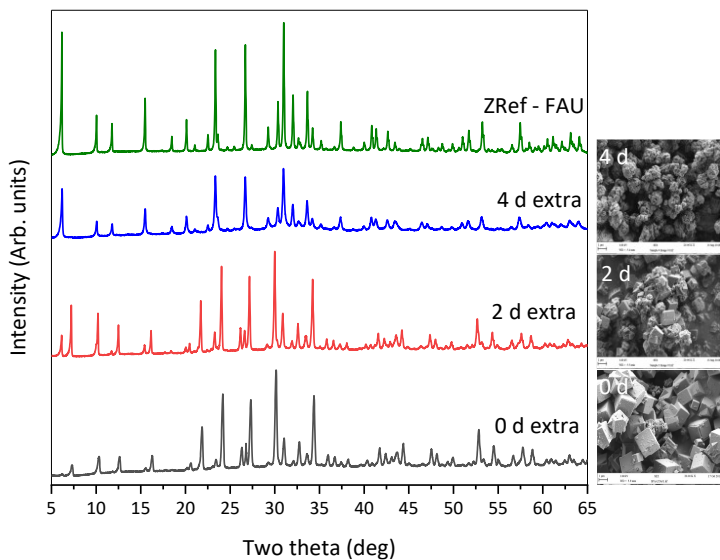


Figure 3-10. Sample B XRD patterns and SEM images for 0 to 4 days extra synthesis step.

Using the same conditions of the extra synthesis step, the changes were much more subtle for sample B where the surface area increased by 10%. The significant change for sample B was at 4 d extra step where the surface area became 319 m²/g. As the extra synthesis durations were increased, LTA progressively became suppressed and eventually at 4 d, only a single NaX phase was present for both samples as seen from the XRD patterns and the accompanied SEM images of Figure 3-9 and Figure 3-10. A peak-by-peak match of the faujasite peaks starting from location d₁₁₁(6.10° 2θ) for ZRef - FAU confirm the evolution and subsequent single NaX zeolite phases for both samples. Beyond 4 d, there seemed to be a point of inflection where NaX zeolite development stops, and the zeolite structure sheds its octagonal edges for a retrograde more rounded cubic-like form like the LTA zeolite, subtle for sample A but more pronounced for sample B with the surface area steeply dropping to 145 m²/g (Table 3-1). The optimal NaX (FAU - type) were 4 d

extra synthesis step products for both sample A and sample B.

3.5.6 Simultaneous Removal of Heavy Metals

The adsorption experiments for the uptake of Cd(II), Co(II), Cu(II), Pb(II), and Zn(II) from aqueous solutions were carried out for different concentration and time ranges using LTA and NaX (FAU) from samples A and B. Furthermore, extra experiments were carried out using sample B FAU for higher concentration ranges and durations. The percentage removal of each metal was calculated using Equation 22.

Figure 3-11 shows the performance of the four adsorbents (sample A LTA/FAU and sample B LTA/FAU) for the simultaneous uptake of the five cations at an initial concentration of 100 mg/L in each from 0 to 60 min and adsorbent loading of 5 g/L. For all four adsorbents, Pb(II), Cu(II), and Cd(II) were preferentially adsorbed within 10 min while Zn(II) and Co(II) were not. The FAU-

type zeolites with their superior surface areas and pore dimensions outperformed the LTA zeolites between 10 and 30 min, but after 30 min, sample A LTA outperformed FAU-types where the generally least adsorbed cations (Zn(II) and Co(II)) were completely removed from the aqueous solutions. Apparently, a longer adsorption duration (above 30 min) enabled the adsorbates to establish contact with the available sites and achieve equilibrium. This could be the reason why more of the poorly adsorbed metals were removed from the solution at the maximum adsorption extent as shown in Figure 3-11 (a-d). 60 min was sufficient to achieve equilibrium.

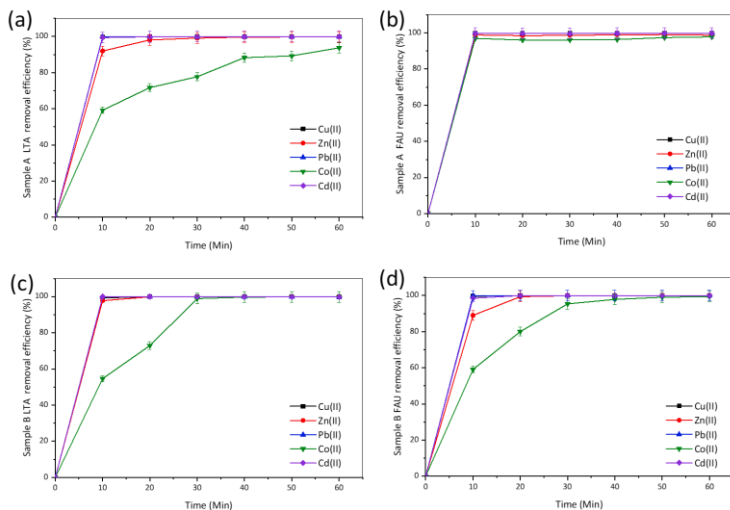


Figure 3-11. Removal efficiency at $C_0 = 100$ mg/L from 0 to 60 min and adsorbent loading of 5 g/L for (a-b) sample A LTA and FAU and (c-d) sample B LTA and FAU.

To investigate the performance of the adsorbents at concentrations above 100 mg/L, experiments were carried at 60 min but with initial concentrations ranging from 100 to 400 mg/L as shown in Figure 3-12.

With the exception of sample A FAU, all the other adsorbents (sample A LTA, sample B LTA, and sample B FAU) had a consistent adsorption trend of Pb(II) > Cu(II) >

Cd(II) > Zn(II) > Co(II) for all concentrations. Sample A FAU differed by preferentially adsorbing Cd(II) over Cu(II) with the trend Pb(II) > Cd(II) > Cu(II) > Zn(II) > Co(II) for 100 to 400 ppm initial concentrations (Figure 3-12). This departure in trend could be because sample A FAU has the highest specific surface area of 486 m²/g and the lowest Si/Al ratio of 1.32 as previously reported in Section 3.5.5.

For the simultaneous removal of those five metals in aqueous solutions, sample B FAU had the overall highest efficiency for Cd(II) and Zn(II) while sample B LTA was higher than its FAU counterpart in Pb(II) and Cu(II). Co(II), the least adsorbed metal, was best adsorbed by the FAU-types from samples A and B. Although the LTAs have smaller surface areas in comparison to faujasite zeolites, this experiment has shown instances where LTAs supersede FAUs in the uptake of heavy metals from aqueous solutions. In this case, sample B LTA (specific surface area 55 m²/g) was more efficient compared to

sample A FAU (specific surface area 486 m²/g) for all metals except Co(II).

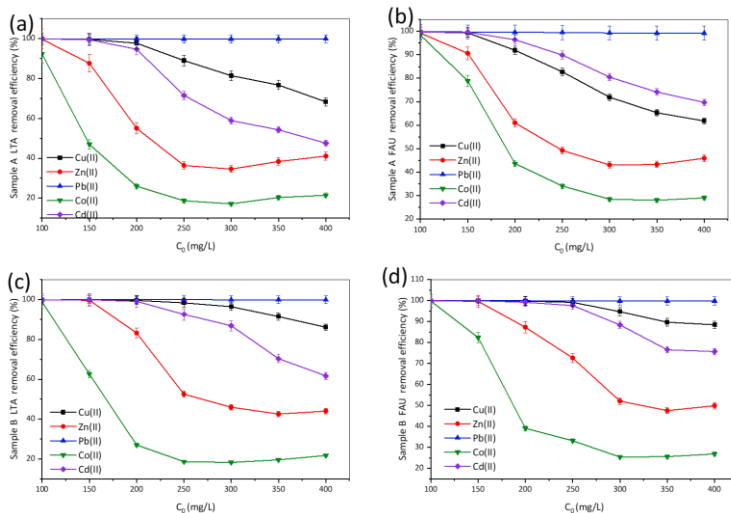


Figure 3-12. LTA and FAU removal efficiency at 60 min from 100 to 400 mg/L.

Sample B FAU was selected as the optimal adsorbent based on the overall uptake of the five metals.

The additional simultaneous adsorption studies for the optimal adsorbent, sample B FAU, using an initial

concentration of 200 mg/L from 0 to 180 min and 100 to 500 mg/L concentrations at 90 min with adsorbent loading of 5 g/L are shown in Figure 3-13.

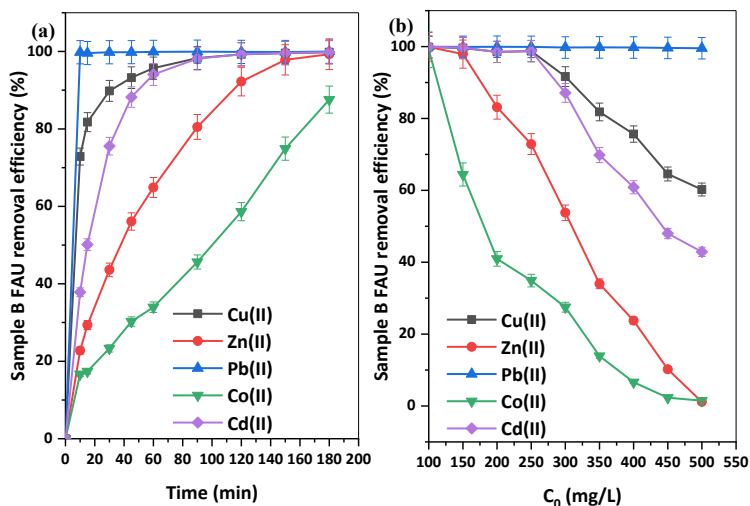


Figure 3-13. Efficacy of the simultaneous removal of five metals in aqueous solutions using sample B FAU at (a) 200 mg/L from 0 to 180 min and (b) 90 min for 100 to 500 mg/L.

In a time variation experiment at 200 mg/L in each of the five metals, Figure 3-13(a) shows that more than 99% of

Pb(II), 72.9% of Cu(II), 37.8% of Cd(II), 22.8% of Zn(II), and 16.7% of Co(II) were removed from the solution within 10 min. By the time the adsorption process reached 60 min, 95.7% of Cu(II), 94% of Cd(II), 64.9% of Zn(II), and 34% of Co(II) had been removed from the aqueous solution. A further 30 min increase in duration resulted in further removal of the less preferentially adsorbed cations, Zn(II) and Co(II) from 64.9% to 80% and from 34% to 45%, respectively. Doubling the duration from 90 min to 180 min resulted in the highest removal (more than 87%) of the least adsorbed metal, Co(II), and about 100% removal of the other four metals, this was probably because the adsorbates had more time to reach the available adsorption sites on the zeolite surfaces and the pore networks.

Although more than 87% of Co(II) was removed at 180 min, reducing the duration to 90 min and increasing the adsorbent loading led to a higher uptake of Co(II) as shown in Figure 3-14. Just doubling the adsorbent loading to 10 g/L at 90 min and 200 mg/L, more than 99% of

Cu(II), Zn(II), Pb(II), and Cd(II) were removed while about 97% of Co(II) was removed (Figure 3-14). Tripling the adsorbent load resulted in almost 100% simultaneous removal of all five metals (Figure 3-14). In considering the trade-off of the reduction of adsorption duration, amounts of adsorbent used, and the overall amounts of metals simultaneously removed, 90 min duration and 5 g/L adsorbent loading were selected.

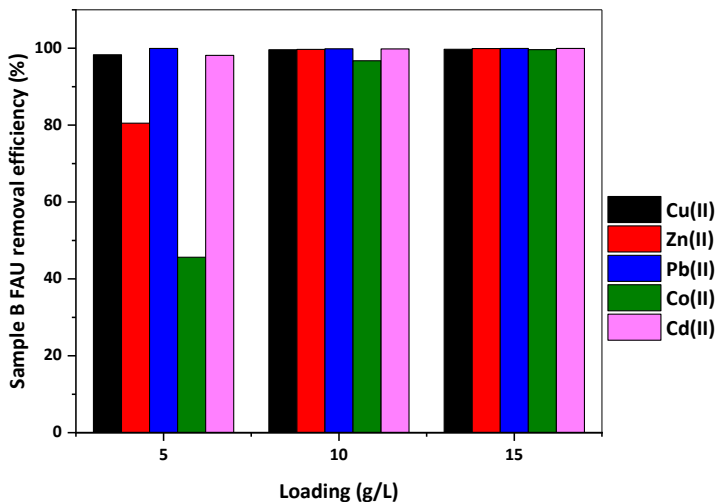


Figure 3-14. Adsorbent loading variation for sample B FAU at 200 mg/L and 90 min.

This concentration variation of 100 to 500 mg/L using sample B FAU with loading of 5 g/L and duration of 90 min resulted in the simultaneous removal of the five metals as shown in Figure 3-13(b). The trend was $\text{Pb(II)} > \text{Cu(II)} > \text{Cd(II)} > \text{Zn(II)} > \text{Co(II)}$. Even in the presence of four other competing cations with concentrations from 100 to 500 mg/L, Pb(II) had about 100% removal efficiency for sample B FAU. For Cu(II), Cd(II), Zn(II), and Co(II), the cation uptake efficiency of sample B FAU was inversely proportional to the initial concentration; an increase in concentration resulted in a decrease in the amounts of metals removed (Figure 3-13b). Contrasting the efficacy of sample B FAU at an initial concentration of 400 mg/L at 60 min (Figure 3-12d) and at 90 min (Figure 3-13b), Pb(II) uptake was the same since that cation has the highest selectivity, extending the adsorption duration to 90 min showed no improvement for the other cations justifying the choice of 60 min as the optimal adsorption duration.

The XRF elemental analysis of sample B FAU before and after the adsorption process is shown in Table 3-2. The five metals of interest were not detected in the adsorbent prior adsorption, after the adsorption experiment, those metals were detected which was an indication that adsorption occurred.

Table 3-2. XRD oxides (mass %) of sample B FAU pre and post adsorption at 5 g/L adsorbent loading.

	SiO ₂	Al ₂ O ₃	ZnO	CuO	Co ₂ O ₃	PbO	CdO
Before	30.40	24.70	0.00	0.00	0.00	0.00	0.00
After	45.70	35.20	3.35	3.37	3.51	3.11	2.37

The comparative study of the adsorption performance of the zeolites (LTA and FAU) obtained from peat ash and FAU obtained from coal fly ash (Section 2.5.4) is summarised in Table 3-3. It was found that at an initial concentration of 400 mg/L, an adsorbent loading of 5 g/L, and a 60 min duration, the peat ash zeolites were

generally more efficient than that from coal fly ash. Pb(II) uptake was similar for coal fly ash and peat ash zeolites. The most important difference was in the uptake of Co(II), a cation with the lowest selectivity for all the zeolites prepared from both waste materials. The coal fly ash FAU zeolite, CFZ10 – 68, removed 1.99 % of Co(II) while the peat based zeolites removed more than 20 %. The other least adsorbed metal, Zn(II), had a similar trend. CFZ10 – 68 removed 13.96 % Zn(II) while the peat based zeolites removed more than 40 % of Zn(II). In both instances, the peat-based FAU-type zeolites had the highest uptake of the least adsorbed metals recorded for FAU-type zeolites from both waste materials.

Table 3-3. Comparison of metal uptake (%) by zeolites from coal fly ash and peat ash at initial $C_0 = 400$ mg/L, adsorbent loading of 5 g/L and 60 min duration.

Adsorbate/ Adsorbent	CFZ10 - 68	Sample	Sample	Sample	Sample
		A LTA (%)	A FAU (%)	B LTA (%)	B FAU (%)
Pb(II)	99.68	99.83	99.46	99.95	99.77
Cu(II)	70.96	68.23	61.80	86.05	88.44
Cd(II)	61.07	47.57	69.74	61.67	75.69
Zn(II)	13.96	41.08	45.88	43.99	49.91
Co(II)	1.99	21.46	29.03	21.76	26.94

The decreasing trend of the surface area for the adsorbents on Table 3-3 is A FAU > CFZ10 – 68 > B FAU > A LTA > B LTA. The Si/Al ratio is of the decreasing order A LTA > B LTA = B FAU > A FAU > CFZ10 – 68. This shows that a larger surface area does not necessarily imply a higher uptake of metals in a competitive sorption system. In addition to the importance of the surface areas and pore sizes of zeolites, factors like zeolite extra framework cations, adsorbent/adsorbate complexation, hydrated ionic radii, and electronegativity affect the adsorption

process. Those factors might have determined the overall higher performance of peat-based zeolites over FAU zeolite from coal fly ash as shown on Table 3-3.

3.5.7 Adsorption isotherms

The adsorption data for sample A LTA/FAU and sample B LTA/FAU for the simultaneous uptake of the five heavy metals at initial concentrations of 100 to 400 mg/L was modelled using Langmuir and Freundlich isotherms, their model parameters are shown from Table 3-4 to

Sample	Langmuir			Freundlich		
	q_{\max} (mg/g)	K_L (L/mg)	R^2	n	K_F (mg/g)	R^2
A LTA	26.603	0.069	0.924	36.873	21.032	0.313
A FAU	32.268	0.072	0.963	15.193	20.538	0.714
B LTA	31.456	0.215	0.985	27.027	25.339	0.597
B FAU	35.714	0.562	0.989	16.359	26.555	0.857

Table 3-8. The model fitting of the adsorption data for each cation was compared for all four adsorbents.

Table 3-4 shows that the most adsorbed metal, Pb(II), had the best fit with Freundlich adsorption isotherm where the correlation coefficient, R^2 , was close to unity for all the adsorbents. Except for sample A LTA, the Langmuir isotherm was similarly applicable to the other adsorbents. The preference of the Freundlich isotherm over Langmuir for Pb(II) is indicative of surface heterogeneity and an exponential spread of the available adsorption sites [68] of the LTA and FAU-type adsorbents. The overestimation of q_{max} by the LTA zeolites when

compared to the FAU-type zeolites (Table 3-4) emphasises the relatively poor fit of the Langmuir model. Thus the Freundlich empirical model is a better fit for Pb(II). The higher values of the Freundlich constant, K_F , and the lower values of the Freundlich adsorption parameter n for the LTAs are indicative of a favourable adsorption process towards Pb(II) ions.

Table 3-4. FAU-type and LTA zeolites adsorption isotherm parameters for Pb(II).

Sample	Langmuir			Freundlich		
	q_{\max} (mg/g)	K_L (L/mg)	R^2	n	k_F (mg/g)	R^2
A LTA	156.006	0.976	0.579	1.509	79.577	0.931
A FAU	94.073	1.163	0.975	2.210	46.172	0.996
B LTA	140.845	1.625	0.940	1.506	98.278	0.963
B FAU	86.505	4.266	0.960	2.522	71.332	0.979

The adsorption data of Cu(II) was best fitted with the Langmuir isotherm as shown in Table 3-5. Even though the Freundlich isotherm could interchangeably be

applicable, the Langmuir empirical model gave correlation factors that were the closest to unity for Cu(II). The Cu(II) experimental q_{\max} data were in close agreement with the empirical data affirming the choice of Langmuir as the best adsorption isotherm. For instance, the Cu(II) experimental q_{\max} ($q_{\max,\text{exp}}$) values for sample A FAU was 45.1 mg/g while that of sample B LTA was 64.4 mg/g and sample B FAU 66.3 mg/L, when compared with the model values in Table 3-5, they are reasonably close.

Table 3-5. FAU-type and LTA zeolites adsorption isotherm parameters for Cu(II).

Sample	Langmuir			Freundlich		
	q_{\max} (mg/g)	K_L (L/mg)	R^2	n	K_F (mg/g)	R^2
A LTA	54.795	0.387	0.998	7.394	29.177	0.983
A FAU	48.426	0.253	0.997	8.273	26.222	0.973
B LTA	69.109	0.886	0.999	5.358	35.252	0.964
B FAU	68.259	1.112	0.996	6.255	38.375	0.968

Another cation with high adsorption selectivity is Cd(II), and similarly to Cu(II), Table 3-6 shows that the data was best fitted with the Langmuir empirical model with R^2 in the range of 0.997 to 1. The $q_{\max, \text{exp}}$ were in close agreement with that obtained from the empirical relationships.

Table 3-6. FAU-type and LTA zeolites adsorption isotherm parameters for Cd(II).

Sample	Langmuir			Freundlich		
	q_{\max} (mg/g)	K_L (L/mg)	R^2	n	K_F (mg/g)	R^2
A LTA	37.750	0.678	0.999	13.827	26.767	0.884
A FAU	55.006	0.328	0.997	7.175	28.360	0.970
B LTA	49.432	7.781	1.000	8.971	31.500	0.912
B FAU	57.870	0.906	0.997	7.757	33.978	0.964

The model fitting for the least adsorbed metals, Zn(II) and Co(II), are shown in Table 3-7 and

Sample	Langmuir			Freundlich		
	q_{\max} (mg/g)	K_L (L/mg)	R^2	n	K_F (mg/g)	R^2
A LTA	26.603	0.069	0.924	36.873	21.032	0.313
A FAU	32.268	0.072	0.963	15.193	20.538	0.714
B LTA	31.456	0.215	0.985	27.027	25.339	0.597
B FAU	35.714	0.562	0.989	16.359	26.555	0.857

Table 3-8 . Freundlich isotherm was a poor fit for both metals, more so for Co(II) than for Zn(II). The Langmuir isotherm was the best fitting for the adsorption of Zn(II) and Co(II) on sample A LTA/FAU and sample B LTA/FAU.

Table 3-7. FAU-type and LTA zeolites adsorption isotherm parameters for Zn(II).

Sample	Langmuir			Freundlich		
	q_{\max} (mg/g)	K_L (L/mg)	R^2	n	K_F (mg/g)	R^2
A LTA	26.603	0.069	0.924	36.873	21.032	0.313
A FAU	32.268	0.072	0.963	15.193	20.538	0.714
B LTA	31.456	0.215	0.985	27.027	25.339	0.597
B FAU	35.714	0.562	0.989	16.359	26.555	0.857

Table 3-8. FAU-type and LTA zeolites adsorption isotherm parameters for Co(II).

	Langmuir			Freundlich		
	q_{\max}	K_L	R^2	n	k_F	R^2
	(mg/g)	(L/mg)			(mg/g)	
Sample A LTA	14.294	0.034	0.884	-	21.280	-
Sample A FAU	20.614	0.092	0.973	-	20.576	-
Sample B LTA	14.013	0.049	0.905	-	20.647	-
Sample B FAU	18.818	0.103	0.971	-	20.448	-

3.5.8 Adsorption kinetics

The adsorption kinetics parameters for sample B FAU at an initial concentration of 200 mg/L and time 0 to 180 min (Section 3.5.6) was modelled using pseudo first-order, second – order, pseudo second – order, and

intraparticle diffusion models. The results are tabulated in Table 3-9.

Modelling the adsorption kinetics data using the Lagergren equation popularly known as the pseudo second order (PSO) kinetics equation gave a poor fit and underestimation of the equilibrium sorption amount, q_e (Table 3-9). That model assumes that adsorption occurs at localised sites without the interaction of the adsorbates. Since the correlation coefficient values, R^2 , were quite low for Pb(II) and Co(II), and reasonably high for Cu(II), Cd(II), and Zn(II), the PSO model is invalid for the former and valid for the latter metals.

An attempt was made to model the data using the second-order rate equation which stipulates the proportional relation of the rate of adsorption with the concentration squared. Apparently, that relationship is not applicable to the kinetics of the uptake of the five metals as shown in Table 3-9.

The pseudo second-order (PSO) model had the best fit for all but one of the metals – Co(II) (Table 3-9). The PSO rate constant trend is consistent with the adsorption selectivity trend for the adsorbent, sample B FAU, where the highest value attributed to Pb(II) is a conclusive indicator of how fast Pb(II) was removed from the aqueous solution. This model is an indicator of chemisorption as opposed to physisorption as the mechanism that drives the sorption process.

Thus, chemisorption is the dominant adsorption mechanism. This does not necessarily mean that physisorption did not occur, it is highly possible that they both occurred which might account for the higher uptake of some of the peat-based zeolites with lower surface areas.

The intraparticle diffusion model fitting was particularly poor for Pb(II) (Table 3-9), an indication that the overall adsorption process was not diffusion – controlled.

Table 3-9. Adsorption kinetics parameters for sample B FAU.

		Pb(II)	Cu(II)	Cd(II)	Zn(II)	Co(II)
Pseudo first-order	q_e (mg/g)	0.094	7.677	17.705	41.841	45.520
	k_{PFO} (1/min)	0.002	0.006	0.008	0.006	0.004
	R^2	0.540	0.972	0.959	0.981	0.803
Second order	k_2 (L/mg.min)	0.047	0.012	0.014	0.003	-
	R^2	0.512	0.809	0.778	0.632	0.738
Pseudo second order	q_e (mg/g)	40.000	40.816	43.860	52.356	52.083
	k_{PSO} (g/mg.min)	0.568	0.006	0.002	-	-
	R^2	1.000	1.000	0.997	0.993	0.739
Intraparticle diffusion	k_{id} (mg.min ^{0.5} /g)	1.763	0.910	2.889	3.184	2.514
	R^2	0.360	0.788	0.824	0.988	0.949

3.6 Conclusions

GIS, LTA, and FAU zeolites were prepared via pre alkali fusion and hydrothermal route for the first time using peat ash samples. The zeolite framework type formed was as a result of a systematic variation of precursor compositions and ageing temperature. Sample A and sample B yielded zeolite P (GIS) from a 1:1.2, 1.5, 1.8, 2.1, and 2.4 NaOH to acid leached peat ash ratio. The optimal ratio was found to be 1:2.4. With the addition of sodium aluminate to boost the severely depleted Al after acid leaching, zeolite A (LTA/NaA) was prepared by changing the Si/Al ratio of both samples. With Si/Al ratio of 1, a single crystalline phase of LTA was formed for sample A and sample B. For an additional step of extra ageing at 35°C, FAU-type zeolites resulted with increasing purity as the duration was increased to 4 days for both samples.

The four peat ash-based LTA and FAU zeolites (samples A and B) were used to simultaneously remove Cd(II), Cu(II), Co(II), Pb(II), and Zn(II) from aqueous solutions. Generally, Langmuir adsorption isotherm and the pseudo

second-order kinetics were valid for the adsorption process for zeolites from peat-based ash.

This research established the literature on the first zeolites synthesised from peat ash and the least energetic acid extraction of CaO from ash samples. The performance of the zeolites from peat ash were found to be superior to that of faujasites from coal fly ash in the uptake of the five heavy metals used in this study.

4 ZEOLITES FROM GEOPHAGICAL CLAY

4.1 Literature Review

Geophagy, a subset of a psychological condition called pica, is an eating disorder associated with cravings for earthy materials like clay and soil deposits practiced worldwide in different ethnic and cultural groups for centuries [138–142]. In sub-Saharan Africa, up to 84% of women, whose cravings are exacerbated during pregnancy and lactation, ingest geophagical clays [140,142]. The consumption of these clays starts as a need for supplementing essential minerals for the body and other medicinal purposes that include antidiarrheal applications but it progresses to a compulsory drive to eat these clays [141,142].

Natural clays are minerals commonly found in environments with soils and sediments. They are hydrated phyllosilicates (sheet silicates) formed by the physical and chemical changes resulting from the interactions of rock and water, a process known as ‘diagenesis’ followed by the hydrothermal alteration of

rocks. The structure of a clay mineral is composed of two-dimensional layers of tetrahedral (SiO_4) or octahedral (AlO_6) structural sheets coordinated with oxygen. A 1:1 layer structure is used to describe units of alternating single tetrahedral and octahedral sheets (TO) such as those found in kaolinites, planar halloysites, and nacrites [143]. A 2:1 structural arrangement is used to describe clays with two tetrahedral units for every octahedral unit (TOT) such as those found in vermiculites and smectites which have hydrated exchangeable cations in their framework [143]. Figure 4-1 shows the structural arrangement of a 1:1 and a 2:1 layer structure where the octahedral and tetrahedral cations are represented by M and T. O_a and O_b represent the tetrahedral at the apex and the base, respectively, and O_{oct} is the octahedral in the anionic position [144].

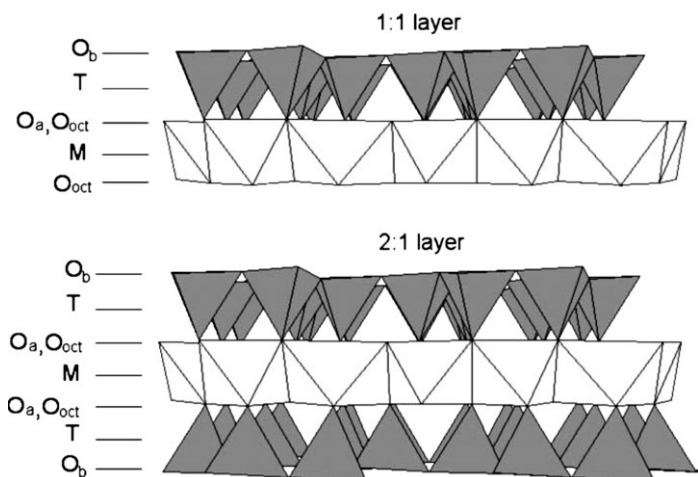


Figure 4-1. 1:1 and 2:1 layer structure of clay minerals [144].

Geophagic clays have been reported to have 1:1 and 2:1 layer arrangements, the literature on their mineralogy include calcite, smectite, illite, kaolinite, halloysite, quartz, feldspar, and montmorillonite [138,139,141,145]. Since clay minerals are abundant in nature and are relatively cheap, there is a wealth of literature on the use of non-edible natural and synthetic clays for the removal of heavy metals in aqueous solutions. Such clays include bentonite, kaolinite, montmorillonite, halloysite, and clay

composites [86,94,154–156,146–153]. So far, no literature has been reported on the use of geophagic clays for the uptake of heavy metals from aqueous solutions.

Since clay minerals are mainly composed of aluminosilicates and quartz, they have the potential as suitable raw materials for synthesis of FAU-type zeolites for water treatment. The application of FAU-type zeolites prepared from clays have been reportedly used as molecular sieves, for the adsorption of gases, as catalysts for industrial processes, and for the uptake of pollutants from contaminated water [4,9,32,35,49,50,53,157,158].

Herein we propose the development of FAU - type zeolites from geophagic clays. The zeolite performance is compared to the untreated clay and that from coal fly ash and a reference FAU – type zeolite. The published work in Appendix 3 (Paper 3) is based on the results from this chapter.

4.2 Materials

The raw clay used for this research was obtained from Nigeria with the necessary DEFRA (Department for Environment, Food and Rural Affairs) certification. The chemicals used for zeolite synthesis and the adsorption experiments are as previously mentioned (Section 2.2).

Instrumental analysis was as previously mentioned in Section 2.2. For the raw clay, additional XRD data for the oriented specimen was collected in the range of 3.5° to 140° where the raw clay sample was mounted by brushing onto a recess of a zero-background silicon sample holder.

4.3 Synthesis

Raw clay samples were first crushed using a planetary ball mill (Retsch PM 100) and sieved to $< 150 \mu\text{m}$ particle sizes for all the experiments. In some experiments, the samples were pre-treated by thermal activation and acid leaching. The clay sample was weighed and mixed with powdered NaOH, at a clay to NaOH mass ratio of 1:1.2 and fused in a furnace at either 600°C or 800°C for

periods of 1 h to 4 h. After NaOH fusion, a mortar was used to grind the fused sample and precise amounts of the ground fused sample were mixed with deionised water in polypropylene reactors at a mass ratio of 1:5, 1:10, and 1:15. The solutions in the polypropylene reactors were aged for 0 to 72 h at ambient temperature while stirring with magnetic stirrers, in some experiments, ageing was done at static conditions (i.e., without stirring). Aged samples were then transferred to a preheated oven to be hydrothermally treated at 90 °C for 0 to 72 h at autogenous pressure. After hydrothermal treatment the samples were filtered, washed to remove excess NaOH, and dried overnight at 90 °C. The dried samples were calcined in a furnace at 550°C for 4 h.

The preparation of the reference FAU zeolite has already been described in Section 2.3.

4.4 Adsorption Studies

A stock solution and standard solutions for a concentration range of 100 to 500 mg L⁻¹ were prepared as previously discussed in Section 2.4.

Batch adsorption experiments for a competitive adsorption system involving quinary metal ions were carried out at 25 °C in triplicates, appropriate amounts of the adsorbents (the raw clay, FAU from clay, and the reference FAU zeolite) were added to aliquots of the standard solutions to test for the effects of the adsorption duration, adsorbent loading, and concentration of the adsorbate. In testing for the optimal adsorption duration, the FAU from clay and the reference FAU zeolite were mixed (at an adsorbent loading of 5 g L⁻¹) with appropriate volumes of the standard solution (initial concentration of 300 mg L⁻¹) in 50 mL polypropylene (PP) sample bottles, the bottles were shaken in a circular motion using a Gerhardt Laboshake for 0 to 180 min. In assessing the effects of adsorbent loading at the optimal duration determined from the previous experiment, standard solutions having initial concentrations of 300 mg L⁻¹ were mixed with the adsorbents and the adsorbent loadings varied from 2.5 to 20 g L⁻¹ for 90 min. The effects of the initial concentration

of the five metals in a competitive adsorption system was tested using an adsorbent loading of 5 g L^{-1} for 90 min at a concentration range of 100 to 500 mg L^{-1} . Adsorption kinetics data was obtained for an initial concentration of 300 mg L^{-1} and duration of 0 to 210 min using an adsorbent loading of 5 g L^{-1} . At the completion of each experiment, each sample was centrifuged for 4 min at 3800 rpm and the supernatant analysed for heavy metal concentration using ICP-OES.

4.5 Results & Discussion

4.5.1 Characterisation of Clay

Figure 4-2(a) shows the SEM image of the uncrushed clay, the size of the raw sample necessitated the need for particle size reduction via crushing and sieving to < 150 μm . The results obtained by XRD and SEM characterisation shown in Figure 4-2(b) shows that the main crystalline phases detected by XRD were predominantly vermiculite, quartz, muscovite, and kaolinite. The SEM shows needle – shaped particles at the surface and irregular shaped densely packed plates beneath them.

Since the XRD patterns of unoriented powder is not a sufficient method for the identification of sheet silicates, XRD patterns were also obtained for oriented powder samples as shown in Figure 4-3. Orientation was achieved by brushing the clay to a zero-background sample holder to introduce the preferred orientation. The difference between the unoriented and oriented XRD patterns was not much, the oriented XRD had a suppression of the

vermiculite peaks and an enhancement of the muscovite peaks, the peaks were sufficient for the identification of the phases present in the clay sample.

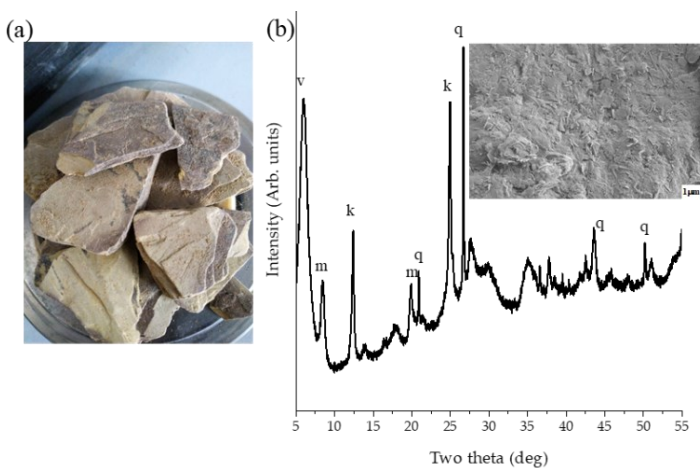


Figure 4-2. Characterisation of raw clay showing (a) image of clay before crushing, (b) XRD pattern of the crushed clay sample, k kaolinite, m muscovite, q quartz, and v vermiculite. The insert is the SEM image.

The XRD data obtained was verified by the location of the characteristic peaks for quartz at $d_{100}(20.8^\circ 2\theta)$,

muscovite at $d_{001}(3.9^\circ 2\theta)$ and $d_{002}(8.35^\circ 2\theta)$, vermiculite at $d_{001}(5.9^\circ 2\theta)$, and kaolinite at $d_{002}(12.3^\circ 2\theta)$. This clay sample is henceforth referred to as a vermiculite kaolinite clay (VK). Vermiculites and muscovites belong with the mica group, they have 2:1 layer arrangement while kaolinites have 1:1 layer arrangement.

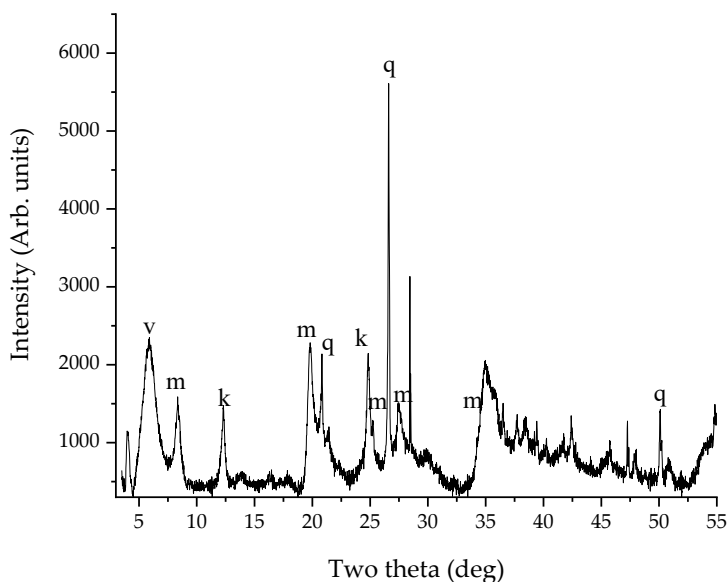


Figure 4-3. XRD pattern of the oriented clay sample oriented raw. k kaolinite, m muscovite, v vermiculite, q quartz.

The textural and compositional analysis of the raw VK gave a BET surface area of $95 \text{ m}^2\text{g}^{-1}$, an external surface area of $74 \text{ m}^2/\text{g}$, a t-plot micropore volume of $0.009 \text{ cm}^3\text{g}^{-1}$, and Si/Al ratio of 2.47. The surface area of clays with mixed compositions such as the VK clay sample has been reported in literature. For instance, kaolinite have been reported with BET surface area of $3.8 \text{ m}^2\text{g}^{-1}$, Ltaief et al. reported a mixed phase of kaolinite and illite with $50 \text{ m}^2\text{g}^{-1}$, and Gu et al. reported $27.8 \text{ m}^2\text{g}^{-1}$ as the surface area of vermiculite [50,147,159]. A comparative study of the surface areas of clays with particle sizes ranging from 0.1 to $50 \mu\text{m}$ was studied by Raman et al. , they reported the range of surface areas for vermiculite as 2.1 to $50.6 \text{ m}^2\text{g}^{-1}$, muscovite 0.9 to $29.5 \text{ m}^2\text{g}^{-1}$, and kaolinite 0.9 to $29.0 \text{ m}^2\text{g}^{-1}$ [160]. The VK clay used for this research has a surface area that is not applicable to a single crystalline phase, the BET specific surface of $95 \text{ m}^2/\text{g}$ for this clay factors in the multi mineral composition of the clay.

The XRF analysis showed that the clay was mainly composed (mass %) of 43.9 % SiO_2 , 15.1 % Al_2O_3 , 5.9 %

Fe₂O₃, 3.2 % MgO, 0.8 % K₂O, and 0.7 % CaO. The reported chemical composition of vermiculite include 39.0 % SiO₂, 12.0 % Al₂O₃, 8.0 % Fe₂O₃, 20.0 % MgO, 4.0 % K₂O, while kaolinite was reported as having 53.7 % SiO₂, 43.6 % Al₂O₃, and 2.0 % Fe₂O₃ [159]. The VK clay was not composed of a singular crystalline phase alone but rather a mixed phase of two different layer type clays and quartz. The crystalline structures were rearranged during zeolite synthesis as discussed in the next section.

4.5.2 FAU - type zeolite: effects of clay pre - treatment

As previously mentioned, the NaOH fusion and hydrothermal treatment synthesis route was applied firstly without pre-treating the VK clay, with pre-treatment via 800 °C thermal activation, and pre-treatment via acid extraction using HCl. The sample to NaOH ratio was 1:1.2 and the sample to deionised water ratio was 1:10, ageing for 68 h and 24 h hydrothermal treatment. The XRD patterns and their corresponding SEM images of the zeolitic materials obtained without

pre-treatment (ZVK – FAU), with thermal activation (ZVK – P), and with acid extraction (ZVK – PQ) are shown in Figure 4-4. ZVK – FAU has the Bragg peaks that characterise NaX (FAU – type) zeolites as seen from location $d_{111}(6.10^\circ 2\theta)$ in Figure 4-4. The thermal activation of the clay produced a pure phase of GIS (ZVK – P), the SEM shows the characteristic woolly morphology of zeolite P with no signs of intergrowth. In addition to the removal of any residual organic matter in the raw clay, thermal activation converted the kaolin component into a chemically reactive metakaolin, activation has been reported for 5 h at 800 °C [161], 1 to 2 h at 600 to 900 °C with the optimal being 1 h at temperature between 750 to 850 °C [161,162]. With the high reactivity of the thermally activated clay, fusion with NaOH and the subsequent ageing and hydrothermal treatment resulted in the dissolution of the crystalline phases and the nucleation and crystallisation of zeolite P (GIS) with particle sizes between 1 to 2 μm . It is interesting to note that with acid extraction at 90 °C, that temperature was

not sufficient for the complete conversion of the kaolinite in the clay to metakaolin hence the formation of a mixed phase of GIS and quartz (ZVK – PQ, Figure 4-4), here the GIS Bragg peaks are of lower intensity compared to the preceding XRD pattern of pure GIS. The SEM of ZVK – PQ shows a marked change in the morphology of the particles, the GIS particles are now smaller than 1 μm and are interspersed by quartz particles (Figure 4-4).

Since a single phase FAU zeolite was obtained without the need for any pre-treatment, subsequent experiments were performed without pre-treatment. The important synthesis parameters tested were the extent of ageing, extent of hydrothermal treatment, alkali fusion temperature, water content, and the effects of precursor agitation.

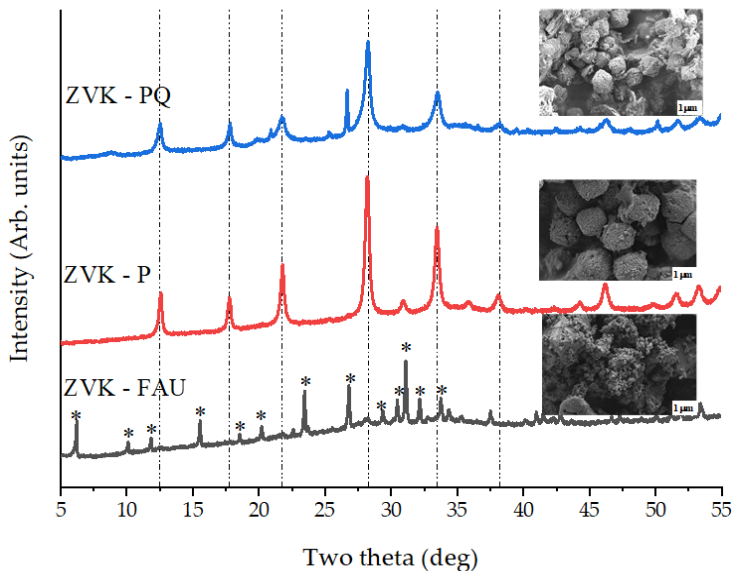


Figure 4-4. XRD patterns and SEM images of a pure NaX phase (ZVK – FAU), a pure GIS (ZVK – P), and a mixed GIS and quartz phases (ZVK – PQ).

4.5.3 FAU - type zeolite: effects of ageing duration

The zeolitic materials obtained from determining the effects of varying precursor ageing at ambient temperature and 1:10 sample to deionised water ratio was carried out for 24 h (ZVK – 24 h), 48 h (ZVK – 48 h), and 68 h (ZVK – 68 h), the XRD patterns are shown in

Figure 4-5. The SEM for 24 h and 48 h ageing are shown in Figure 4-6 while that of 68 h ageing is an insert in Figure 4-4. The three zeolitic materials were obtained after 24 h hydrothermal treatment.

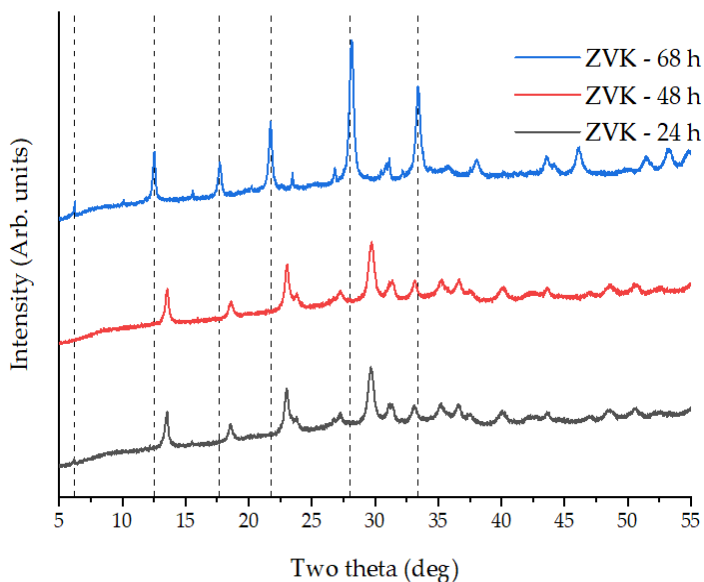


Figure 4-5. XRD patterns of FAU zeolite from VK for 24, 48, and 68 h ageing. Dashed lines represent the main FAU zeolite peaks.

24 and 48 h ageing resulted in predominantly GIS phase and an insignificant smattering of FAU crystals as seen in

Figure 4-5 and Figure 4-6. A crystalline phase change occurs between 48 h ageing and 68 h ageing as evidenced by the XRD patterns and the results of BET surface area analysis. Both the 24 h and 48 h samples had a BET surface area of $61 \text{ m}^2\text{g}^{-1}$. The significant structural change in the crystallinity and the morphology of the 68 h ageing sample (ZVK – 68) resulted in a BET surface area of $219 \text{ m}^2\text{g}^{-1}$. The 68 h ageing duration was similar to that used for the synthesis of FAU zeolites from coal fly ash as discussed in Chapter 2 (Section 2.5.2). Thus 68 h was selected as the optimal synthesis duration.

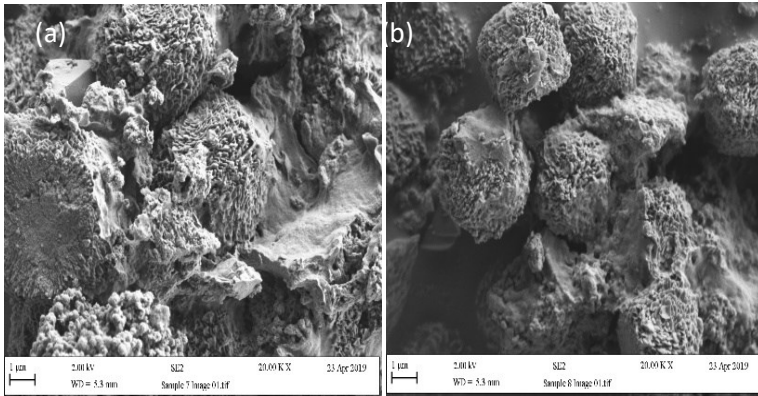


Figure 4-6. SEM images of zeolitic products obtained at (a) 24 h ageing and (b) 48 h ageing.

4.5.4 FAU - type zeolite: effects of hydrothermal treatment

Using an optimal ageing duration of 68 h, the effects of the extent of hydrothermal treatment (HT) on the crystallisation of FAU zeolites was determined by varying the duration from 0 to 72 h at 90 °C and a sample to deionised water ratio of 1:10. The XRD patterns and the SEM images for each product are shown in Figure 4-7 where the products are designated as n HT where n is the

hydrothermal duration (for n = 0, 12, 24, 36, 48, and 72 h).

Product 0 HT bore a close resemblance to the XRD patterns obtained after NaOH fusion with coal fly ash prior hydrothermal treatment shown in Figure 2-7. That is characteristic of the diffraction pattern analysis of the dissolution of crystalline phases before hydrothermal treatment. Thus 0 HT is mainly composed of amorphous phases without any significantly defined crystallinity as shown in the XRD pattern and its SEM image (Figure 4-7). The BET surface area was found to be $52 \text{ m}^2\text{g}^{-1}$, it is less than the surface area of the raw clay which was found to be $95 \text{ m}^2\text{g}^{-1}$. That indicates a significant structural change from the original crystalline structure to the predominantly amorphous particles of 0 HT. 12 h hydrothermal treatment (product 12 HT) led to the formation of FAU zeolites albeit of low intensities, the characteristic FAU shapes are not as well defined yet since there was insufficient extent of heat application for crystallisation. Product 12 HT looks more like an arrested

development of FAU zeolites as seen in Figure 4-7. Without the XRD data, the SEM would have been difficult to confirm FAU morphology. Pairing the XRD pattern for 12 HT ($81 \text{ m}^2\text{g}^{-1}$ surface area) product, the accompanying SEM took on a new meaning, the roughened protrusion of the FAU octahedral shape can now be seen for what it is – an unfinished FAU zeolite structural development. At 24 h hydrotreatment (product 24 HT), the ambiguity of the 12 HT gives way to a clearly defined FAU shape and the BET surface area went from $81 \text{ m}^2\text{g}^{-1}$ to $219 \text{ m}^2\text{g}^{-1}$ signifying a fully developed FAU zeolite structure with particle sizes below $2 \mu\text{m}$ as shown in Figure 4-7. Increasing the hydrothermal treatment duration to 36 h (product 36 HT) gave a FAU product with less structural defects than 24 h but the BET surface area reduced from 219 to $108 \text{ m}^2\text{g}^{-1}$. The reduced surface area was probably because of the larger particle sizes of product 36 HT, the surface area is inversely proportional to the particle size. The 48 h (product 48 HT) and 72 h (product 72 HT) treatments resulted in the shedding of some of the FAU

morphological protrusions to the development of GIS as seen in Figure 4-7. The surface area of $108 \text{ m}^2\text{g}^{-1}$ obtained from the 36 h hydrothermal treatment reduced to 33 and $26 \text{ m}^2/\text{g}$ as the duration was extended to 48 h and 72 h, respectively. Thus between 0 to 72 h hydrothermal treatment, two morphological transition boundaries exist for this clay, at 12 h and at 48 h. The transitions were amorphous to FAU zeolite and FAU to a mixed phase dominated by GIS. Thus 24 h was selected as the optimal hydrothermal treatment extent.

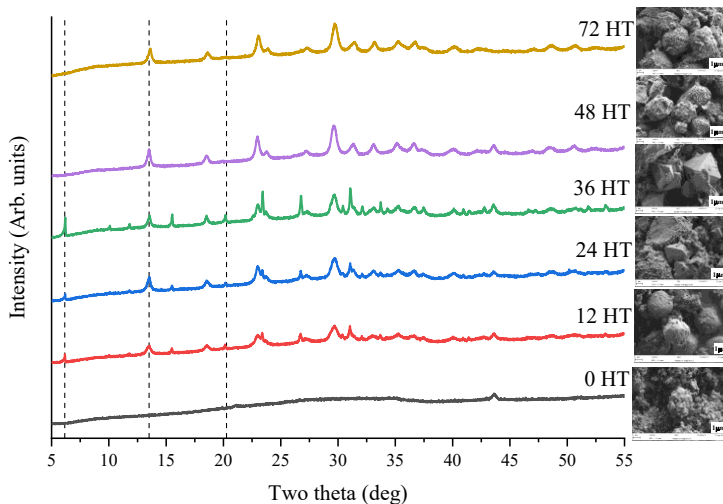


Figure 4-7. XRD patterns of FAU zeolites from VK for hydrothermal treatment (HT) times from 0 h to 72 h. Dashed lines represent the main FAU zeolite peaks. Inserts contain SEM images of the corresponding samples.

4.5.5 FAU - type zeolite: effects of water content and fusion temperature

At optimal ageing and hydrothermal durations of 68 h and 24 h, respectively, the effects of precursor water content and NaOH fusion temperature were determined, and the results presented in Figure 4-8.

Fused sample to deionised water ratios of 1:5, 1:10, and 1:15 was tested followed by hydrothermal treatment at 90 °C for 24 h and the products shown in Figure 4-8(a). The products from 1:5, 1:10, and 1:15 sample to deionised water ratios are designated as 1:5 DI, 1:10 DI, and 1:15 DI, respectively (Figure 4-8a). It was found that a lower water content yielded a FAU zeolite product with superior crystallinity and phase purity, as can be seen from Figure 4-8(a), crystallinity decreased as the water content increased. 1:15 water ratio has the characteristic XRD pattern of pre – hydrothermal FAU zeolite synthesis, it was mainly composed of amorphous phases from the dissolution of crystalline materials after NaOH fusion and ageing. The role of water in the alkali fusion and hydrothermal synthesis of FAU zeolites include silica depolymerisation, post fusion dissolution of crystalline phases, and as polar structure directing agents prior nucleation in zeolite synthesis [163–165]. The hydrothermal treatment of FAU zeolite precursors leads to interspecies interaction of the silicates and water. The

bond strength of such interactions have been reported to be silicate – silicate > silicate – water > water – water, the magnitude of their strength determine how silicates congregate in solutions which in turn dictates the nucleation and crystallisation process [163]. The interactions of the silicate and water species are significantly affected by the latent hydrophilicity and hydrophobicity of the material. This could explain why less amounts of water in the precursor promoted the development of more defined FAU crystalline phases in the samples. The BET surface areas for products 1:5 DI, 1:10 DI, and 1:15 DI were 307, 219 and 57 m²g⁻¹, respectively. Thus, this clay identified an inverse proportion relationship between precursor water content and FAU zeolite crystallinity. In comparison with coal fly ash, the fused sample to water ratio of up to 1:15 was sufficient for the development of well-defined FAU crystals.

Variation of the NaOH fusion conditions shown in Figure 4-8(b) at optimal water ratio (1:5), ageing (68 h), and

hydrothermal treatment (24 h) gave the products denoted as 600 °C 4 h, 600 °C 1 h, and 800 °C 1 h. The products obtained for 4 h fusion at 600 °C and that of 1 h at the same temperature were similar negating the need for an extended fusion duration under high temperature (Figure 4-8b).

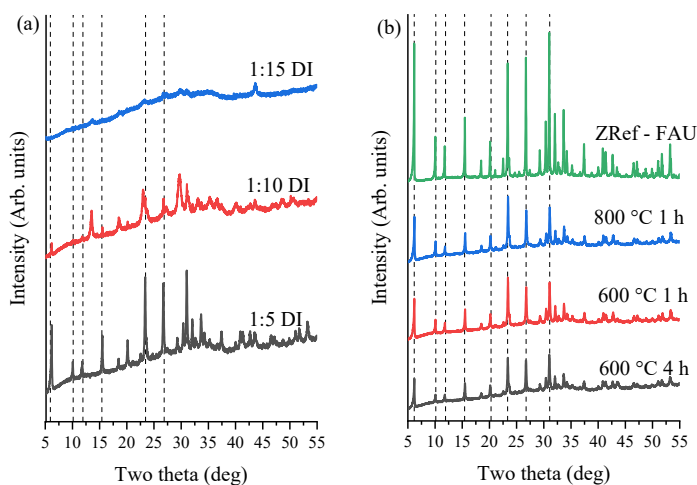


Figure 4-8. XRD patterns FAU zeolites prepared using (a) fused sample to deionised (DI) water mass ratios of 1:5 to 1:15 and (b) different temperatures and times during the alkali fusion step. Dashed lines represent main FAU zeolite peaks.

That of 800 °C for 1 h had higher peak intensities and was chosen as the optimal alkali fusion extent. Thus, a fusion temperature of 800 °C for an hour (BET surface area 303 m²g⁻¹) is sufficient for the subsequent dissolution of the crystalline phases prior to hydrothermal treatment. The FAU peaks obtained agreed with that of the reference material, ZRef – FAU.

4.5.6 FAU - type zeolite: effects of agitation during ageing

Even though the optimal ageing duration was found to be 68 h, that duration translates to a significant drain on energy employed in agitating the sample for 68 h. Thus, a set of experiments were carried to determine the relevance of agitation (to stir or not to stir) to the development of fully formed FAU zeolite crystals. The previously determined optimal experimental parameters were applied here. One of the samples was stirred for 68 h before hydrothermal treatment and the product denoted as ZVK – FAU stirred, another sample was stirred

for 5 min (to ensure adequate mixing) and left without agitation for the rest of the interval followed by hydrothermal treatment (ZVK – FAU static). The XRD patterns of the resulting products are shown in Figure 4-9 including that of the reference FAU zeolite.

It was found that the crystallinity and BET surface area of the static sample was higher than that of the stirred sample. Figure 4-9 shows that the static sample FAU zeolite peaks were of higher intensities than the stirred sample. ZVK – FAU static had a BET surface area was $339 \text{ m}^2\text{g}^{-1}$ which is about 12 % increase in surface area when compared to the stirred sample which had a surface area of $303 \text{ m}^2\text{g}^{-1}$. Thus, the static sample product was chosen as the optimal FAU zeolite prepared from VK clay, henceforth termed ZVK – FAU.

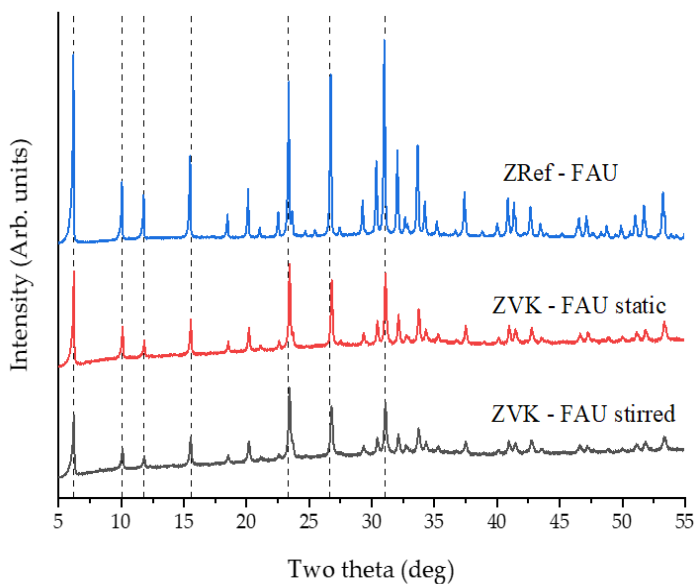


Figure 4-9. XRD patterns of FAU zeolites from VK (ZVK – FAU) under stirred and static ageing. Dashed lines represent main FAU zeolite peaks.

The XRF chemical composition of the optimal zeolite, ZVK – FAU and the reference FAU zeolite is tabulated in Table 4-1. Compared with the optimal zeolite, negligible amounts of Fe_2O_3 , MgO , CaO , and TiO_2 were detected in ZRef – FAU. That is not surprising considering the reference zeolite was prepared from commercially available alumina and silica sources while the clay based

FAU zeolite was prepared from an impure source. Na ions will most likely be the extra framework cations for ZRef – FAU (Si/Al 1.16) while the prepared zeolite, ZVK – FAU (Si/Al 1.61), will have more extra framework cations to contend with. When these zeolites are used as adsorbents in heavy metals removal, the presence of those exchangeable cations can affect the uptake of said metals.

Table 4-1. XRF chemical compositions (mass %) of reference zeolite (ZRef-FAU) and the optimal zeolite from clay (ZVK-FAU).

Adsorbent	SiO ₂	Al ₂ O ₃	Na ₂ O	MgO	Fe ₂ O ₃	TiO ₂	CaO
ZRef-FAU	32.20	23.50	18.90	-	0.03	0.00	0.01
ZVK-FAU	42.80	22.50	19.00	2.69	9.31	1.44	1.13

4.5.7 Simultaneous Removal of Heavy Metals

Prior testing the efficacy of the prepared optimal adsorbent (ZVK – FAU), adsorption experiments were first carried out using raw VK clay as an adsorbent to serve as a basis for comparing the difference in metal uptake resulting from the structural changes from clay to FAU zeolites. The simultaneous uptake of Cd, Co, Cu, Pb, and Zn by the untreated VK from 0 to 180 min at an initial concentration of 200 mg L⁻¹ and from 100 to 500 mg L⁻¹ at 90 min, all at an adsorbent loading of 5 g L⁻¹, is shown in Figure 4-10 while the variation of adsorbent loading from 5 to 15 g L⁻¹ is tabulated in Table 4-2.

The percentage uptake (removal) of the metals were calculated using Equation 20. From Figure 4-10(a), it was determined that 90 min was sufficient for achieving equilibrium concentration in the adsorption process. The decreasing adsorption uptake trend was Pb > Cu > Cd > Co > Zn, similar to the trend for coal fly ash FAU (CFZ10 – 68), peat sample A LTA, sample B LTA, and sample B FAU. At 200 mg L⁻¹, the most adsorbed metal, Pb, had about 20

% difference with the next most adsorbed, Cu as shown in Figure 4-10 (a-b). That is an indication of a discriminate preference of Pb ions over the other four ions.

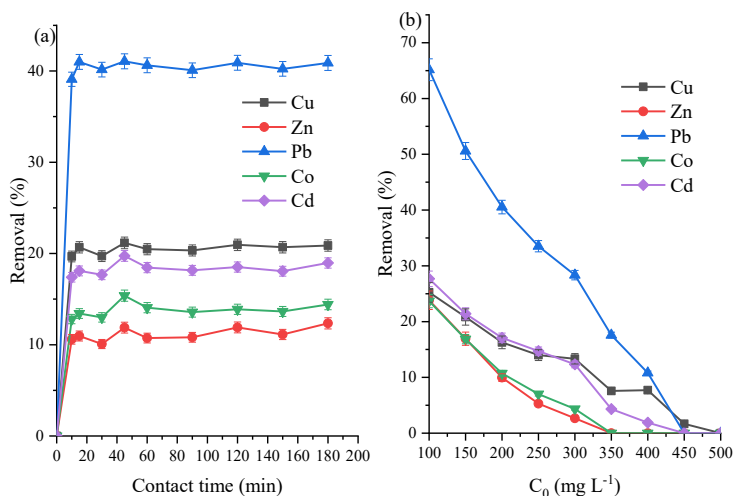


Figure 4-10. Untreated VK metal uptake at $5 \text{ g} \cdot \text{L}^{-1}$ adsorbent loading for (a) $C_0 = 200 \text{ mg L}^{-1}$ for 10 to 180 min and (b) $C_0 = 100$ to 500 mg L^{-1} at 90 min.

At the lowest concentration, 100 mg L^{-1} , about 65 % of Pb was removed from the solution while Cu, Cd, Zn, and Co

had 25 %, 28 %, 24%, and 24 %, respectively. At lower concentration, Cd was slightly preferred over Cu and as the adsorbent–adsorbate boundary becomes overcrowded with higher concentrations of the adsorbates, the adsorption process stalls and proceeds with a sharp decline as seen in Figure 4-10(b). At 200 mg L⁻¹, doubling and tripling the adsorbent loading from 5 to 10 and 15 g L⁻¹ resulted in an increased uptake of the metal ions by the clay. Generally, an increase in the amount of adsorbent is proportional to an increase in the available adsorption sites. The chemical and textural makeup of the raw clay did not permit an appreciable uptake of the metals with initial concentrations above 300 mg L⁻¹.

Table 4-2. Untreated VK clay loading variation ($C_0 = 200 \text{ mg L}^{-1}$ at 90 min) on the uptake (%) of divalent metals.

VK load (g L^{-1})	Cu (%)	Zn (%)	Pb (%)	Co (%)	Cd (%)
5.0	16.3	10.0	40.5	10.7	17.1
10.0	30.9	18.1	61.2	20.2	23.9
15.0	43.6	28.2	75.9	29.6	32.4

Figure 4-11 shows the adsorption efficiency plots for the prepared FAU zeolite, ZVK – FAU. Compared to the raw VK which became overwhelmed even as little as 150 mg L^{-1} initial concentration, the superior FAU zeolite resulted in an increased simultaneous uptake of the metals at the minimal adsorbent loading of 5 g L^{-1} .

It was also found that the optimal adsorption duration was 90 min beyond which there was no substantial adsorption to warrant an extended time as shown in Figure 4-11(a). The experiment for 100 to 500 mg L^{-1} shown in Figure 4-11(b) indicates a total removal of Pb

for all the concentration range while the other four metals had a steady decline as the concentration was increased. The decreasing order of the selectivity trend was found to be $Pb > Cu > Cd > Zn > Co$ like that of FAU from coal and peat ash samples.

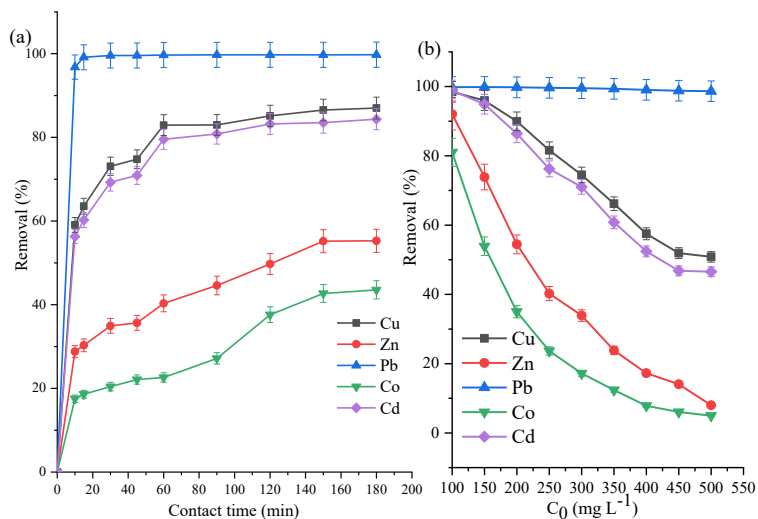


Figure 4-11. ZVK – FAU simultaneous uptake of five metals at (a) 300 mg L^{-1} from 0 to 180 min and (b) 90 min for $C_0 = 100$ to 500 mg L^{-1} and 5 g L^{-1} zeolite loading.

In assessing the effects of reducing and increasing the loading variation would have on the adsorption system, ZVK – FAU was varied from 2.5 to 20 g L⁻¹ as shown in Table 4-3. At the lowest adsorbent loading, the uptake of Pb was 98.1 %, indicating the highest selectivity of Pb by the uptake of disproportionate amount of Pb in comparison to the other four metals in the aqueous solution (Table 4-3). This implies that no matter how few the adsorption available sites, if Pb is in the mix with Cu, Cd, Co, and Zn, the adsorbent would discriminate others and permit the occupation of the adsorption sites by Pb ions. As the adsorbent loadings are increased, the uptake of the other metals also increased with preference given to the selectivity trend. Thus, the increased uptake of Cu over Cd at 5 g L⁻¹, and by 10 g L⁻¹, the selectivity of Cu and Cd was no longer an issue since that loading ensured that there are adsorption sites that would suffice the easy uptake of Cu and Cd. The least adsorbed metals, Zn and Co required 15 and 20 g L⁻¹, respectively for almost 100 % removal from the aqueous solution.

Table 4-3. ZVK - FAU loading variation ($C_0 = 300 \text{ mg L}^{-1}$ at 90 min) on the percentage uptake (%) of divalent metals.

ZVK - FAU load (g L^{-1})	Cu (%)	Zn (%)	Pb (%)	Co (%)	Cd (%)
2.5	37.7	12.5	98.1	6.7	35.7
5.0	74.5	33.9	99.5	20.4	71.0
10.0	97.3	79.7	99.9	59.6	97.2
15.0	99.4	97.0	99.9	90.5	99.7
20.0	99.7	99.4	100.0	97.8	99.9

4.5.8 Adsorption kinetics

The adsorption kinetics data for ZVK - FAU at an initial concentration of 300 mg L^{-1} , an adsorbent loading of 5 g L^{-1} , and time 0 to 210 min (Section 4.4) was modelled using the linear forms of the first-order, second – order, pseudo second – order, and intraparticle diffusion models. The kinetics parameters are tabulated in

Table 4-4. Generally, the pseudo second – order model had the best fit for most of the metals in a competitive adsorption system. Using this model, the correlation coefficient (R^2) values was found to be 1.0 for Pb, Cu and Cd, 0.92 for Zn, and 0.71 for Co (

Table 4-4). In comparing the experimental amount of metal adsorbed at equilibrium, q_e , to that obtained from the pseudo second – order (PSO) model fitting, there was a close agreement for the metals. At initial adsorbate concentration of 300 mg L^{-1} , Pb had an experimental of q_e value of 59.9 mg g^{-1} while the PSO model also gave 59.9 mg g^{-1} which confirms the validity of that model for Pb. For the least adsorbed metal, Co, the experimental q_e was 41.9 mg g^{-1} while the PSO model also gave 42.0 mg g^{-1} which were equal even though the PSO model correlation was low compared to that of the first order ($R^2 = 0.79$).

The first – order kinetics equation, where the rate of adsorption depends only on the concentration of one component, cannot adequately describe a competitive adsorption system such as what was done here. Thus, the PSO model was chosen as the best empirical relation for all the metals establishing the mechanism of chemisorption for the adsorption process. According to the magnitude of the PSO rate constant, k_{PSO} , how fast the adsorption occurs should follow the decreasing trend $Pb > Cu > Cd > Zn > Co$.

The intraparticle diffusion model fitting for the metals had R^2 between 0.81 and 0.9, it indicates the possibility of diffusion within the pores of ZVK – FAU adsorbent.

Table 4-4. Kinetics parameters for ZVK - FAU.

		Cu	Zn	Pb	Co
First-order	k_1 (min ⁻¹)	0.006	0.004	0.008	0.004
	R ²	0.873	0.863	0.521	0.792
Second-order	k_2 (L.mg ⁻¹ .min ⁻¹)	-	-	0.006	-
	R ²	0.942	0.740	0.798	0.668
Pseudo second-order	q_e (mg. g ⁻¹)	54.945	43.290	59.880	42.017
	k_{PSO} (g. mg ⁻¹ .min ⁻¹)	0.002	0.001	0.112	-
	R ²	0.999	0.920	1.000	0.714
Intraparticle diffusion	k_{ID} (mg. min ^{0.5} .g ⁻¹)	1.479	2.025	0.014	2.223
	R ²	0.876	0.903	0.867	0.806

4.5.9 Adsorption isotherms

The use of nonlinear adsorption isotherms over their linearised forms helps in minimising the error variance that results from linearisation. The experimental adsorption data for ZVK – FAU and the reference zeolite, ZRef – FAU were fitted using the solver function in MS Excel to obtain the isotherm parameters in Table 4-5 and Table 4-6, respectively. Pb, Cu, and Cd data were modelled using Freundlich, Fritz-Schlunder IV, Langmuir, Redlich-Peterson, and Tóth isotherms while Zn and Co were modelled using only Fritz-Schlunder IV and Redlich-Peterson isotherms due to their dismal fit with the others. A value as close to unity for the coefficient of correlation, R^2 , was the criterion for selecting the best model for each metal.

Starting with the most adsorbed metal, Pb, the experimental value obtained at the maximum adsorption, q_{\max} ($q_{\max, \text{exp}}$), using ZVK – FAU was 98.6 mg g^{-1} while that of ZRef – FAU was 99.7 mg g^{-1} . The q_{\max} values for Pb obtained from modelling the adsorption

data using nonlinear Langmuir isotherm was 100.2 mg g^{-1} ($R^2 = 0.96$) for ZVG – FAU and 111.1 mg g^{-1} ($R^2 = 0.98$) for ZRef – FAU as shown in Figure 4-12, Table 4-5, and Table 4-6. Those values were close enough to the experimental value therefore, the Langmuir isotherm is valid for Pb for either adsorbents. The modelling of the data using the nonlinear Freundlich for both adsorbents also proved valid for Pb in both cases with the R^2 values closer to unity than with the Langmuir isotherm (Figure 4-12, Table 4-5, and Table 4-6).

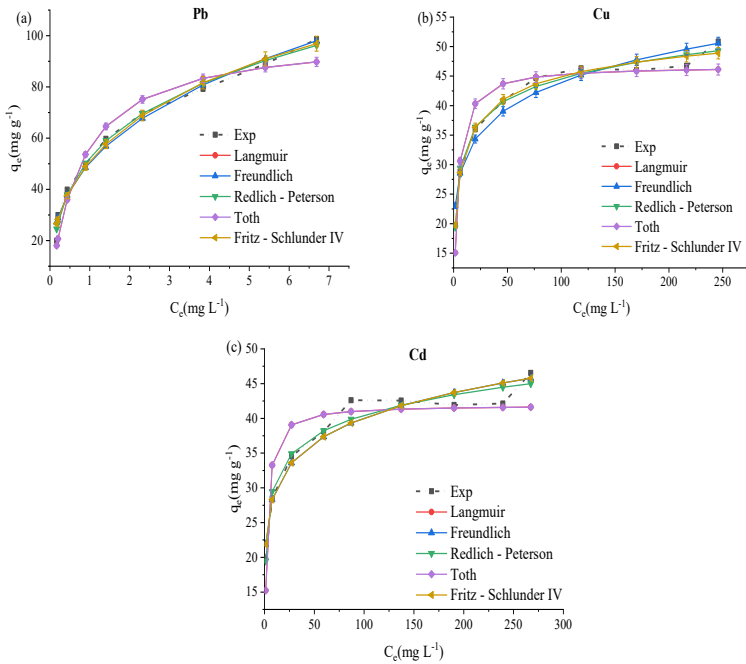


Figure 4-12. ZVK – FAU nonlinear adsorption isotherms plots for the simultaneous removal of five metals at 90 min, $C_0 = 100$ to 500 mg L^{-1} and 5 g L^{-1} zeolite loading for (a) Pb, (b) Cu, and (c) Cd.

The validity of both Langmuir and Freundlich isotherms imply that the adsorption process included both monolayer and multilayer adsorption over heterogeneous surfaces. Model fitting using Redlich-Peterson, Tóth, and

Fritz-Schlunder IV for Pb using both adsorbents showed that both ZVK – FAU and ZRef – FAU had the highest R^2 value of 0.99 with Redlich-Peterson. That is not surprising since the Redlich-Peterson model is a combination of the Langmuir and the Freundlich models, it is usually applicable to adsorption processes that are inclusive of mono and multi layers. It reaffirms the validity of either Langmuir or Freundlich model for the adsorption of Pb on the FAU – type adsorbents.

The $q_{\max, \text{exp}}$ for Cu was 50.8 mg g⁻¹ using ZVK – FAU and 61.4 mg g⁻¹ using ZRef – FAU. The Langmuir model gave a q_{\max} of 46.7 mg g⁻¹ ($R^2=0.92$) using ZVK – FAU while ZRef – FAU was found to be 46.9 mg g⁻¹ ($R^2=0.90$). The Freundlich model on the other hand gave R^2 of 0.96 and 0.99 for ZVK – FAU and ZRef – FAU, respectively (Figure 4-12, Table 4-5, and Table 4-6). The better fitting of the data to the Freundlich model over the Langmuir model implies multilayer adsorption dominates the process. Model fitting using the Redlich-Peterson relation gave R^2 of 0.99 for both ZVK – FAU and ZRef – FAU. Without fitting

the data using both Langmuir and Freundlich, fitting with only the Redlich-Peterson equation would have given rise to ambiguity regarding the dominant layer adsorption system in place. Knowing the Cu data was better fitted with the Freundlich isotherm over the Langmuir isotherm, the Redlich-Peterson isotherm confirms the multilayer adsorption process. The R^2 for Tóth and Fritz-Schlunder IV was 0.91 and 0.99, respectively for ZVK – FAU. On the other hand, the R^2 for Tóth and Fritz-Schlunder IV was 0.82 and 0.95, respectively for ZRef – FAU.

The $q_{\max, \text{exp}}$ for Cd was 46.5 mg g⁻¹ using ZVK – FAU and 77.0 mg g⁻¹ using ZRef – FAU. The Langmuir model gave a q_{\max} of 41.9 mg g⁻¹ ($R^2=0.84$) using ZVK – FAU while ZRef – FAU was found to be 52.1 mg g⁻¹ ($R^2=0.94$). The Freundlich model on the other hand gave R^2 of 0.95 and 0.99 for ZVK – FAU while ZRef – FAU, respectively (Figure 4-12, Table 4-5, and Table 4-6). The Freundlich isotherm had a better fitting for both adsorbents and a fitting using the Redlich-Peterson model gave R^2 of 0.97 and 0.99 for

ZVK – FAU while ZRef – FAU, respectively. The R^2 for Tóth and Fritz-Schlunder IV was 0.83 and 0.95, respectively for ZVK – FAU. On the other hand, the R^2 for Tóth and Fritz-Schlunder IV was 0.99 and 0.97, respectively for ZRef – FAU.

For the least adsorbed metals, Zn and Co, the $q_{\max, \text{exp}}$ was 37.7 and 29.4 mg g^{-1} , respectively using ZRef – FAU. The Langmuir and Freundlich models gave the values of 34.8 mg g^{-1} ($R^2=0.89$) and 27.1 mg g^{-1} ($R^2=0.99$), respectively for ZRef – FAU. For ZVK – FAU, the $q_{\max, \text{exp}}$ was 22.2 and 16.2 mg g^{-1} , for Zn and Co, respectively. Although the Langmuir, the Freundlich, and the Tóth isotherms could not be used in fitting the adsorption data of Zn and Co for ZVK – FAU, the Redlich-Peterson and the Fritz-Schlunder IV showed reasonably good fittings. For ZVK – FAU, the decreasing model fitting trend for both Zn and Co was Fritz-Schlunder IV > Redlich-Peterson as shown in Figure 4-13 and Table 4-5.

Table 4-5. ZVK - FAU nonlinear adsorption isotherm parameters ($C_0 = 100$ to 500 mg L^{-1} at 90 min and 5 g L^{-1} adsorbent loading).

Model	Parameter	Pb	Cu	Cd	Zn	Co
Langmuir	$q_{\max} (\text{mg g}^{-1})$	100.153	46.712	41.924	-	-
	$K_L (\text{L mg}^{-1})$	1.292	0.314	0.502	-	-
	R^2	0.957	0.915	0.836	-	-
Freundlich	$1/n$	0.349	0.154	0.135	-	-
	K_F	50.521	21.615	21.515	-	-
	R^2	0.986	0.956	0.948	-	-
Redlich-Peterson	K_{RP}	425.625	37.795	72.577	3.281	1.216
	a_{RP}	7.127	1.349	2.884	0.029	0.003
	b_{RP}	0.731	0.896	0.896	1.356	1.659
Tóth	R^2	0.992	0.986	0.967	0.736	0.946
	K_T	6.734	4.599	15.123	-	-
	α_T	0.774	3.182	1.993	-	-
	t	14.872	10.157	2.772	-	-
Fritz-Schlunder	R^2	0.953	0.907	0.829	-	-
	β_1	0.3687	0.5122	0.1351	0.0005	0.0001
	β_2	1.4019	0.4816	0.0001	1.9657	1.8211
IV	α_1	51.2060	27.5655	21.5237	20.1108	16.8901
	α_2	0.0046	0.5964	0.0004	0.0000	0.0000
	R^2	0.9877	0.9878	0.9484	0.8110	0.9907

For ZRef – FAU, the trend for Zn was Redlich-Peterson > Langmuir > Fritz-Schlunder IV > Freundlich > Tóth while

Co was Langmuir > Fritz-Schlunder IV > Redlich-Peterson
 > Freundlich > Tóth as shown in Table 4-6.

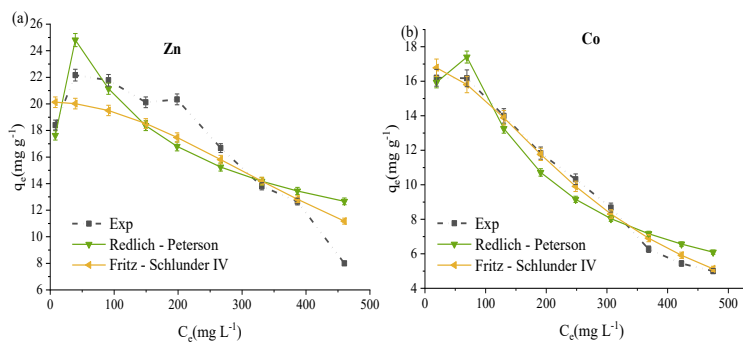


Figure 4-13. ZVK – FAU nonlinear adsorption isotherms plots for the simultaneous removal of five metals at 90 min, $C_0 = 100$ to 500 mg L⁻¹ and 5 g L⁻¹ zeolite loading for (a) Zn and (b) Co.

Table 4-6. ZRef - FAU nonlinear adsorption isotherm parameters (C_0 = 100 to 500 mg L⁻¹ at 90 min and 5 g L⁻¹ adsorbent loading).

Model	Parameters	Pb	Cu	Cd	Zn	Co
Langmuir	q_{max} (mg g ⁻¹)	111.081	46.874	52.105	34.820	27.098
	K_L (L mg ⁻¹)	3.835	1.991	6.353	3.988	3.761
	R^2	0.977	0.904	0.941	0.891	0.988
Freundlich	$1/n$	0.617	0.180	0.198	0.088	0.031
	K_F	128.232	26.921	37.056	24.687	23.048
	R^2	0.992	0.991	0.993	0.849	0.336
Redlich-Peterson	K_{RP}	4228.923	738.597	1587.369	206.628	53.863
	a_{RP}	32.316	25.990	40.492	6.878	1.464
Tóth	b_{RP}	0.406	0.837	0.831	0.960	1.073
	R^2	0.988	0.992	0.995	0.937	0.778
	K_T	1.151	5.303	18.625	3.911	4.891
Fritz-Schlunder	α_T	0.268	0.769	47.504	0.211	0.140
	t	96.680	9.875	0.881	8.454	4.937
	R^2	0.973	0.817	0.985	0.772	0.114
IV	β_1	0.778	0.539	0.175	0.088	0.214
	β_2	0.692	0.468	0.384	1.883	0.674
IV	α_1	291.082	91.213	37.403	24.695	21.775
	α_2	2.337	2.247	0.026	0.000	0.052
	R^2	0.980	0.954	0.971	0.851	0.914

4.6 Conclusions

In this research, geophagic clay was characterised and, for the first time, used to prepare faujasite zeolites via alkali fusion and hydrothermal crystallisation. The clay layer type was found to 1:1 and 2:1, the mineral composition was vermiculite, kaolinite, muscovite, and quartz. The clay was used to prepare FAU – type (NaX) zeolites by varying synthesis conditions. The optimal FAU – type synthesis conditions were found to be NaOH fusion with the raw clay at 800 °C for 1 h, a mass ratio of the fused sample to deionised water ratio of 1:5, 68 h of static ageing of the suspension (including an initial 5 min of mixing), and 24 h of hydrothermal treatment at 90 °C.

The efficacy of the synthesised optimal FAU – type zeolite was tested for a competitive simultaneous adsorption system comprising of Cd, Co, Cu, Pb, and Zn. The result was compared with the raw clay and a reference FAU – type zeolite material. It was found that at an initial concentration of 300 mg L⁻¹ and an adsorbent loading of 5 g L⁻¹, within the first 10 min, almost 100 % of Pb was

removed while 60 % of Cu, 58 % of Cd, 28 % of Zn, and 19 % of Co were removed from the aqueous solution. At an optimal adsorption duration of 90 min, the divalent cation selectivity trend was $Pb > Cu > Cd > Zn > Co$. Two to four parameter nonlinear adsorption isotherms were used to fit the adsorption data and it was found that overall, three and four parameter isotherms had the best fit for the adsorption process. Overall, the adsorption process for FAU - type zeolite from VK clay was best described by the nonlinear empirical models of the Redlich - Peterson isotherms for Pb, Cu, and Cd while the Fritz – Schlunder IV isotherm was used to describe the adsorption of Zn and Co. On the other hand, the Redlich – Peterson isotherm best described the adsorption using the reference FAU - type zeolite.

The highlights of this research include:

- i. Geophagic clay was successfully converted to FAU-type zeolite.
- ii. Synthesis parameters for the conversion were systematically optimised.

- iii. FAU zeolite from geophagic clay improved the adsorption capacity of five divalent metals.

5 SOLVENT-FREE ZEOLITE SYNTHESIS

5.1 Literature Review

Cancrinites belong with the feldspathoids (tectosilicates) class of minerals but due to their interlinked and porous aluminosilicate framework, they are also classified as zeolites [166,167]. Cancrinite zeolites are characterised by open cavities consisting of two channel types; narrow ϵ cages and wider β cages [48,168–171]. The crystal system is hexagonal pyramidal with a Hermann-Mauguin (H-M) symbol of 6, and $P6_3/mmc$ space group. The cancrinite zeolite framework has the three-letter designation of CAN with a sphere diameter of about 6.27 Å. The stacking of its six membered rings follows an ABAB.. sequence that results in 1D large channels confined by alternating SiO_4 and AlO_4 tetrahedra twelve membered rings as shown on Figure 5-1 [171–173]. These zeolites have applications in the fields of water purification, nuclear waste treatment, and catalysis [48,52,174].

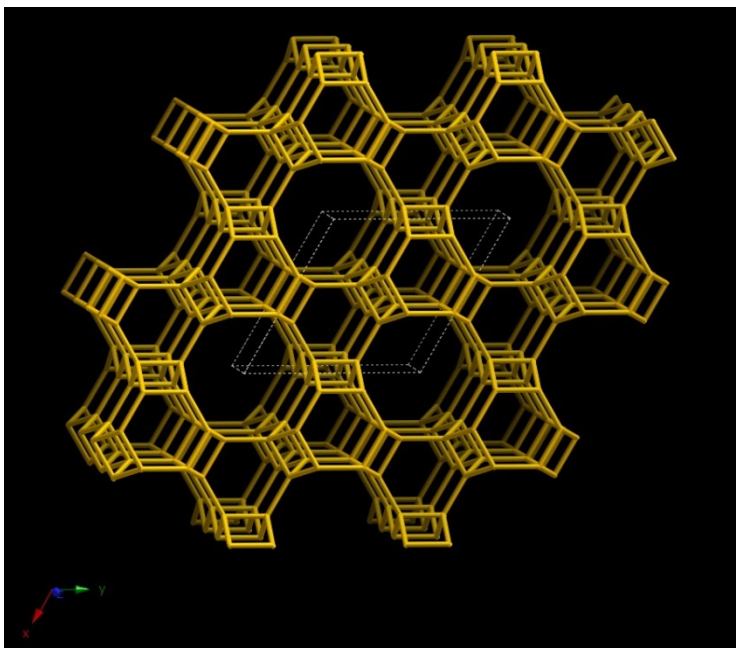


Figure 5-1. CAN zeolite viewed along 001 [175].

Since the inception of synthetic zeolite synthesis, the conventional technique has been the hydrothermal route wherein water, as a solvent, plays vital roles in the depolymerisation and condensation of silica species [164,176,177]. The drawbacks of using solvents include material wastes, toxic pollutants, lower zeolite yields, and increased autogenous pressures [164,177,178].

Advances in green chemistry has prompted research in solvent – free synthesis of zeolites that would result in higher yields at autogenous pressure.

Unlike FAU - type and LTA zeolites, reported findings on the syntheses of CAN zeolites is sparse despite its economic importance. The dearth of published research data is probably due to the co-crystallisation of unwanted phases during the nucleation and crystal growth stages of CAN synthesis, thus a pure CAN zeolite product is a rarity [179,180].

The starting materials for the synthesis of cancrinite zeolite via hydrothermal or solvent-free routes include commercially sourced alumina/silica, metakaolin, an alkaline environment, and in some instances the modification of fully developed zeolites like the FAU – type zeolite [174,179,181]. The use of kaolinite, bentonite, muscovite, and even agricultural wastes like rice husk ash have been reported for the synthesis of CAN zeolite albeit with other crystalline phases co – crystallising with the CAN product

[48,52,166,167,170,182]. The few literature on the synthesis method was mainly hydrothermal synthesis, in some instances, alkali pre-fusion step was carried out before hydrothermal treatment. The synthesis was thusly done at temperature between 120 to 650 °C for durations from 24 h to 21 days and at pressures as high as 100 MPa [52,179]. The products were mainly CAN mixed with other phases like sodalite and even quartz [52,179]. In contrast, solvent – free routes at autogenous pressures are reported to be optimal at 100 °C over 72 h and 100 °C over 48 h [170,174]. In addition to the synthesis duration, the formation of unwanted phases and the pre-treatment of precursors provide areas of investigation for the synthesis of CAN zeolites.

In the previous chapter, the vermiculite kaolinite (VK) was used to prepare zeolites via the alkali pre – fusion and hydrothermal route. GIS and FAU – type zeolites were successfully synthesised from that clay. In this chapter the experimental conditions were changed to synthesise CAN zeolite using the same clay. Herein, the

synthesis of CAN zeolite is reported using a one - step solvent – free synthesis route with no structure-directing agent. The product obtained was a pure CAN zeolite crystalline phase without the formation of unwanted phases, a scale up yielded a consistent CAN zeolite product.

5.2 Materials

In addition to the materials mentioned in Section 4.2 and the chemicals in Section 2.2, 99.99% purity analytical grades of sodium carbonate, sodium carbonate decahydrate, and aluminium sulphate octadecahydrate were also purchased from Sigma Aldrich.

Instrumental analysis was as previously mentioned in Section 2.2. In addition, the crystallite sizes of the samples were calculated in HighScore Plus by line profile analysis of the cancrinite d_{211} peak using a Pseudo-Voight peak function. High resolution transmission electron

microscopy (HRTEM) images were carried out on an Oxford JEOL 3000F field emission TEM.

5.3 Synthesis

The raw VK clays were first crushed using a planetary ball mill and sieved to particle sizes $<150\ \mu\text{m}$. Without pre-treatment by either thermal activation or acid leaching, predetermined amounts of the clay, NaOH, and $\text{Al}_2(\text{SO}_4)_3 \cdot 18\text{H}_2\text{O}$ (1.00:1.20:1.45 ratios, respectively) were manually mixed in a mortar, placed in Teflon-lined autoclaves, and heated at $180\ ^\circ\text{C}$ for 0.5 – 72 h, and between $80\text{ – }180\ ^\circ\text{C}$ for 6 h. Some experimental trials were carried using clay mixed with NaOH (1:1.2), Na_2CO_3 (1:1.2), $\text{Na}_2\text{CO}_3 \cdot 10\text{H}_2\text{O}$ (1:1.2), and a combination of $\text{Na}_2\text{CO}_3 \cdot 10\text{H}_2\text{O}$ and NaAlO_2 (1:1.2:0.13) at $180\ ^\circ\text{C}$ for 24h. After heating for the desired duration, the autoclave was quenched, and the sample washed with deionised water. Product recovery was via centrifugation at

3800 rpm for 5 min. The samples were then dried in an oven and calcined in a furnace at 550 °C for 1 h.

5.4 Adsorption Studies

A stock solution and standard solutions for a concentration range of 100 to 500 mg/L were prepared as previously discussed in Section 2.4. The experimental method was optimised using a two level, three factor, full factorial experimental design from Minitab 20 statistical software, that was to avoid the tedious process of varying a wide range of parameters that affect adsorption [183,184]. In adsorption experiments, even though it is logical that an increased amount of adsorbents would lead to an increase in adsorption, a factorial experimental design would help in determining the effects of the interaction of different parameters that affect the adsorption process. These interactions could produce an antagonistic, synergistic or a ceiling effect where the higher the amount of an independent variable reduces the effect of another variable. In comparison to the usual

one factor at a time (OFAT) experimental method, the factorial design is more efficient and produces a more comprehensive overview of the effects of the main parameters that affect adsorption. Using the three factor (concentration, time, and adsorbent loading) two level (high and low) factorial design, aqueous solutions were prepared in duplicates with the variation of adsorbent loading (5 to 10 g/L), concentration (200 to 400 mg/L), and time (60 to 120 min) to find the optimal experimental conditions for the uptake of the five heavy metals. The choice of the high and low values was based on an approximation of how low or high the values would have to be to give a quantifiable estimation of the effects of the three adsorption parameters. The experiments were randomised in replicates to minimise errors.

For the adsorption experiments at 25 °C, appropriate amounts of the adsorbent (ZVK - FAU) was added to aliquots of the standard solutions to test for the effects of the adsorption duration, adsorbent loading, and concentration of the adsorbate as designed using the

Minitab 20 software. In other experiments at a concentration range of 50 to 400 mg/L, ZVK - FAU was mixed (at an adsorbent loading of 10 g/L) with appropriate volumes of the standard solutions in 50 mL polypropylene (PP) sample bottles, the bottles were shaken in a circular motion using a Gerhardt Laboshake for 90 min. At the completion of the adsorption experiment, the solutions were centrifuged for 4 min at 3800 rpm and the supernatant analysed for heavy metal concentration using ICP-OES.

5.5 Results & Discussion

5.5.1 Effects of NaOH

The results from the characterisation of the VK clay have been described in Chapter 5 (4.5.1). The solvent – free synthesis was carried out for different combination of the clay with NaOH, $\text{Al}_2(\text{SO}_4)_3 \cdot 18\text{H}_2\text{O}$, Na_2CO_3 , $\text{Na}_2\text{CO}_3 \cdot 10\text{H}_2\text{O}$, and NaAlO_2 .

Figure 5-2 shows the XRD patterns for 72 h solvent – free synthesis using a mixture of clay with NaOH at 180 °C and a mixture of clay with $\text{Al}_2(\text{SO}_4)_3 \cdot 18\text{H}_2\text{O}$ only without the addition of NaOH for 80 °C and 180 °C. At 80 °C, quartz was the predominant crystalline phase albeit with poor crystallinity as well as amorphous phases as evidenced by the broad peaks in Figure 5-2 (a). The increase in synthesis temperature from 80 to 180 °C resulted in the substantial reduction of the amorphous phases and instead the highly crystalline alunite (aluminium potassium sulphate mineral) and some quartz Bragg peaks were observed. The alunite phase was due to the solfataric (escape of sulphur gas stream) action from the interactions of feldspathoids with sulphate compounds. The characteristic peak with the maximum intensity ($I_{\text{rel}} 100$) for quartz is located at $26.65^\circ 2\theta$ (d_{101}) and is easily identified in the XRD patterns of Figure 5-2 (a). Synthesis with only clay and NaOH yielded a mixture of amorphous and crystalline phases, the crystalline phase was identified as hydroxy sodalite (Figure 5-2b).

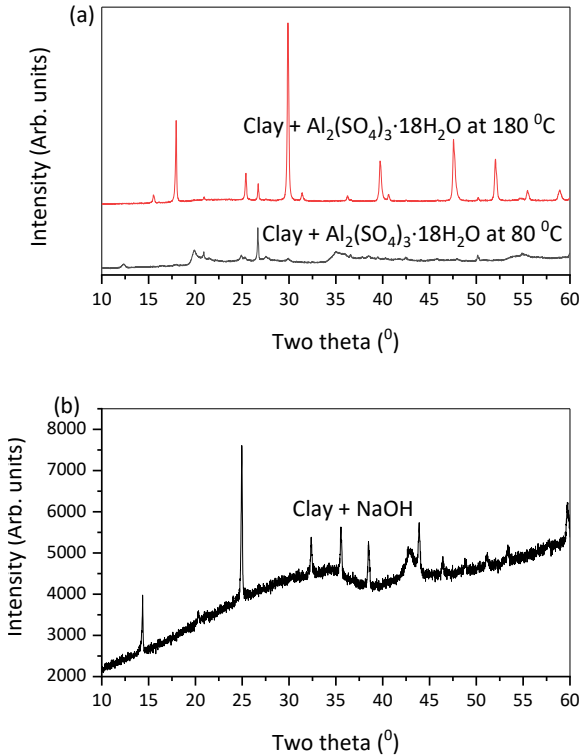


Figure 5-2. XRD patterns of synthesis (a) without NaOH at 80 °C and 180 °C, (b) with only clay and NaOH at 180 °C.

After observing the standalone effects of NaOH and $\text{Al}_2(\text{SO}_4)_3 \cdot 18\text{H}_2\text{O}$ when mixed with clay and autoclaved, Figure 5-3 shows the experimental trials for the mixture

of clay, NaOH and $\text{Al}_2(\text{SO}_4)_3 \cdot 18\text{H}_2\text{O}$ at 180 °C for 72 h. The XRD patterns for clay to NaOH ratios of 1:1.2, 1:0.8, 1:0.4, and no NaOH addition are shown in Figure 5-3. After synthesis, the precursor with the maximum amount of NaOH (1:1.2) resulted in CAN zeolites (Figure 5-3, major cancrinite peaks labelled c) as the only crystalline phase present in the sample; the Bragg peaks matched the cancrinite peaks reported by Treacy et.al [19]. CAN zeolite characteristic peaks with high intensities, a representation of the crystallinity, are located at $19.15^\circ 2\theta$ (d_{101}) and $27.74^\circ 2\theta$ (d_{211}) [19]. It was observed that progressively reducing the amount of NaOH first led to a mixed CAN zeolite and alunite mineral phases and as NaOH was completely excluded, a single alunite crystalline phase emerged (peaks labelled a in Figure 5-3).

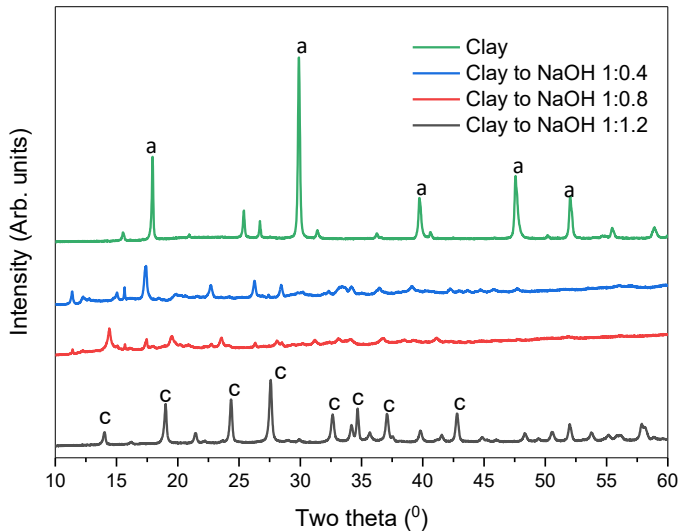


Figure 5-3. XRD patterns for the variation of NaOH to clay ratios. c CAN and a alunite.

5.5.2 Time- and temperature- evolution

CAN zeolite crystallinity evolution in Figure 5-3 resulting from the addition of NaOH supports the theory that the presence of an alkaline environment is a necessity for the dissolution of the original aluminosilicate crystalline phases prior to zeolite nucleation [185]. Hence a pure CAN zeolite product was obtained when the maximum amount of NaOH was added indicating a direct

proportional relationship between the amounts of NaOH added and CAN phase purity. This implies that a sample devoid of NaOH would likely result in the complete absence of CAN zeolite as proved in Figure 5-2(a). Therefore, a clay to NaOH ratio of 1:1.2 was selected as the best option.

Experiments where clay, NaOH, and $\text{Al}_2(\text{SO}_4)_3 \cdot 18\text{H}_2\text{O}$ were used to investigate the effects of time and temperature – evolution are shown Figure 5-4 and Figure 5-5. The XRD diffraction peak intensities at d_{101} corresponding to CAN zeolites prepared for 0.5 to 72 h at 180 °C (Figure 5-4) and 80 to 180 °C for 6 h (Figure 5-5) were plotted. From Figure 5-4, even at the lowest crystallisation duration of 0.5 h, the shortest time ever for this zeolite type, unadulterated CAN zeolites were crystallised albeit with the lowest peak intensity. A 0.5 h increment resulted in a little increase in peak intensities that was constant between 1h and 3h. At 6 h there was more than a fourfold increment in peak intensities from the initial duration, that remained approximately

constant thereafter. Since no appreciable change in the peak intensities was observed from 6 h to 72 h, 6 h was chosen as a duration that was sufficient for the nucleation and crystallisation of CAN zeolites. The Si/Al ratio at 0.5 h was 1.25 and as the crystallisation duration was increased from 1 h to 72 h, the decrease in Si/Al ratio was found to be in the range of 1.19 – 1.23.

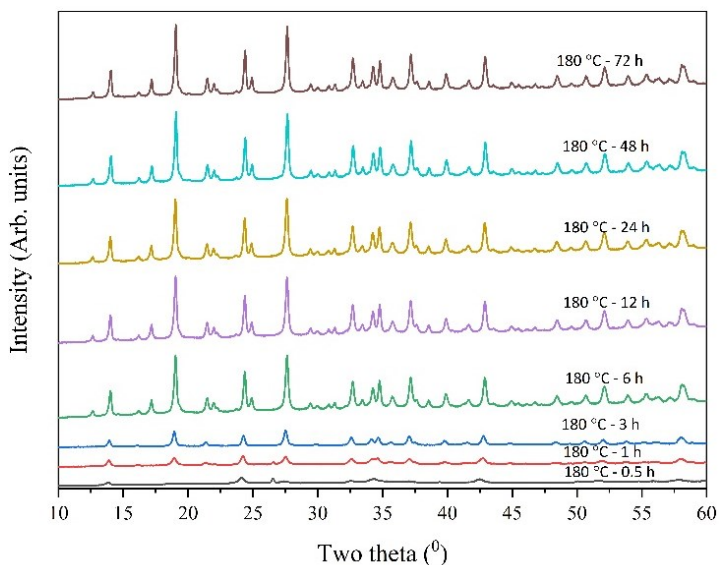


Figure 5-4. XRD pattern intensities at location d_{101} for 180 °C from 0 to 72 h.

Figure 5-5 shows the results for synthesis below 180 °C, the pivotal temperature at which the time-evolution synthesis was tested. It was found that CAN zeolite was formed even at the lowest temperature of 80 °C although the peak intensities were low. As the synthesis temperature was raised, the intensities increased until 150 °C. At 180 °C, there was no appreciable difference in the product hence no further increment in temperature was attempted. The extraneous peak that started as a double between 26 and 27° 2θ was first observed at 80 °C – 6 h, it gradually decreased as the temperature was increased. At 150 °C – 6 h, it was completely suppressed but it reoccurred at 180 °C – 6 h. The molar Si/Al ratio was in the range of 1.02 to 1.08 from the lowest temperature synthesis product to that of 150 °C – 6 h. 180 °C – 6 h product had a ratio of 1.2. Thus, the best conditions were selected as 150 °C for 6 h with clay to NaOH ratio of 1:1.2 (CAN – 6h).

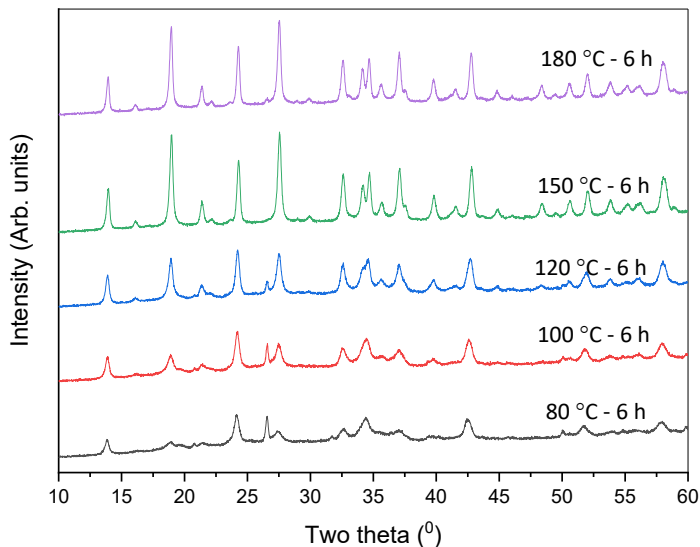


Figure 5-5. XRD pattern intensities at location d_{101} for 150 °C from 0 to 72 h.

The SEM and TEM images of the optimal CAN zeolite are shown in Figure 5-6. SEM image magnification of 40,000 times showed particles that are below 1 μm size range. From the TEM image in Figure 5-6 (b), an aggregate of small particles with sizes below 100 nm was observed. These particles were predominantly nonhomogeneous in shape.

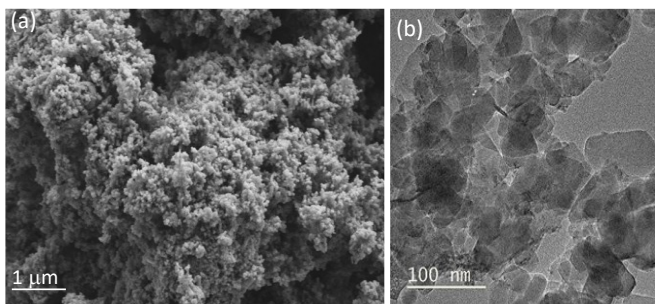


Figure 5-6. (a). SEM image of optimal CAN zeolite at 40k magnification and (b). TEM image of the optimal CAN zeolite.

The optimal CAN zeolite, CAN – 6 h, synthesized at 150 °C, had a BET specific surface area of 63 m²/g, t-plot micropore area of 9 m²/g, t-plot micropore volume of 0.004 m³/g, and an average pore width of 25 nm. The Si/Al ratio was 1.02 while the XRD crystallite size of the CAN particle was 31 nm.

5.5.3 Synthesis scale-up

A scale up of the synthesis from 1 to 8 times the starting materials consistently resulted in a uniform physicochemical characteristic of the CAN zeolite produced (Figure 5-7).

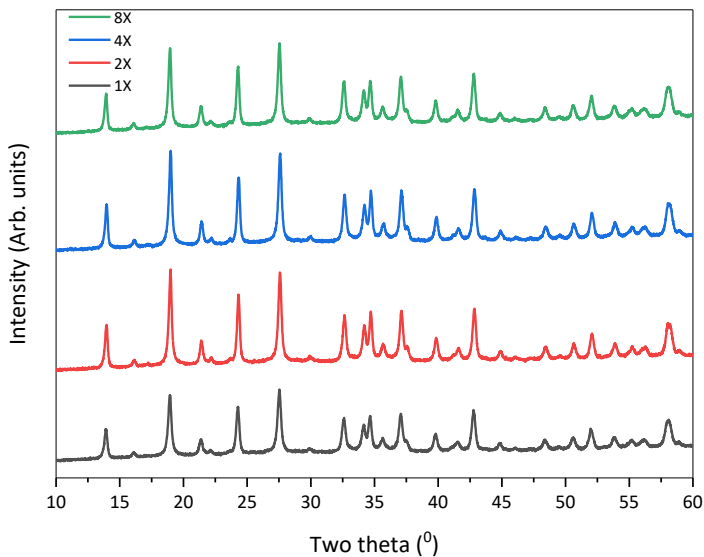


Figure 5-7. XRD patterns of scale up synthesis of CAN zeolite for 1X to 8X of the starting material.

The scale up products had specific surface areas, external surface areas, micropore volume, and pore dimensions that were similar (Table 5-1). The crystallite size, estimated using XRD, indicated that CAN zeolite size distribution was in the range of 31 to 38 nm. In comparison with a specific surface area (SSA) of 95 m²/g and micropore volume of 0.01 cm³/g of the starting material (clay), CAN zeolite synthesis resulted in the

reordering of morphological parameters as shown in Table 5-1. The BET specific surface area (SSA) was an average of 61.3 m²/g while the micropore volumes reduced by a magnitude of 10, too narrow for the adsorption of nitrogen. The small values for the micropore might be as a result of the blockage of the entrance to gas by the CAN zeolite anionic species leading to an underestimation of the micropore volume [180,186,187].

Table 5-1. BET and XRD data for the scale-up experiment.

Parameters	1X	2X	4X	8X
BET SSA (m ² /g)	63	57	62	63
t-Plot Micropore Area (m ² /g)	9	6	7	8
t-Plot Ext. Surface Area (m ² /g)	54	51	55	55
t-Plot micropore volume (cm ³ /g)	0.004	0.002	0.003	0.003
Ads. ave. pore width (nm)	25	30	31	26
XRD Crystallite size (nm)	31	36	38	38

A comparison of the N₂ adsorption/desorption data and the pore size distribution of the CAN zeolites obtained from the minimum and the maximum starting materials (1X and 8X) is shown in Figure 5-8. The BJH pore size distribution and the N₂ adsorption/desorption isotherms were similar, the zeolites had pores with sizes below 110 nm. The adsorption isotherms displayed characteristic type II behaviour; the narrow H3 hysteresis loop shows the isotherm is a type IIb. The type IIb isotherm is indicative of the formation of multilayers, the narrow hysteresis loop is from the pore inter-particle condensation [27,54,57].

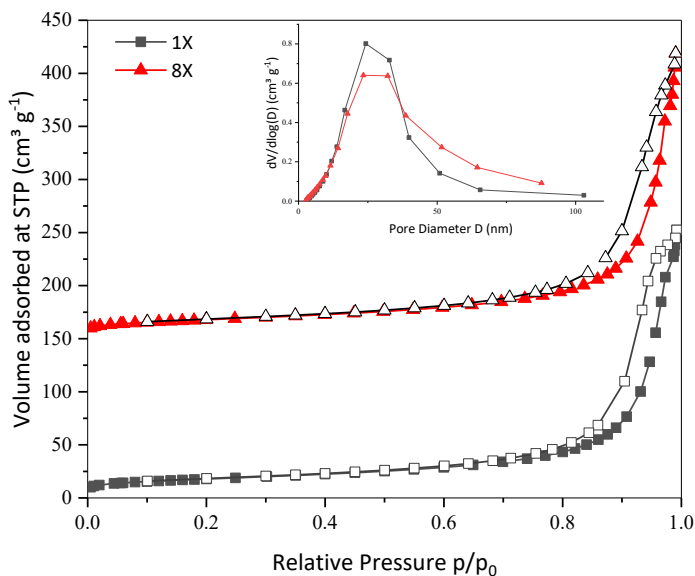


Figure 5-8. N₂ adsorption/desorption curves at -196 °C for 1X and 8X scale-up CAN zeolite, BJH pore size distribution in the insert. Opened symbols, desorption, closed symbols, adsorption. The isotherm for 8X was shifted by 150 units on the y – axis for clarity.

5.5.4 Simultaneous Removal of Heavy Metals

To determine the effects of time, adsorbent loading, and initial concentration has on the CAN zeolite uptake of Cd, Cu, Co, Pb, and Zn from aqueous solution, a 2³ factorial experimental design was used to plan and analyse the

experimental data. The design codes and the high and low levels of time, adsorbent loading, and the initial concentration is illustrated in Table 5-2. From the design matrix $2^3 = 8$, 16 experiments (including replicates) were performed.

Table 5-2. Factorial design factors and levels.

Factor	Coded symbol	Low level (-1)	High level (+1)
Time (min)	A	60	120
Ads. loading (g/L)	B	5	10
Initial conc. (mg/L)	C	200	400

The effects of the three factors on the uptake of the five metals by CAN zeolite is shown in the normal probability plots and Pareto charts from Figure 5-9 to Figure 5-18. The red square symbols in the normal probability plots identify the factors that significantly affect the uptake of each metal while the blue symbols represent insignificant factors. The significance or insignificance of a factor(s) is

determined by the difference between the p-values (the probability that a difference observed could be random) and α (significant) level of 0.05. For the Pareto charts, the absolute effect of the factors beyond the 2.306 line is considered significant. A mathematical model is used to represent the relationship between the metal uptake efficiency and the possible interactions between the factors. The regression model is not the same for each metal since a factor might be significant in one and insignificant in another. A general regression model for a three-factor experimental design is given in Equation 21:

$$y = \gamma_0 + \gamma_1 A + \gamma_2 B + \gamma_3 C + \gamma_{12} AB + \gamma_{13} AC + \gamma_{23} BC + \gamma_{123} ABC \quad \text{Equation 21}$$

where y is the predicted metal removal efficiency (%), γ_0 is a constant, γ_1 to γ_3 are the respective coefficients for A (time), B (adsorbent loading), and C (initial concentration).

The uptake of Co by CAN zeolite in a five-metal competitive adsorption system was significantly affected by the adsorbent amount as depicted in Figure 5-9 and

Figure 5-10. The regression expression for the removal of Co is shown in Equation 22.

$$Co (\%) = 54.0 - 0.29A - 5.8B - 0.2C + 0.03AB + 0.002AC + 0.022BC \quad \text{Equation 22}$$

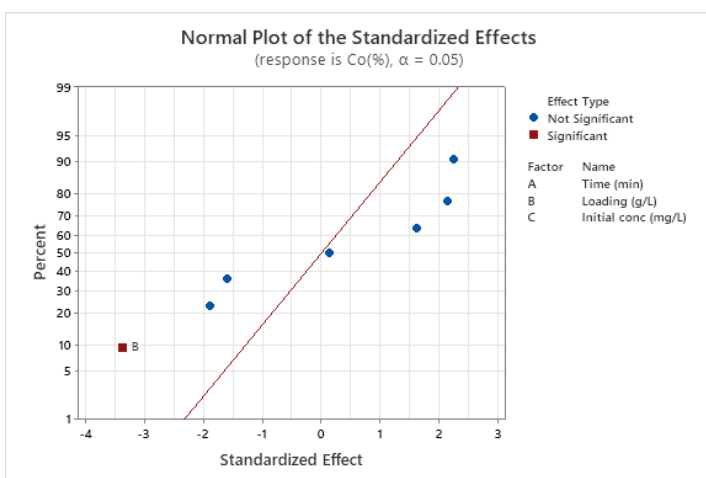


Figure 5-9. Normal probability plot for Co removal using CAN zeolite.

This shows the two-factor (instead of a three-factor) interactions between all the pairings, the adsorbent loading (B) being the most significant with a regression coefficient of -5.8. The adsorption of Co in a multicomponent adsorption system was poor, using the design analysis, it was evident that a significant increase in the adsorbent loading would increase the uptake of Co by CAN zeolite. The insignificant effect of time on the adsorption of Co is an important finding, an increase in time with the same low adsorbent would not result in any appreciable increase in the removal efficiency as indicated by the empirical equation and the Minitab plots for Co.

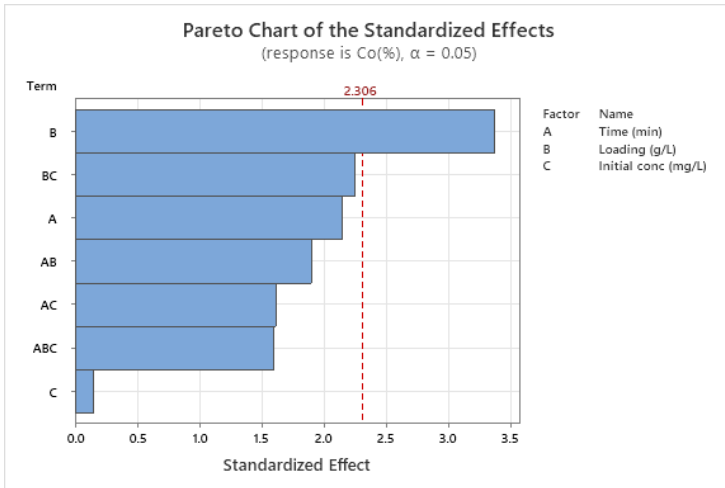


Figure 5-10. Pareto chart for Co removal using CAN zeolite.

Another poorly adsorbed metal, Zn, was found to have a regression expressing shown in Equation 23.

$$Zn (\%) = 102.1 - 0.59A - 10.91B - 0.36C + 0.06AB + 0.003AC + 0.04BC \quad \text{Equation 23}$$

The normalised plot of the standardised effects is shown in Figure 5-11 while the Pareto chart is shown in Figure 5-12.

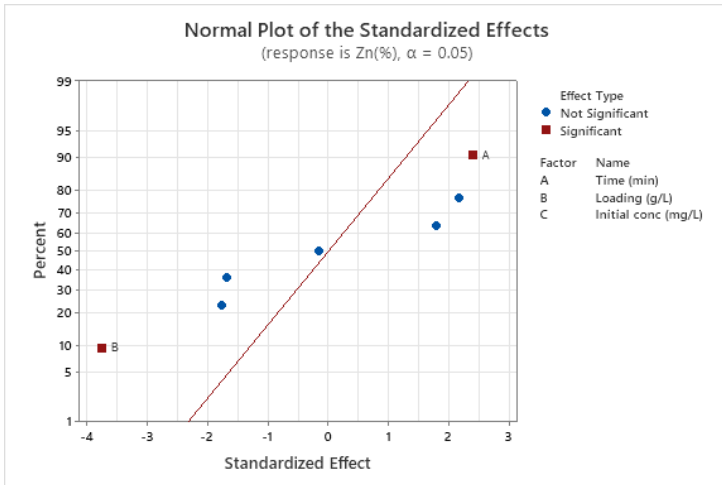


Figure 5-11. Normal probability plot for Zn removal using CAN zeolite.

The analysis indicated that although both time (A) and adsorbent loading (B) played significant roles in the uptake of Zn, unlike Co, an appreciable increase in the removal efficiency of Zn would require a simultaneous increase of both adsorbent loading and time. Of the three factors, the effects were in the decreasing order of adsorbent loading > time > initial concentration.

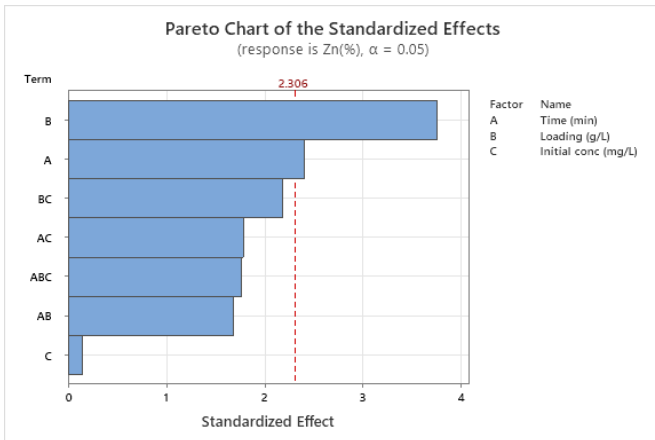


Figure 5-12. Pareto chart for Zn removal using CAN zeolite.

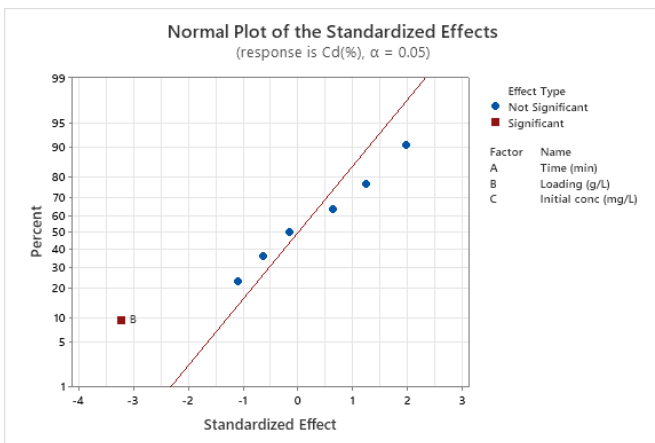


Figure 5-13. Normal probability plot for Cd removal using CAN zeolite.

The uptake of Cd by CAN zeolite was significantly affected by the adsorbent loading as shown in Figure 5-13 and Figure 5-14. The derived mathematical expression for the regression analysis is given in Equation 24.

$$Cd (\%) = 99.8 - 0.58A - 9.4 B - 0.28 C + 0.06AB + 0.003AC + 0.03BC \quad \text{Equation 24}$$

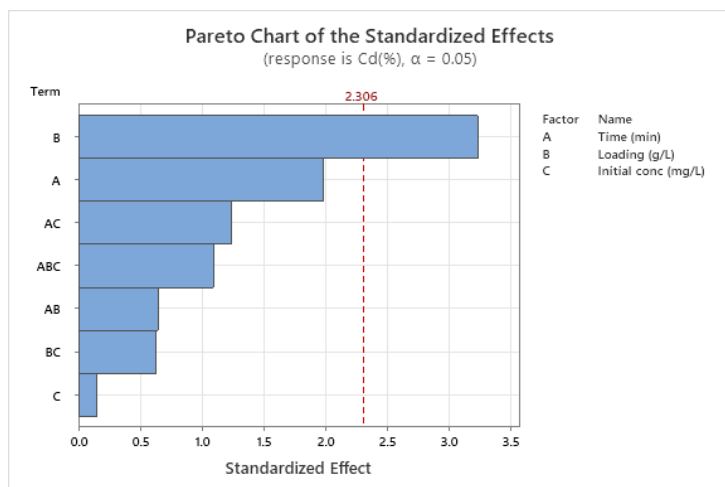


Figure 5-14. Pareto chart for Cd removal using CAN zeolite.

This implies that in the competition for adsorption sites with the other four metals, adsorption of Cd could occur within a short interval and at higher concentrations; an

increase or decrease in the adsorbent loading is the only factor that would significantly affect the uptake of Cd using CAN zeolite. This is also true for Pb and Cu as shown in Figure 5-15 to Figure 5-18. Thus, those three metals would be the most adsorbed in a five-metal adsorption system consisting of Cd, Cu, Pb, Co, and Zn.

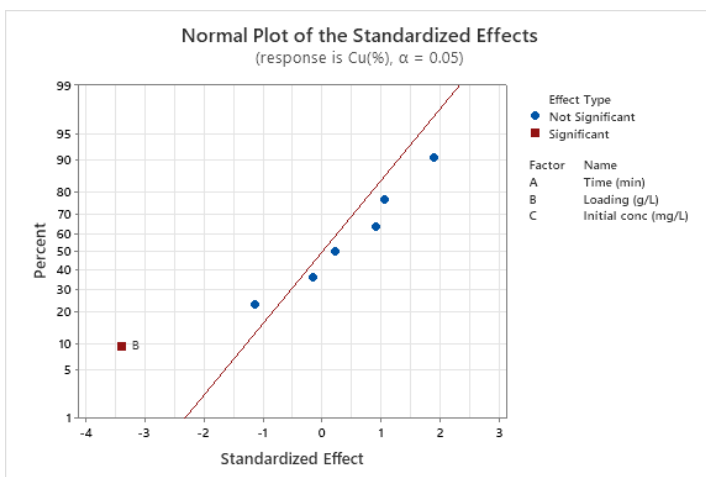


Figure 5-15. Normal probability plot for Cu removal using CAN zeolite.

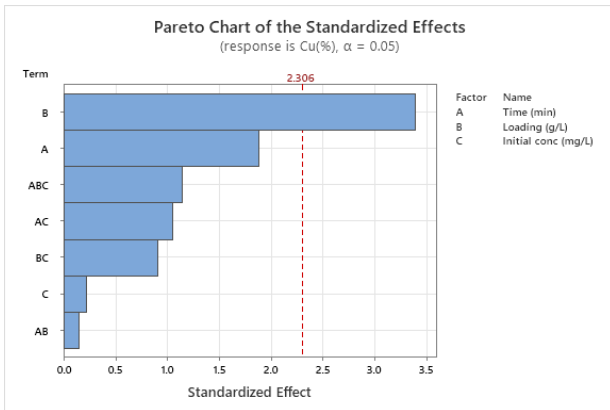


Figure 5-16. Pareto chart for Cu removal using CAN zeolite.

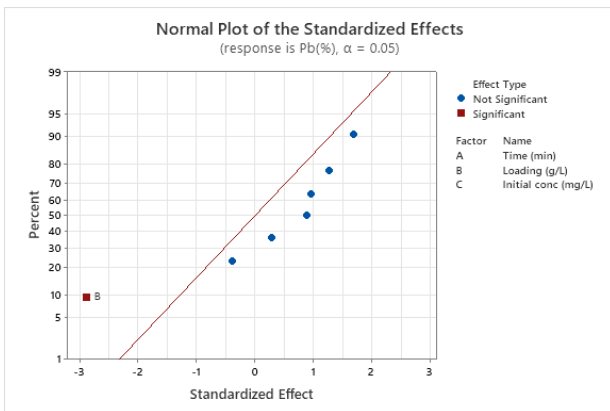


Figure 5-17. Normal probability plot for Pb removal using CAN zeolite.

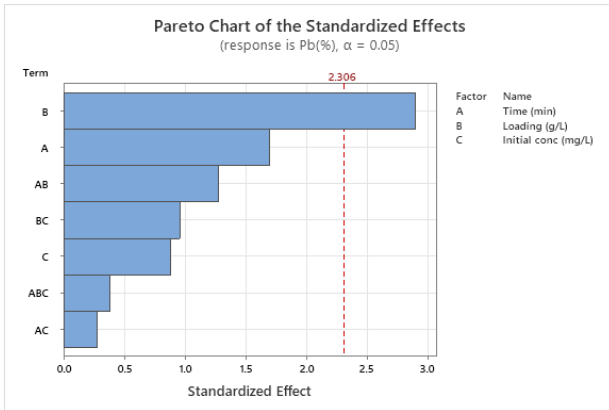


Figure 5-18. Pareto chart for Pb removal using CAN zeolite.

Having determined the optimal experimental requirements for Cd, Cu, Pb, Co, and Zn, a compromise was made in selecting the overall optimal experimental factors. Since Pb, Cu, and Cd were only affected by the adsorbent loading, Zn by both adsorbent loading and time, and Co by adsorbent loading alone, 60 min was chosen as sufficient time. In addition, an adsorbent loading of 10 g/L (above the factorial experimental low level of 5 g/L) and a concentration range of 50 to 400 mg/L were selected.

The experimental results of the simultaneous uptake of the five metals using CAN zeolite are shown in Table 5-3.

Table 5-3. The removal efficiency (%) for the simultaneous uptake of five metals by CAN zeolite, $C_0 = 50$ to 400 mg/L, at 60 min and adsorbent loading of 10 g/L.

C_0 (mg/ L)	Cu	Pb	Co	Cd	Zn
50	99.46	99.72	62.89	93.24	90.40
100	95.56	99.52	24.32	60.60	46.71
150	85.17	99.25	13.72	39.94	26.67
200	73.67	98.73	9.28	29.41	18.07
250	62.31	97.82	7.14	23.33	13.39
300	52.59	96.56	2.12	17.49	6.89
350	46.61	95.29	1.56	16.25	5.40
400	41.42	92.50	0.00	14.82	2.03

The decreasing selectivity trend was $Pb > Cu > Cd > Zn > Co$ at both low and high concentrations. The removal of Pb was comparable to FAU – type zeolites prepared from coal fly ash and peat ash. As discussed in Chapter 2

(Section 2.5.4), the disproportionate preference of Pb over the other metals competing for the available adsorption sites could be for reasons that include the radii of the hydrated cation and the electronegativities.

5.6 Conclusions

In summary, geophagical clays mixed with sodium hydroxide and aluminium sulphate octadecahydrate and treated in an autoclave at 150 °C for 6 h gave a single crystalline phase of CAN zeolites without the co – crystallisation of any side product. The CAN zeolite retained its compositional integrity when it was systematically scaled up to eight times the initial precursor amounts. To determine the efficacy of the prepared CAN zeolite for the simultaneous removal of five heavy metals from aqueous solutions, a factorial experimental design was used to obtain the optimal experimental conditions. It was found that the uptake of Cd, Cu, and Pb was affect by adsorbent loading only while Co was affected by both time and adsorbent loading. Zn

on the other hand, was only affected by the adsorbent loading. An experiment using the overall optimal experimental conditions was carried out and it was found that the metal removal trend of CAN was of the decreasing order of $Pb > Cu > Cd > Zn > Co$. The uptake of Pb was comparable to that obtained from FAU-type zeolites prepared from coal fly ash and peat ash.

The impacts of these findings include the following:

- i. The first cancrinite zeolite synthesised without the co-crystallisation of unwanted phases.
- ii. An optimal solvent - free method that significantly contributes to template free synthesis of zeolites.
- iii. Morphology control using either sodium carbonate decahydrate or aluminium sulphate octadecahydrate. This control affected the zeolite nucleation rate and the suppression of crystal growth.
- iv. A scale-up of the synthesis that produced a consistent textural and chemical characteristics.

6 GENERAL CONCLUSIONS AND FURTHER WORK

6.1 General Conclusions

The synthesis of zeolites from the three starting materials, coal fly ash, peat ash, and clay by the pre-alkali fusion and hydrothermal route was systematically optimised. For coal fly ash, this study showed that the extent of fly ash to water ratio was 1:15, beyond that, the product reverted to its pre hydrothermal treatment developmental stage. An optimal pre-treatment was development for the peat ash samples where a single step extraction with less energy usage was found, the development of LTAs and FAU-type zeolites from peat ash was found to depend on ageing temperature of 35 °C in addition to the Si/Al ratio of the precursor. This research utilised geophagic clay, for the first time, to synthesise FAU – type and CAN zeolites. The CAN zeolites were prepared by a solvent – free method that resulted in pure phase CAN crystals without the formation of side products.

It was found that the optimal faujasite zeolites from the three starting materials and the reference zeolite had some subtle differences. The decreasing order for Si/Al ratio was clay FAU > peat ash FAU > coal fly ash FAU > Zref FAU. The amount of water added in the synthesis of the faujasite zeolites was found to be in the decreasing order coal fly ash FAU > peat ash FAU = Zref FAU > clay FAU. To synthesise faujasite zeolites, coal fly ash and the clay samples required no initial purification while the peat ash samples required acid extraction for the removal of excess Ca and Fe. Even though FAU zeolites are usually superior in heavy metal uptake, this research found instances where Linde type A zeolites obtained from peat ash outperformed faujasite zeolites in the uptake of Pb, Cu, Cu, and Zn.

All the prepared zeolites could remove heavy metals in a multicomponent adsorption system. Faujasite zeolites from coal fly ash, peat ash, and clay, Linde type A zeolite from peat, and cancrinite zeolite from clay all showed a disproportionate selectivity for Pb at the minimal time

and the maximum concentration while Co was the least adsorbed. Of all the zeolites synthesised from coal fly ash, peat ash, and clay, that of peat ash gave an overall maximum uptake of heavy metals from aqueous solutions. In consideration of the purification required for peat ash samples, the zeolites from the clay samples used in this research were more easily synthesised. The cancrinites from clay offered a unique zeolite synthesis pathway whereby a solvent-free method produced a single phase cancrinite crystals for the first time.

This research set out to establish systematic methods for zeolite synthesis and for multicomponent adsorption systems. Even though the aims were achieved, the need for further work has been identified.

6.2 Further Work

The research described in this thesis has added to the literature on zeolite synthesis – both via hydrothermal and solvent – free synthesis routes. The adsorption

experiments used in this work for multicomponent adsorption systems are not common in literature which provide opportunities for further research work. Water pollution is dynamic and continuous research is required for the uptake of existing and emerging pollutants. Although this research used the synthesised adsorbents for the uptake of five heavy metals from aqueous solutions, an increased pollutant matrix could be attempted for more than five mix of heavy metals. Further studies on the performance of the prepared adsorbents (faujasites, Linde type A, and cancrinites) can also be tested for a combination of organic and inorganic pollutants. The findings would be of importance to academia and industry concerning water pollution abatement.

REFERENCES

- [1] D. Novembre, D. Gimeno, P. Cappelletti, S.F. Graziano, A case study of zeolitization process:"Tufo Rosso a Scorie Nere" (Vico volcano, Italy): Inferences for a general model, *Eur. J. Mineral.* 33 (2021) 315–328. <https://doi.org/10.5194/ejm-33-315-2021>.
- [2] M. Moshoeshoe, M. Silas Nadiye-Tabbiruka, V. Obuseng, A Review of the Chemistry, Structure, Properties and Applications of Zeolites, *Am. J. Mater. Sci.* (2017) 196–221. <https://doi.org/10.5923/j.materials.20170705.12>.
- [3] D.W. Breck, Crystalline molecular sieves, *J. Chem. Educ.* 41 (1964) 678–683. <https://pubs.acs.org/sharingguidelines> (accessed August 26, 2021).
- [4] P. Payra, P.K. Dutta, Zeolites: A Primer, *ChemInform.* 35 (2004) 1–19. <https://doi.org/10.1002/chin.200438229>.

- [5] Structure Commission, Framework Type Codes, Int. Zeolite Assoc. 5 (2019) 2020. <http://www.iza-structure.org/> (accessed September 10, 2018).
- [6] R. Lobo, Introduction to the Structural Chemistry of Zeolites, in: Handb. Zeolite Sci. Technol., 2003: pp. 65–89. <https://doi.org/10.1201/9780203911167.ch3>.
- [7] J. Weitkamp, Zeolites and catalysis, Solid State Ionics. 131 (2000) 175–188. [https://doi.org/10.1016/S0167-2738\(00\)00632-9](https://doi.org/10.1016/S0167-2738(00)00632-9).
- [8] B. Jha, D.N. Singh, Fly Ash Zeolites, 1st ed., Springer Singapore, Singapore, 2016. <https://doi.org/10.1007/978-981-10-1404-8>.
- [9] D.N. Stamires, Properties of the zeolite, faujasite, substitutional series: A review with new data, Clays Clay Miner. 21 (1973) 379–389. <https://doi.org/10.1346/CCMN.1973.0210514>.
- [10] R.M. Milton, Molecular sieve adsorbents, 2,882,244, 1959.

- [11] J. Warzywoda, M. Valcheva-Traykova, G.A. Rossetti, N. Baç, R. Joesten, S.L. Suib, A. Sacco, Characterization of zeolites A and X grown in low earth orbit, *J. Cryst. Growth.* 220 (2000) 150–160. [https://doi.org/10.1016/S0022-0248\(00\)00660-6](https://doi.org/10.1016/S0022-0248(00)00660-6).
- [12] S.N. Azizi, A. Alavi Daghigh, M. Abrishamkar, Phase transformation of zeolite P to γ and analcime zeolites due to changing the time and temperature, *J. Spectrosc.* 1 (2013). <https://doi.org/10.1155/2013/428216>.
- [13] Q. Liu, A. Navrotsky, Synthesis of nitrate sodalite: An in situ scanning calorimetric study, *Geochim. Cosmochim. Acta.* 71 (2007) 2072–2078. <https://doi.org/10.1016/j.gca.2007.01.011>.
- [14] C. Belviso, State-of-the-art applications of fly ash from coal and biomass: A focus on zeolite synthesis processes and issues, *Prog. Energy Combust. Sci.* 65 (2018) 109–135. <https://doi.org/10.1016/j.peccs.2017.10.004>.

- [15] S.M. Auerbach, K.A. Carrado, P.K. Dutta, MFI: A Case Study of Zeolite Synthesis, in: S.M. Auerbach, K.A. Carrado, P.K. Dutta (Eds.), *Handb. Zeolite Sci. Technol.*, 1st ed., CRC Press, 2003: pp. 37–91. <https://doi.org/10.1201/9780203911167-8>.
- [16] S. Mintova, *Verified Syntheses of Zeolitic materials: Third Edition*, 2016. http://www.iza-online.org/synthesis/VS_3rdEd.pdf.
- [17] X. Querol, N. Moreno, J.C. Umaa, A. Alastuey, E. Hernández, A. López-Soler, F. Plana, Synthesis of zeolites from coal fly ash: an overview, *Int. J. Coal Geol.* 50 (2002) 413–423. [https://doi.org/10.1016/S0166-5162\(02\)00124-6](https://doi.org/10.1016/S0166-5162(02)00124-6).
- [18] R.W. Thompson, Nucleation, growth, and seeding in zeolite synthesis, in: H. Robson, K.P.B.T.-V.S. of Z.M. Lillerud (Eds.), *Verif. Synth. Zeolitic Mater.*, Elsevier Science, Amsterdam, 2001: pp. 21–23. <https://doi.org/10.1016/b978-044450703-7/50100-9>.

- [19] M.M.J. Treacy, J.B. Higgins, Collection of Simulated XRD Powder Patterns for Zeolites Fifth (5th) Revised Edition, 2007. <https://doi.org/10.1016/B978-0-444-53067-7.X5470-7>.
- [20] H. Khan, A.S. Yerramilli, A. D'Oliveira, T.L. Alford, D.C. Boffito, G.S. Patience, Experimental methods in chemical engineering: X-ray diffraction spectroscopy—XRD, *Can. J. Chem. Eng.* 98 (2020) 1255–1266. <https://doi.org/10.1002/cjce.23747>.
- [21] Thermo scientific, Energy Dispersive X-Ray Fluorescence, EDXRF, for Material Analysis and Sample Identification Using Niton Handheld XRF Analysers from Thermo Scientific, 2007. <https://www.azom.com/article.aspx?ArticleID=5251> (accessed September 28, 2021).
- [22] B. Kwiecińska, S. Pusz, B.J. Valentine, Application of electron microscopy TEM and SEM for analysis of coals, organic-rich shales and carbonaceous

matter, *Int. J. Coal Geol.* 211 (2019).
<https://doi.org/10.1016/j.coal.2019.05.010>.

[23] A. Salman Ali, Application of Nanomaterials in Environmental Improvement, in: *Nanotechnol. Environ.*, IntechOpen, 2020: p. 11.
<https://doi.org/10.5772/intechopen.91438>.

[24] S. Brunauer, P.H. Emmett, E. Teller, Adsorption of Gases in Multimolecular Layers, *J. Am. Chem. Soc.* 60 (2002) 309–319.
<https://doi.org/10.1021/ja01269a023>.

[25] K.S.W. Sing, Assessment of Surface Area by Gas Adsorption, in: *Adsorpt. by Powders Porous Solids Princ. Methodol. Appl. Second Ed.*, Academic Press, 2013: pp. 237–268.
<https://doi.org/10.1016/B978-0-08-097035-6.00007-3>.

[26] ISO [International Organization for Standardization], Determination of the specific surface area of solids by gas adsorption - BET

method (ISO 9277:2010(E)), Ref. Number ISO. 9277 (2010) 30 pp. <https://www.iso.org/standard/44941.html> (accessed September 3, 2021).

- [27] M. Thommes, K. Kaneko, A. V Neimark, J.P. Olivier, F. Rodriguez-Reinoso, J. Rouquerol, K.S.W. Sing, Physisorption of gases, with special reference to the evaluation of surface area and pore size distribution (IUPAC Technical Report), *Pure Appl. Chem.* 87 (2015) 1051–1069. <https://doi.org/10.1515/pac-2014-1117>.
- [28] Micrometrics Instrument Corporation, The science and technology of small particles accelerated surface area and porosimetry system, (2020). <https://docplayer.net/65259936-Asap-accelerated-surface-area-and-porosimetry-system-the-science-and-technology-of-small-particles.html> (accessed September 28, 2021).
- [29] F. Caruso, S. Mantellato, M. Palacios, R.J. Flatt, ICP-

OES method for the characterization of cement pore solutions and their modification by polycarboxylate-based superplasticizers, *Cem. Concr. Res.* 91 (2017) 52–60. <https://doi.org/10.1016/j.cemconres.2016.10.007>

- [30] L.F.O. Silva, T. Moreno, X. Querol, An introductory TEM study of Fe-nanominerals within coal fly ash, *Sci. Total Environ.* 407 (2009) 4972–4974. <https://doi.org/10.1016/j.scitotenv.2009.05.044>.
- [31] B.J. Inkson, Scanning Electron Microscopy (SEM) and Transmission Electron Microscopy (TEM) for Materials Characterization, in: *Mater. Charact. Using Nondestruct. Eval. Methods*, Woodhead Publishing, 2016: pp. 17–43. <https://doi.org/10.1016/B978-0-08-100040-3.00002-X>.
- [32] V. Komvokis, L.X.L. Tan, M. Clough, S.S. Pan, B. Yilmaz, Zeolites in fluid catalytic cracking (FCC), in:

- Zeolites Sustain. Chem. Synth. Charact. Catal. Appl., Springer, Berlin, Heidelberg, Berlin, 2015: pp. 271–297. https://doi.org/10.1007/978-3-662-47395-5_8.
- [33] K.G. Strohmaier, Chapter 3. Synthesis of Zeolites, in: Zeolites Catal. Prop. Appl., 2017: pp. 73–102. <https://doi.org/10.1039/9781788010610-00073>.
- [34] S.M. Auerbach, K.A. Carrado, P.K. Dutta, Handbook of zeolite science and technology, Focus Catal. 2004 (2004) 8. [https://doi.org/10.1016/s1351-4180\(04\)00164-3](https://doi.org/10.1016/s1351-4180(04)00164-3).
- [35] C.S. Cundy, P.A. Cox, The hydrothermal synthesis of zeolites: History and development from the earliest days to the present time, Chem. Rev. 103 (2003) 663–701. <https://doi.org/10.1021/cr020060i>.
- [36] C. Amrhein, G.H. Haghnia, T.S. Kim, P.A. Mosher, R.C. Gagajena, T. Amanios, L. De La Torre, Synthesis and properties of zeolites from coal fly

- ash, Environ. Sci. Technol. 30 (1996) 735–742.
<https://doi.org/10.1021/es940482c>.
- [37] K. Ojha, N.C. Pradhan, A.N. Samanta, Zeolite from fly ash: Synthesis and characterization, Bull. Mater. Sci. 27 (2004) 555–564.
<https://doi.org/10.1007/BF02707285>.
- [38] J.L.X. Hong, T. Maneerung, S.N. Koh, S. Kawi, C.H. Wang, Conversion of Coal Fly Ash into Zeolite Materials: Synthesis and Characterizations, Process Design, and Its Cost-Benefit Analysis, Ind. Eng. Chem. Res. 56 (2017) 11565–11574.
<https://doi.org/10.1021/acs.iecr.7b02885>.
- [39] J. Szerement, A. Szatanik-Kloc, R. Jarosz, T. Bajda, M. Mierzwa-Hersztek, Contemporary applications of natural and synthetic zeolites from fly ash in agriculture and environmental protection, J. Clean. Prod. 311 (2021) 127461.
<https://doi.org/10.1016/j.jclepro.2021.127461>.
- [40] T. Aldahri, J. Behin, H. Kazemian, S. Rohani,

Synthesis of zeolite Na-P from coal fly ash by thermo-sonochemical treatment, *Fuel*. 182 (2016) 494–501.

<https://doi.org/10.1016/j.fuel.2016.06.019>.

[41] Franus W., Characterisation of X-type zeolite prepared from coal fly ash, *Polish J. Environ. Stud.* 21 (2012) 337–343.

[42] A. Khaleque, M.M. Alam, M. Hoque, S. Mondal, J. Bin Haider, B. Xu, M.A.H. Johir, A.K. Karmakar, J.L. Zhou, M.B. Ahmed, M.A. Moni, Zeolite synthesis from low-cost materials and environmental applications: A review, *Environ. Adv.* 2 (2020) 100019.

<https://doi.org/10.1016/j.envadv.2020.100019>.

[43] E.A. Abdelrahman, Y.G. Abou El-Reash, H.M. Youssef, Y.H. Kotp, R.M. Hegazey, Utilization of rice husk and waste aluminum cans for the synthesis of some nanosized zeolite, zeolite/zeolite, and geopolymer/zeolite products for the efficient

removal of Co(II), Cu(II), and Zn(II) ions from aqueous media, *J. Hazard. Mater.* 401 (2021). <https://doi.org/10.1016/j.jhazmat.2020.123813>.

- [44] T. Wajima, Synthesis of zeolite from blast furnace slag using alkali fusion with addition of EDTA, in: *Adv. Mater. Res.*, Trans Tech Publications Ltd, 2014: pp. 124–127. <https://doi.org/10.4028/www.scientific.net/AMR.1044-1045.124>.
- [45] H. Guo, L. Tang, B. Yan, K. Wan, P. Li, NaA zeolite derived from blast furnace slag: Its application for ammonium removal, *Water Sci. Technol.* 76 (2017) 1140–1149. <https://doi.org/10.2166/wst.2017.294>.
- [46] A. López-Delgado, J.I. Robla, I. Padilla, S. López-Andrés, M. Romero, Zero-waste process for the transformation of a hazardous aluminum waste into a raw material to obtain zeolites, *J. Clean. Prod.* 255 (2020).

<https://doi.org/10.1016/j.jclepro.2020.120178>.

- [47] M. Yoldi, E.G. Fuentes-Ordoñez, S.A. Korili, A. Gil, Zeolite synthesis from aluminum saline slag waste, *Powder Technol.* 366 (2020) 175–184. <https://doi.org/10.1016/j.powtec.2020.02.069>.
- [48] M. Esaifan, L.N. Warr, G. Grathoff, T. Meyer, M.T. Schafmeister, A. Kruth, H. Testrich, Synthesis of hydroxy-sodalite/cancrinite zeolites from calcite-bearing kaolin for the removal of heavy metal ions in aqueous media, *Minerals.* 9 (2019) 484. <https://doi.org/10.3390/min9080484>.
- [49] M.A. Moneim, E.A. Ahmed, Synthesis of Faujasite from Egyptian Clays: Characterizations and Removal of Heavy Metals, *Geomaterials.* 05 (2015) 68–76. <https://doi.org/10.4236/gm.2015.52007>.
- [50] O.O. Ltaief, S. Siffert, S. Fourmentin, M. Benzina, Synthesis of Faujasite type zeolite from low grade Tunisian clay for the removal of heavy metals from aqueous waste by batch process: Kinetic and

equilibrium study, *Comptes Rendus Chim.* 18
(2015) 1123–1133.
<https://doi.org/10.1016/j.crci.2015.03.013>.

- [51] C. Belviso, F. Cavalcante, G. Niceforo, A. Lettino, Sodalite, faujasite and A-type zeolite from 2:1dioctahedral and 2:1:1 trioctahedral clay minerals. A singular review of synthesis methods through laboratory trials at a low incubation temperature, *Powder Technol.* 320 (2017) 483–497.
<https://doi.org/10.1016/j.powtec.2017.07.039>.
- [52] V. Wernert, O. Schaef, L. Aloui, C. Chassigneux, F. Ayari, D. Ben Hassen Chehimi, R. Denoyel, Cancrinite synthesis from natural kaolinite by high pressure hydrothermal method: Application to the removal of Cd^{2+} and Pb^{2+} from water, *Microporous Mesoporous Mater.* 301 (2020).
<https://doi.org/10.1016/j.micromeso.2020.110209>.

- [53] O.O. Ltaief, S. Siffert, C. Poupin, S. Fourmentin, M. Benzina, Optimal Synthesis of Faujasite-Type Zeolites with a Hierarchical Porosity from Natural Clay, *Eur. J. Inorg. Chem.* 2015 (2015) 4658–4665. <https://doi.org/10.1002/ejic.201500537>.
- [54] J. Rouquerol, F. Rouquerol, P. Llewellyn, G. Maurin, K.S.W. Sing, *Adsorption by Powders and Porous Solids: Principles, Methodology and Applications: Second Edition*, 2013. <https://doi.org/10.1016/C2010-0-66232-8>.
- [55] F. Rouquerol, J. Rouquerol, K.S.W. Sing, G. Maurin, P. Llewellyn, Introduction, in: *Adsorpt. by Powders Porous Solids Princ. Methodol. Appl. Second Ed.*, Academic Press, 2014: pp. 1–24. <https://doi.org/10.1016/B978-0-08-097035-6.00001-2>.
- [56] K.A. Cychoz, M. Thommes, Progress in the Physisorption Characterization of Nanoporous Gas Storage Materials, *Engineering*. 4 (2018) 559–566.

<https://doi.org/10.1016/j.eng.2018.06.001>.

- [57] K.S.W. Sing, R.T. Williams, Physisorption hysteresis loops and the characterization of nanoporous materials, *Adsorpt. Sci. Technol.* 22 (2004) 773–782. <https://doi.org/10.1260/0263617053499032>.
- [58] N. Ayawei, A.N. Ebelegi, D. Wankasi, Modelling and Interpretation of Adsorption Isotherms, *J. Chem.* 2017 (2017) 1–11. <https://doi.org/10.1155/2017/3039817>.
- [59] I. Langmuir, The constitution and fundamental properties of solids and liquids. Part I. Solids, *J. Am. Chem. Soc.* 38 (1916) 2221–2295. <https://doi.org/10.1021/ja02268a002>.
- [60] K.Y. Foo, B.H. Hameed, Insights into the modeling of adsorption isotherm systems, *Chem. Eng. J.* 156 (2010) 2–10. <https://doi.org/10.1016/j.cej.2009.09.013>.
- [61] Y.S. Ho, J.F. Porter, G. McKay, Equilibrium isotherm studies for the sorption of divalent metal ions onto

- peat: Copper, nickel and lead single component systems, *Water. Air. Soil Pollut.* 141 (2002) 1–33. <https://doi.org/10.1023/A:1021304828010>.
- [62] A.R. Khan, T.A. Al-Bahri, A. Al-Haddad, Adsorption of phenol based organic pollutants on activated carbon from multi-component dilute aqueous solutions, *Water Res.* 31 (1997) 2102–2112. [https://doi.org/10.1016/S0043-1354\(97\)00043-2](https://doi.org/10.1016/S0043-1354(97)00043-2).
- [63] S. Kumar, M. Zafar, J.K. Prajapati, S. Kumar, S. Kannepalli, Modeling studies on simultaneous adsorption of phenol and resorcinol onto granular activated carbon from simulated aqueous solution, *J. Hazard. Mater.* 185 (2011) 287–294. <https://doi.org/10.1016/j.jhazmat.2010.09.032>.
- [64] H.M.F. Freundlich, About the adsorption in solution, *Z. Phys. Chem.* 57 (1906) 385–471.
- [65] J. Tóth, Calculation of the BET-compatible surface area from any Type I isotherms measured above the critical temperature, *J. Colloid Interface Sci.*

225 (2000) 378–383.
<https://doi.org/10.1006/jcis.2000.6723>.

- [66] J. Toth, State Equations of Solid-Gas Interface Layers, *Acta Chim. Acad. Sci. Hungaricae*. 69 (1971) 311-.
- [67] O. Hamdaoui, E. Naffrechoux, Modeling of adsorption isotherms of phenol and chlorophenols onto granular activated carbon. Part II. Models with more than two parameters, *J Hazard Mater*. 147 (2007) 401–411.
<https://doi.org/10.1016/j.jhazmat.2007.01.023>.
- [68] M.A. Al-Ghouthi, D.A. Da’ana, Guidelines for the use and interpretation of adsorption isotherm models: A review, *J. Hazard. Mater*. 393 (2020) 122383.
<https://doi.org/10.1016/j.jhazmat.2020.122383>.
- [69] O. Hamdaoui, E. Naffrechoux, Modeling of adsorption isotherms of phenol and chlorophenols onto granular activated carbon. Part II. Models with more than two parameters, *J. Hazard. Mater*.

147 (2007) 401–411.
<https://doi.org/10.1016/j.jhazmat.2007.01.023>.

[70] H.K. Boparai, M. Joseph, D.M. O’Carroll, Kinetics and thermodynamics of cadmium ion removal by adsorption onto nano zerovalent iron particles, *J. Hazard. Mater.* 186 (2011) 458–465.
<https://doi.org/10.1016/j.jhazmat.2010.11.029>.

[71] G. William Kajokumba, S. Emik, A. Öngen, H. Kurtulus Özcan, S. Aydın, Modelling of Adsorption Kinetic Processes—Errors, Theory and Application, in: *Adv. Sorption Process Appl.*, IntechOpen, 2018.
<https://doi.org/10.5772/intechopen.80495>.

[72] Y.S. Ho, G. McKay, Kinetic models for the sorption of dye from aqueous solution by wood, *Process Saf. Environ. Prot.* 76 (1998) 183–191.
<https://doi.org/10.1205/095758298529326>.

[73] L. Largitte, R. Pasquier, A review of the kinetics adsorption models and their application to the adsorption of lead by an activated carbon, *Chem.*

Eng. Res. Des. 109 (2016) 495–504.
<https://doi.org/10.1016/j.cherd.2016.02.006>.

[74] J.P. Simonin, J. Boute, J. Bouté, Intraparticle Diffusion-Adsorption Model to Describe Liquid/Solid Adsorption Kinetics, *Rev. Mex. Ing. Quim.* 15 (2016) 161–173. <https://hal.sorbonne-universite.fr/hal-01312850> (accessed July 30, 2019).

[75] N.A. Anjum, *Phytotechnologies: Remediation of Environmental Contaminants*, CRC Press Inc, 2012. <https://www.dawsonera.com:443/abstract/9781439875193>.

[76] A. Fairbrother, R. Wenstel, K. Sappington, W. Wood, Framework for Metals Risk Assessment, *Ecotoxicol. Environ. Saf.* 68 (2007) 145–227. <https://doi.org/10.1016/j.ecoenv.2007.03.015>.

[77] S. Chowdhury, M.A.J. Mazumder, O. Al-Attas, T. Husain, Heavy metals in drinking water: Occurrences, implications, and future needs in

developing countries, *Sci. Total Environ.* 569–570
(2016) 476–488.
<https://doi.org/10.1016/j.scitotenv.2016.06.166>.

- [78] N. Graham, *Guidelines for Drinking-Water Quality*, 2nd edition, Addendum to Volume 1 – Recommendations, World Health Organisation, Geneva, 1998, 36 pages, *Urban Water*. 1 (1999) 183. [https://doi.org/10.1016/s1462-0758\(00\)00006-6](https://doi.org/10.1016/s1462-0758(00)00006-6).
- [79] International Agency for Research on Cancer, C. International Agency for Research on, *IARC Monographs: Arsenic, Metals, Fibres, and Dusts*, IARC Monogr. Eval. Carcinog. Risks to Humans. 100C (2012) 527. <http://monographs.iarc.fr> (accessed July 26, 2018).
- [80] G. Fellenberg, Ddc, *The chemistry of pollution*, 3rd ed., rev. and expanded, Wiley, Chichester, 2000. <http://capitadiscovery.co.uk/mmu/items/130195> 8.

- [81] S.E. Manahan, Environmental chemistry, 9th ed, CRC Taylor & Francis [distributor], Boca Raton, Fla London, 2009.
<http://capitadiscovery.co.uk/mmu/items/1901122>.
- [82] J. Sekizawa, Concise International Chemical Assessment Document (CICAD): a new chemical safety series in IPCS, internationalizing national reviews, Eisei Shikenjo Hokoku. (1996) 89–94.
<http://www.who.int/ipcs/publications/cicad/cicad69.pdf> (accessed August 29, 2018).
- [83] Copper in Drinking Water, National Academies Press, Washington, D.C., 2000.
<https://doi.org/10.17226/9782>.
- [84] G. Brundtland, UN Brundtland Commission Report, Our Common Future. (1987).
- [85] B. Shah, D. Pandya, H. Patel, A. Ayalew, A. Shah, Zeolitic Composites From Agricultural Detritus for Pollution Remedy: a Review, J. Crit. Rev. 3 (2016)

41–49.

<https://innovareacademics.in/journals/index.php/jcr/article/view/11219/6321>.

- [86] I. Anastopoulos, A. Mittal, M. Usman, J. Mittal, G. Yu, A. Núñez-Delgado, M. Kornaros, A review on halloysite-based adsorbents to remove pollutants in water and wastewater, *J. Mol. Liq.* 269 (2018) 855–868.

<https://doi.org/10.1016/j.molliq.2018.08.104>.

- [87] M. Visa, P. Nicoleta, A. Chelaru, Zeolite Materials Obtained from Fly Ash Used for Removal of Heavy Metals and dye from Complex Wastewaters, in: 2017 World Coal Ash, Lexington, KY, 2017.

<https://worldofcoalash.org/wp-content/uploads/2018/03/technical-sessions-woca2017.pdf>.

- [88] A. Hamadi, K. Nabih, Synthesis of Zeolites Materials Using Fly Ash and Oil Shale Ash and Their Applications in Removing Heavy Metals from

Aqueous Solutions, *J. Chem.* 2018 (2018) 1–12.
<https://doi.org/10.1155/2018/6207910>.

- [89] M. Visa, Synthesis and characterization of new zeolite materials obtained from fly ash for heavy metals removal in advanced wastewater treatment, *Powder Technol.* 294 (2016) 338–347.
<https://doi.org/10.1016/j.powtec.2016.02.019>.
- [90] O.E. Abdel Salam, N.A. Reiad, M.M. ElShafei, A study of the removal characteristics of heavy metals from wastewater by low-cost adsorbents, *J. Adv. Res.* 2 (2011) 297–303.
<https://doi.org/10.1016/j.jare.2011.01.008>.
- [91] C.A. Rios, C.D. Williams, C.L. Roberts, C.A. Ríos, C.D. Williams, C.L. Roberts, Removal of heavy metals from acid mine drainage (AMD) using coal fly ash, natural clinker and synthetic zeolites, *J Hazard Mater.* 156 (2008) 23–35.
<https://doi.org/10.1016/j.jhazmat.2007.11.123>.
- [92] C. Belviso, Zeolite for potential toxic metal uptake

from contaminated soil: A brief review, *Processes*.
8 (2020). <https://doi.org/10.3390/pr8070820>.

- [93] E. Erdem, N. Karapinar, R. Donat, The removal of heavy metal cations by natural zeolites, *J. Colloid Interface Sci.* 280 (2004) 309–314. <https://doi.org/10.1016/j.jcis.2004.08.028>.
- [94] S. Malamis, E. Katsou, A review on zinc and nickel adsorption on natural and modified zeolite, bentonite and vermiculite: Examination of process parameters, kinetics and isotherms, *J. Hazard. Mater.* 252–253 (2013) 428–461. <https://doi.org/10.1016/j.jhazmat.2013.03.024>.
- [95] T. Motsi, N.A. Rowson, M.J.H.H. Simmons, Adsorption of heavy metals from acid mine drainage by natural zeolite, *Int. J. Miner. Process.* 92 (2009) 42–48. <https://doi.org/10.1016/j.minpro.2009.02.005>.
- [96] G. Blanchard, M. Maunaye, G. Martin, Removal of heavy metals from waters by means of natural

- zeolites, *Water Res.* 18 (1984) 1501–1507.
[https://doi.org/10.1016/0043-1354\(84\)90124-6](https://doi.org/10.1016/0043-1354(84)90124-6).
- [97] U. Wingenfelder, C. Hansen, G. Furrer, R. Schulin, Removal of heavy metals from mine waters by natural zeolites, *Environ. Sci. Technol.* 39 (2005) 4606–4613. <https://doi.org/10.1021/es048482s>.
- [98] T. Cheng, C. Chen, R. Tang, C.H. Han, Y. Tian, Competitive Adsorption of Cu, Ni, Pb, and Cd from Aqueous Solution Onto Fly Ash-Based Linde F(K) Zeolite, *Iran. J. Chem. Chem. Eng. English Ed.* 37 (2018) 61–72.
http://www.ijcce.ac.ir/article_31971_e25cf575d60edbc02902f7aad53c6952.pdf (accessed August 12, 2019).
- [99] I.H.A. El Maksod, S. Kosa, E.Z. Hegazy, The Effect of Preparation Conditions on the Removal Efficiency of Water Pollutants Using LTA Zeolite, *J. Water Resour. Prot.* 09 (2017) 811–821.
<https://doi.org/10.4236/jwarp.2017.97054>.

- [100] C. Mahamadi, F. Almomani, On the dominance of Pb during competitive biosorption from multi-metal systems: A review, *Cogent Environ. Sci.* 5 (2019) 2–32. <https://doi.org/10.1080/23311843.2019.1635335>.
- [101] USEPA, Understanding variation in partition coefficient, K_d , values. Volume I: The K_d Model, Methods of Measurement, and Application of Chemical Reaction Codes, 1999. <https://www.google.com/url?sa=t&rct=j&q=&esrc=s&source=web&cd=4&ved=0ahUKEwi045ai9v3NAhVMQSYKHV9wD0QQFgg0MAM&url=https%3A%2F%2Fwww.epa.gov%2Fsites%2Fproduction%2Ffiles%2F2015-05%2Fdocuments%2F402-r-99-004a.pdf&usq=AFQjCNEMons5lWXRBeJOTNYK7FnQt8tGpA&sig2=d> (accessed September 8, 2021).
- [102] Federal Highway Administration, A. Federal Highway, User Guidelines for Waste and Byproduct Materials in Pavement Construction:

Sewage Sludge Ash – Material Description, FHWA-
RD-97-148. (2012).

<https://www.fhwa.dot.gov/publications/research/infrastucture/structures/97148/cfa51.cfm>
(accessed September 7, 2018).

[103] Astm, Standard Specification for Coal Fly Ash and Raw or Calcined Natural Pozzolan for Use, 2010.
<https://doi.org/10.1520/C0618>.

[104] V. Berkgaut, A. Singer, High capacity cation exchanger by hydrothermal zeolitization of coal fly ash, *Appl. Clay Sci.* 10 (1996) 369–378.
[https://doi.org/10.1016/0169-1317\(95\)00033-X](https://doi.org/10.1016/0169-1317(95)00033-X).

[105] H. HÖLLER, U. WIRSCHING, Zeolite formation from fly ash, *Fortschritte Der Mineral.* 63 (1985) 21–43.

[106] Z.T. Yao, X.S. Ji, P.K. Sarker, J.H. Tang, L.Q. Ge, M.S. Xia, Y.Q. Xi, A comprehensive review on the applications of coal fly ash, *Earth-Science Rev.* 141 (2015) 105–121.
<https://doi.org/10.1016/j.earscirev.2014.11.016>.

- [107] G.G. Hollman, G. Steenbruggen, M. Janssen-Jurkovičová, Two-step process for the synthesis of zeolites from coal fly ash, *Fuel*. 78 (1999) 1225–1230. [https://doi.org/10.1016/S0016-2361\(99\)00030-7](https://doi.org/10.1016/S0016-2361(99)00030-7).
- [108] N. Murayama, H. Yamamoto, J. Shibata, Mechanism of zeolite synthesis from coal fly ash by alkali hydrothermal reaction, *Int. J. Miner. Process.* 64 (2002) 1–17. [https://doi.org/10.1016/S0301-7516\(01\)00046-1](https://doi.org/10.1016/S0301-7516(01)00046-1).
- [109] S.S. Bukhari, J. Behin, H. Kazemian, S. Rohani, Conversion of coal fly ash to zeolite utilizing microwave and ultrasound energies: A review, *Fuel*. 140 (2015) 250–266. <https://doi.org/10.1016/j.fuel.2014.09.077>.
- [110] O.B. Kotova, I.N.L. Shabalin, D.A. Shushkov, L.S. Kocheva, Hydrothermal synthesis of zeolites from coal fly ash, *Adv. Appl. Ceram.* 115 (2016) 152–157.

<https://doi.org/10.1179/1743676115Y.00000000>

63.

- [111] X. Querol, N. Moreno, A. Alastuey, R. Juan, J.M. Andres, A. Lopez-Soler, C. Ayora, A. Medinaceli, A. Valero, J.M. Andrés, A. López-Soler, C. Ayora, A. Medinaceli, A. Valero, Synthesis of high ion exchange zeolites from coal fly ash, *Geol. Acta.* 5 (2007) 49–57. <https://doi.org/10.1344/105.000000309>.
- [112] N. Shigemoto, H. Hayashi, K. Miyaura, Selective formation of Na-X zeolite from coal fly ash by fusion with sodium hydroxide prior to hydrothermal reaction, *J. Mater. Sci.* 28 (1993) 4781–4786. <https://doi.org/10.1007/BF00414272>.
- [113] S. Rayalu, S.U. Meshram, M.Z. Hasan, Highly crystalline faujasitic zeolites from flyash, *J. Hazard. Mater.* 77 (2000) 123–131. [https://doi.org/10.1016/S0304-3894\(00\)00212-0](https://doi.org/10.1016/S0304-3894(00)00212-0).
- [114] C. Belviso, F. Cavalcante, A. Lettino, S. Fiore,

Zeolite Synthesised from Fused Coal Fly Ash at Low Temperature Using Seawater for Crystallization, *Coal Combust. Gasif. Prod.* 1 (2009) 7–13. <https://doi.org/10.4177/ccgp-d-09-00004.1>.

[115] W. Channabasavaraj, R. Reddy, a Review on Characterization and Application of Fly Ash Zeolites, 07 (2017) 14294–14300. <http://www.journalijdr.com> (accessed September 8, 2018).

[116] P. Kumar, N. Mal, Y. Oumi, K. Yamana, T. Sano, Mesoporous materials prepared using coal fly ash as the silicon and aluminium source, *J. Mater. Chem.* 11 (2001) 3285–3290. <https://doi.org/10.1039/b104810b>.

[117] P.K. Kolay, D.N. Singh, Characterization of an alkali activated lagoon ash and its application for heavy metal retention, *Fuel.* 81 (2002) 483–489. [https://doi.org/10.1016/S0016-2361\(01\)00119-3](https://doi.org/10.1016/S0016-2361(01)00119-3).

[118] M. Inada, Y. Eguchi, N. Enomoto, J. Hojo, Synthesis

- of zeolite from coal fly ashes with different silica-alumina composition, *Fuel*. 84 (2005) 299–304.
<https://doi.org/10.1016/j.fuel.2004.08.012>.
- [119] H. Tanaka, H. Eguchi, S. Fujimoto, R. Hino, Two-step process for synthesis of a single phase Na-A zeolite from coal fly ash by dialysis, *Fuel*. 85 (2006) 1329–1334.
<https://doi.org/10.1016/j.fuel.2005.12.022>.
- [120] K. Fukui, M. Katoh, T. Yamamoto, H. Yoshida, Utilization of NaCl for phillipsite synthesis from fly ash by hydrothermal treatment with microwave heating, *Adv. Powder Technol.* 20 (2009) 35–40.
<https://doi.org/10.1016/j.appt.2008.10.007>.
- [121] S.S. Rayalu, J.S. Udhoji, S.U. Meshram, R.R. Naidu, S. Devotta, Estimation of crystallinity in flyash-based zeolite-A using XRD and IR spectroscopy, *Curr. Sci.* 89 (2005) 2147–2151.
<https://www.jstor.org/stable/24111077> (accessed September 28, 2021).

- [122] S. Jala, D. Goyal, Fly ash as a soil ameliorant for improving crop production - A review, *Bioresour. Technol.* 97 (2006) 1136–1147. <https://doi.org/10.1016/j.biortech.2004.09.004>.
- [123] V. Somerset, L. Petrik, E. Iwuoha, Alkaline hydrothermal conversion of fly ash precipitates into zeolites 3: The removal of mercury and lead ions from wastewater, *J. Environ. Manage.* 87 (2008) 125–131. <https://doi.org/10.1016/j.jenvman.2007.01.033>.
- [124] M. Park, C.L. Choi, W.T. Lim, M.C. Kim, J. Choi, N.H. Heo, Molten-salt method for the synthesis of zeolitic materials I. Zeolite formation in alkaline molten-salt system, *Microporous Mesoporous Mater.* 37 (2000) 81–89. [https://doi.org/10.1016/S1387-1811\(99\)00196-1](https://doi.org/10.1016/S1387-1811(99)00196-1).
- [125] M. Park, C.L. Choi, W.T. Lim, M.C. Kim, J. Choi, N.H. Heo, Molten-salt method for the synthesis of zeolitic materials II. Characterization of zeolitic

- materials, *Microporous Mesoporous Mater.* 37 (2000) 91–98. [https://doi.org/10.1016/S1387-1811\(99\)00195-X](https://doi.org/10.1016/S1387-1811(99)00195-X).
- [126] H.W. Nugteren, N. Moreno, E. Sebastia, X. Querol, Determination of the Available Si and Al from Coal Fly Ashes under Alkaline Conditions with the Aim of Synthesizing Zeolite Products, in: *Int. Ash Util. Symp. Cent. Appl. Energy Res. Univ. Kentucky*, 2001. www.flyash.info.
- [127] V.P. Valtchev, K.N. Bozhilov, Transmission electron microscopy study of the formation of FAU-type zeolite at room temperature, *J. Phys. Chem. B.* 108 (2004) 15587–15598. <https://doi.org/10.1021/jp048341c>.
- [128] K. Sangita, B. Prasad, G. Udayabhanu, Synthesis of zeolite from waste fly ash by using different methods, *Asian J. Chem.* 28 (2016) 1435–1439. <https://doi.org/10.14233/ajchem.2016.19682>.
- [129] P. Koshy, N. Ho, V. Zhong, L. Schreck, S.A. Koszo,

E.J. Severin, C.C. Sorrell, Fly ash utilisation in mullite fabrication: Development of novel percolated mullite, *Minerals*. 11 (2021) 1–17. <https://doi.org/10.3390/min11010084>.

[130] H. Joosten, D. Clarke, Wise use of mires and peatlands -Background and principles including a framework for decision-making, International Mire Conservation Group and International Peat Society, 2002. <http://www.wetlands.org/projects/GPI/default.htm> (accessed September 14, 2018).

[131] World Energy Council (WEC), World Energy Resources: 2013 survey, 2013. <http://www.worldenergy.org>.

[132] I.D. Rotherham, I.D. Rotherham, Global peat resources, in: *Peatlands*, International Peat Society, 2020: pp. 22–33. <https://doi.org/10.4324/9780429439285-3>.

[133] T. Paappanen, A. Leinonen, Peat Industry In The Six

EU Member States – Country Reports, 2010.
http://epagma.eu/sites/default/files/documents/vtt_summary_report_peat_in_eu_2010.pdf
(accessed September 14, 2018).

[134] Sustainable Energy Authority of Ireland, I. Sustainable Energy Authority of, Energy in Ireland 1990-2016, 2017.
<https://www.seai.ie/resources/publications/Energy-in-Ireland-1990-2016-Full-report.pdf> (accessed September 14, 2018).

[135] B.M. Steenari, O. Lindqvist, Fly ash characteristics in co-combustion of wood with coal, oil or peat, *Fuel*. 78 (1999) 479–488.
[https://doi.org/10.1016/S0016-2361\(98\)00177-X](https://doi.org/10.1016/S0016-2361(98)00177-X).

[136] J. Fagerström, I.L. Näzelius, C. Gilbe, D. Boström, M. Öhman, C. Boman, J. Fagerstrom, I.L. Nazelius, C. Gilbe, D. Bostrom, M. Ohman, C. Boman, Influence of Peat Ash Composition on Particle Emissions and Slag Formation in Biomass Grate Co-

combustion, *Energy & Fuels*. 28 (2014) 3403–3411.
<https://doi.org/10.1021/ef4023543>.

- [137] L. Tosheva, A. Brockbank, B. Mihailova, J. Sutula, J. Ludwig, H. Potgieter, J. Verran, Micron- and nanosized FAU-type zeolites from fly ash for antibacterial applications, *J. Mater. Chem.* 22 (2012) 16897–16905.
<https://doi.org/10.1039/c2jm33180b>.
- [138] M.J. Wilson, Clay mineralogical and related characteristics of geophagic materials, *J. Chem. Ecol.* 29 (2003) 1525–1547.
<https://doi.org/10.1023/A:1024262411676>.
- [139] S. Aurèle Douola Ninla, Mineralogical and Physico-Chemical Characterization of Clayey Materials of Meka&a (West Cameroon) Preliminary Step for Their Utilization for Human Ingestion, *Earth Sci.* 7 (2018) 74.
<https://doi.org/10.11648/j.earth.20180702.15>.
- [140] L. Huebl, S. Leick, L. Guetl, G. Akello, R. Kutalek,

Geophagy in northern Uganda: Perspectives from consumers and clinicians, *Am. J. Trop. Med. Hyg.* 95 (2016) 1440–1449. <https://doi.org/10.4269/ajtmh.15-0579>.

[141] D.E. Vermeer, R.E. Ferrell, Nigerian geophagical clay: A traditional antidiarrheal pharmaceutical, *Science* (80-.). 227 (1985) 634–636. <https://doi.org/10.1126/science.3969552>.

[142] J.M. Hunter, Geophagy in Africa and in the United States: A Culture-Nutrition Hypothesis, *Geogr. Rev.* 63 (1973) 170. <https://doi.org/10.2307/213410>.

[143] F. Bergaya, G. Lagaly, General introduction: Clays, clay minerals, and clay science, in: *Dev. Clay Sci.*, 2013: pp. 1–19. <https://doi.org/10.1016/B978-0-08-098258-8.00001-8>.

[144] M.F. Brigatti, E. Galan, B.K.G. Theng, Chapter 2 Structures and Mineralogy of Clay Minerals, *Dev. Clay Sci.* 1 (2006) 19–86.

[https://doi.org/10.1016/S1572-4352\(05\)01002-0](https://doi.org/10.1016/S1572-4352(05)01002-0).

- [145] E.G.I. Ekosse, N.D. Jumbam, Geophagic clays: Their mineralogy, chemistry and possible human health effects, *African J. Biotechnol.* 9 (2010) 6755–6767. <https://doi.org/10.4314/ajb.v9i40>.
- [146] V.B. Yadav, R. Gadi, S. Kalra, Clay based nanocomposites for removal of heavy metals from water: A review, *J. Environ. Manage.* 232 (2019) 803–817. <https://doi.org/10.1016/j.jenvman.2018.11.120>.
- [147] S. Sen Gupta, K.G. Bhattacharyya, Immobilization of Pb(II), Cd(II) and Ni(II) ions on kaolinite and montmorillonite surfaces from aqueous medium, *J. Environ. Manage.* 87 (2008) 46–58. <https://doi.org/10.1016/j.jenvman.2007.01.048>.
- [148] X. Xu, Y. Cheng, X. Wu, P. Fan, R. Song, La(III)-bentonite/chitosan composite: A new type adsorbent for rapid removal of phosphate from water bodies, *Appl. Clay Sci.* 190 (2020) 105547.

<https://doi.org/10.1016/j.clay.2020.105547>.

- [149] M. Vhahangwele, G.W. Mugeru, The potential of ball-milled South African bentonite clay for attenuation of heavy metals from acidic wastewaters: Simultaneous sorption of Co^{2+} , Cu^{2+} , Ni^{2+} , Pb^{2+} , and Zn^{2+} ions, *J. Environ. Chem. Eng.* 3 (2015) 2416–2425. <https://doi.org/10.1016/j.jece.2015.08.016>.
- [150] P.P. Prabhu, B. Prabhu, P.B. Raghuvir, P.P. Prabhu, B. Prabhu, T.M. Mathew, A Review on Removal of Heavy Metal Ions from Waste Water using Natural/ Modified Bentonite, *MATEC Web Conf.* 144 (2018) 02021. <https://doi.org/10.1051/matecconf/201814402021>.
- [151] J.L. Vega, J. Ayala, J. Loreda, J.G. Iglesias, Bentonites as adsorbents of heavy metals ions from mine waste leachates : Experimental data, *9th Int. MINE WATER Congr.* (2005) 603–609.

- [152] K.G. Bhattacharyya, S. Sen Gupta, Adsorption of a few heavy metals on natural and modified kaolinite and montmorillonite: A review, *Adv. Colloid Interface Sci.* 140 (2008) 114–131. <https://doi.org/10.1016/j.cis.2007.12.008>.
- [153] S. Sen Gupta, K.G. Bhattacharyya, Adsorption of heavy metals on kaolinite and montmorillonite: A review, *Phys. Chem. Chem. Phys.* 14 (2012) 6698–6723. <https://doi.org/10.1039/c2cp40093f>.
- [154] Ö. Yavuz, Y. Altunkaynak, F. Güzel, Removal of copper, nickel, cobalt and manganese from aqueous solution by kaolinite, *Water Res.* 37 (2003) 948–952. [https://doi.org/10.1016/S0043-1354\(02\)00409-8](https://doi.org/10.1016/S0043-1354(02)00409-8).
- [155] L. De Pablo, M.L. Chávez, M. Abatal, Adsorption of heavy metals in acid to alkaline environments by montmorillonite and Ca-montmorillonite, *Chem. Eng. J.* 171 (2011) 1276–1286. <https://doi.org/10.1016/j.cej.2011.05.055>.

- [156] J. Matusik, A. Wóscisło, Enhanced heavy metal adsorption on functionalized nanotubular halloysite interlayer grafted with aminoalcohols, *Appl. Clay Sci.* 100 (2014) 50–59. <https://doi.org/10.1016/j.clay.2014.06.034>.
- [157] A. Dyer, Ion exchange capacity, in: H. Robson, K.P.B.T.-V.S. of Z.M. Lillerud (Eds.), *Verif. Synth. Zeolitic Mater.*, Elsevier Science, Amsterdam, 2001: pp. 67–68. <https://doi.org/10.1016/b978-044450703-7/50112-5>.
- [158] M. Asghari, T. Mohammadi, A. Aziznia, M.R. Danayi, S.H. Moosavi, R.F. Alamdari, F. Agand, Preparation and characterization of a thin continuous faujasite membrane on tubular porous mullite support, *Desalination*. 220 (2008) 65–71. <https://doi.org/10.1016/j.desal.2007.01.022>.
- [159] S. Gu, X. Kang, L. Wang, E. Lichtfouse, C. Wang, Clay mineral adsorbents for heavy metal removal from wastewater: a review, *Environ. Chem. Lett.* 17

- (2019) 629–654. <https://doi.org/10.1007/s10311-018-0813-9>.
- [160] K. V Raman, M. Mortland, External Specific Surface Area of Vermiculite, *Am. Mineral.* 51 (1966) 1787–1792.
- [161] M. Warzybok, J. Warchoł, Synthesis of kaolin-based zeolite Y and its application for adsorption of two carbonyl compound gases, *Czas. Inżynierii Lądowej, Środowiska i Archit.* (2018) 13–26. <https://doi.org/10.7862/rb.2018.2>.
- [162] F. Moodi, A.A. Ramezani-pour, A.S. Safavizadeh, Evaluation of the optimal process of thermal activation of kaolins, *Sci. Iran.* 18 (2011) 906–912. <https://doi.org/10.1016/j.scient.2011.07.011>.
- [163] M.J. Mora-Fonz, C.R.A. Catlow, D.W. Lewis, H-Bond interactions between silicates and water during zeolite pre-nucleation, *Phys. Chem. Chem. Phys.* 10 (2008) 6571–6578. <https://doi.org/10.1039/b719632f>.

- [164] Q. Wu, X. Meng, X. Gao, F.S. Xiao, Solvent-Free Synthesis of Zeolites: Mechanism and Utility, *Acc. Chem. Res.* 51 (2018) 1396–1403. <https://doi.org/10.1021/acs.accounts.8b00057>.
- [165] Y.G. Bushuev, G. Sastre, J.V. De Julián-Ortiz, The structural directing role of water and hydroxyl groups in the synthesis of beta zeolite polymorphs, *J. Phys. Chem. C.* 114 (2010) 345–356. <https://doi.org/10.1021/jp907694g>.
- [166] A.Q. Selim, E.A. Mohamed, M.K. Seliem, A.M. Zayed, Synthesis of sole cancrinite phase from raw muscovite: Characterization and optimization, *J. Alloys Compd.* 762 (2018) 653–667. <https://doi.org/10.1016/j.jallcom.2018.05.195>.
- [167] S.M. Seo, D. Kim, D. Kim, J.H. Kim, Y.J. Lee, K.M. Roh, I.M. Kang, A simple synthesis of nitrate cancrinite from natural bentonite, *J. Porous Mater.* 25 (2018) 1561–1565. <https://doi.org/10.1007/s10934-018-0569-4>.

- [168] G.D. Gatta, P. Lotti, Cancrinite-group minerals: Crystal-chemical description and properties under non-ambient conditions - A review, *Am. Mineral.* 101 (2016) 253–265. <https://doi.org/10.2138/am-2016-5282>.
- [169] I. V. Pekov, L. V. Olysyh, N. V. Chukanov, N. V. Zubkova, D.Y. Pushcharovsky, K. V. Van, G. Giester, E. Tillmanns, Crystal chemistry of cancrinite-group minerals with an Ab-type framework: A review and new data. I. chemical and structural variations, *Can. Mineral.* 49 (2011) 1129–1150. <https://doi.org/10.3749/canmin.49.5.1129>.
- [170] P. Zhang, S. Li, C. Zhang, Solvent-free synthesis of nano-cancrinite from rice husk ash, *Biomass Convers. Biorefinery.* 9 (2019) 641–649. <https://doi.org/10.1007/s13399-019-00375-8>.
- [171] N. V Chukanov, S.M. Aksenov, R.K. Rastsvetaeva, Structural chemistry, IR spectroscopy, properties, and genesis of natural and synthetic microporous

cancrinite- and sodalite-related materials: A review, *Microporous Mesoporous Mater.* (2021) 111098.

<https://doi.org/https://doi.org/10.1016/j.micromeso.2021.111098>.

[172] I. Hassan, Feldspathoids and their relationships to zeolites, *Kuwait J. Sci. Eng.* 24 (1997) 163–182.

[173] L.B. Baerlocher, Ch; McCusker, C. Baerlocher, L.B. McCusker, Database of Zeolite Structures, <Http://Www.Iza-Structure.Org/Databases/>. 25 (2019) 2019. <http://www.iza-structure.org/databases/> (accessed January 1, 2021).

[174] S. Cheng, G. Zhang, M. Javed, W. Gao, B. Mazonde, Y. Zhang, C. Lu, R. Yang, C. Xing, Solvent-Free Synthesis of 1D Cancrinite Zeolite for Unexpectedly Improved Gasoline Selectivity, *ChemistrySelect.* 3 (2018) 2115–2119. <https://doi.org/10.1002/slct.201703056>.

- [175] NAT: Main framework image, IZA-SC. (2007).
http://asia.iza-structure.org/IZA-SC/framework_main_image.php?STC=CAN
(accessed February 2, 2022).
- [176] L. Ren, Q. Wu, C. Yang, L. Zhu, C. Li, P. Zhang, H. Zhang, X. Meng, F.S. Xiao, Solvent-free synthesis of zeolites from solid raw materials, *J. Am. Chem. Soc.* 134 (2012) 15173–15176.
<https://doi.org/10.1021/ja3044954>.
- [177] J. Mei, A. Duan, X. Wang, A brief review on solvent-free synthesis of zeolites, *Materials (Basel)*. 14 (2021) 1–13.
<https://doi.org/10.3390/ma14040788>.
- [178] Q. Wu, X. Wang, G. Qi, Q. Guo, S. Pan, X. Meng, J. Xu, F. Deng, F. Fan, Z. Feng, C. Li, S. Maurer, U. Müller, F.S. Xiao, Sustainable synthesis of zeolites without addition of both organotemplates and solvents, *J. Am. Chem. Soc.* 136 (2014) 4019–4025.
<https://doi.org/10.1021/ja500098j>.

- [179] S. Chen, L.P. Sorge, D.K. Seo, Template-free synthesis and structural evolution of discrete hydroxycancrinite zeolite nanorods from high-concentration hydrogels, *Nanoscale*. 9 (2017) 18804–18811.
<https://doi.org/10.1039/c7nr05770a>.
- [180] H. Shao, T.J. Pinnavaia, Synthesis and properties of nanoparticle forms saponite clay, cancrinite zeolite and phase mixtures thereof, *Microporous Mesoporous Mater.* 133 (2010) 10–17.
<https://doi.org/10.1016/j.micromeso.2010.04.002>.
- [181] A. Galarneau, F. Di Renzo, F. Fajula, J. Védrine, Zeolites and mesoporous materials at the dawn of the 21st century: Preface, in: *Stud. Surf. Sci. Catal.*, 2001. [https://doi.org/10.1016/s0167-2991\(01\)81177-0](https://doi.org/10.1016/s0167-2991(01)81177-0).
- [182] C.A.R. Reyes, C. Williams, O.M.C. Alarcón, Nucleation and growth process of sodalite and

cancrinite from kaolinite-rich clay under low-temperature hydrothermal conditions, *Mater. Res.* 16 (2013) 424–438. <https://doi.org/10.1590/S1516-14392013005000010>.

[183] R. Gottipati, S. Mishra, Process optimization of adsorption of Cr(VI) on activated carbons prepared from plant precursors by a two-level full factorial design, *Chem. Eng. J.* 160 (2010) 99–107. <https://doi.org/10.1016/j.cej.2010.03.015>.

[184] E.H. Gürkan, Y. Tibet, S. Çoruh, Application of full factorial design method for optimization of heavy metal release from lead smelting slag, *Sustain.* 13 (2021) 4890. <https://doi.org/10.3390/su13094890>.

[185] B. Velde, Origins and mineralogy of clays: clays and the environment, *Clay Miner.* 1 (1995) 285–287. <https://doi.org/10.1180/claymin.1996.031.2.15>.

[186] S. He, Y. Wang, C. Yang, Y. Li, Z. Zhou, X. Tian,

Potassium cation induced controllable synthesis of CAN zeolite hollow microspheres, *Microporous Mesoporous Mater.* 225 (2016) 365–370. <https://doi.org/10.1016/j.micromeso.2016.01.022>.

[187] J. Yuan, J. Yang, H. Ma, C. Liu, C. Zhao, Hydrothermal synthesis of analcime and hydroxycancrinite from K-feldspar in Na₂SiO₃ solution: Characterization and reaction mechanism, *RSC Adv.* 6 (2016) 54503–54509. <https://doi.org/10.1039/c6ra08080d>.

APPENDICES

Appendix 1 (Paper 1)

Fuel Processing Technology 194 (2019) 106124



Contents lists available at ScienceDirect

Fuel Processing Technology

journal homepage: www.elsevier.com/locate/fuproc



Research article

Waste peat ash mineralogy and transformation to microporous zeolites

Ifeoma V. Joseph, Giulia Roncaglia, Lubomira Tosheva, Aidan M. Doyle*

Department of Natural Sciences, Manchester Metropolitan University, Chester St., Manchester M1 5GD, United Kingdom



ARTICLE INFO

Keywords:
Peat ash utilisation
Zeolite
Pyrolysis
Waste management
Water purification

ABSTRACT

The combustion of peat fuel for industrial scale power generation and domestic heating produces toxic ash, most of which is presently buried in landfill. In this study, the mineralogy of waste peat ash was determined, followed by its successful use as a starting reagent to prepare zeolites. X-ray diffraction (XRD) confirmed the presence of quartz, anhydrite, calcite, lime, merwinite and magnetite in peat ash, and that a single extraction step using mineral acid was sufficient to remove all non-quartz crystal phases. Alkali fusion of the acid-extracted sample produced GIS-type zeolite. LTA- and FAU-type were also prepared by altering the Si/Al ratio and extending the ageing time. Experiments confirmed that the LTA- and FAU-type zeolites were active in the simultaneous adsorption of lead, cadmium, cobalt, zinc and copper from aqueous solutions, with similar quantities of metals removed to those using a reference zeolite.

1. Introduction

Peat is a carbon based material produced from partially decayed vegetation. The deficiencies of oxygen and nutrients in waterlogged bogs and fens (peatlands) limit the decay rate of vegetation such that there is an accumulation of peat over time. These peatlands cover an estimated global area of 4 m km², which equates to 2–3% of the total land area, and are found mainly in Russia, North and South America, Northern Europe and South-East Asia, including lower quantities in locations such as central Africa [1,2]. Peat is classified as an intermediate fuel i.e. between biomass and fossil fuel (lignite). Total global consumption is estimated at 17 m tons per annum, over 99% of which is used in Northern Europe for the production of heat and electricity [3]. Ireland is the largest user, consuming 3.8 m tons annually from peatlands that cover approximately 20% of the national land area [4]. Most of this is used in thermal power plants to generate 8.5% of Ireland's electricity [5,6]. While renewable fuel sources are increasingly being used as a substitute for peat (at least partially in the short term), the production of electricity in Ireland using peat based fuel is an established industry with a secure, indigenous energy source, and will, therefore, continue for the foreseeable future.

Peat ash is the main waste product of combustion at thermal power stations, some of which is disposed of by landfill burial. The alkalinity of peat ash alters the soil quality of the landfill site such that only alkali tolerant plants can grow during the years immediately after disposal. The composition of peat ash varies with location but typically contains a mixture of silicon-, aluminium-, calcium- and iron-containing species,

and a range of toxic elements including arsenic and cadmium [7–10]. While its elemental composition has been well studied, a definitive characterisation of peat ash mineralogy is lacking in the literature. The few papers that discuss peat ash infer crystal phases from (a) elemental composition by scanning electron microscopy/energy-dispersive X-ray spectroscopy (SEM/EDAX) or X-ray fluorescence (XRF) only and/or (b) unseen XRD data; the reader is thus advised to treat such assertions with caution. For example, quartz, microcline, albite and calcium sulfate were reported to be present in peat ash samples, although no XRD results were shown [7,8].

The transformation of peat ash to a useful value-added product with industrial applications would be a significant improvement on the current method of disposal. One such possibility is to use peat ash to prepare zeolites, which are high surface area aluminosilicates widely used for water treatment and purification, humidity control, and heterogeneous catalysis [11]. The combustion of fossil fuels and biomass produces ash residue that contains silicon and aluminum based minerals in appropriate quantities to those used to prepare aluminosilicate zeolites. Coal fly ash has been extensively studied as a zeolite synthesis reagent, and a variety of zeolite architectures were successfully prepared using the alkali fusion method [12–23]. More recently, there are reports showing zeolite preparation using ash from the following renewable biomass sources: rice husk [24–27] eucalyptus bark residue [28], pulp from paper industry [29], sawdust and pine bark [30], bamboo [31] and cogon grass [32].

We now report the mineralogy of peat ash and its successful transformation to pure zeolite using a single stage purification step. To

* Corresponding author.
E-mail address: a.m.doyle@mmu.ac.uk (A.M. Doyle).

<https://doi.org/10.1016/j.fuproc.2019.106124>

Received 13 May 2019; Received in revised form 12 June 2019; Accepted 12 June 2019
0378-3820/© 2019 Elsevier B.V. All rights reserved.

Appendix 2 (Paper 2)

Journal of Environmental Chemical Engineering 8 (2020) 103895



Contents lists available at ScienceDirect

Journal of Environmental Chemical Engineering

journal homepage: www.elsevier.com/locate/jeece



Simultaneous removal of Cd(II), Co(II), Cu(II), Pb(II), and Zn(II) ions from aqueous solutions via adsorption on FAU-type zeolites prepared from coal fly ash



Ifeoma V. Joseph*, Lubomira Tosheva, Aidan M. Doyle

Department of Natural Sciences, Manchester Metropolitan University, Chester Street, Manchester M1 5GD, United Kingdom

ARTICLE INFO

Editor: Depo Kamion.
Keywords:
Heavy metals
Adsorption isotherm
Fly ash
Zeolite
pseudo second order
Coal fly ash

ABSTRACT

This study reports the potential for the simultaneous removal of Cd(II), Co(II), Cu(II), Pb(II), and Zn(II) ions from aqueous solutions by FAU-type zeolites prepared from coal fly ash. The zeolite synthesis route was via alkaline fusion followed by the addition of deionised water and hydrothermal treatment using fly ash to water mass ratios of 4, 10, 15, and 20. XRD, XRF, SEM and N₂ adsorption measurements were used to characterize the prepared zeolites. Adsorption experiments were carried out for variations in concentration, time, and adsorbent loading. The adsorption process followed pseudo second-order kinetics and Langmuir adsorption isotherm; intra particle diffusion model fitting indicated that diffusion within the pores affected the rate controlling steps and mass transfer across boundary layers for the adsorbate – adsorbent system. The efficacy of FAU – type zeolite for the binary-metal ions adsorption studied decreased in the order Pb(II) > Cu(II) > Zn(II) > Co(II).

1. Introduction

The release, accidental or premeditated, of toxic metals to the environment as a result of industrialization continues to be a cause for global concern due to the impact on the environment and the health of living organisms [1]. For instance, trace amounts of metals like copper, iron, and zinc are essential for metabolism in all living organisms; excess amounts of these essential metals are capable of overwhelming the homeostatic mechanism, i.e. the ability to regulate complex metabolic equilibria, of an organism [2,3]. The toxicity of cadmium, cobalt, copper, lead, and zinc vary. While some are lethal even in small concentrations, others are lethal from bioaccumulation; toxic effects arise from disruption of the nervous system to carcinogenic potentials [4–6].

Adsorption is one of the effective means of the removal of these toxic metals in solutions via the use of adsorbents [5–7]. As far back as 1884, when Venable collected rudimentary data on zinc contamination [8], advances have been made in the detection, quantification, and removal of toxic metals from drinking water. Among a plethora of inorganic waste materials for purifying water contaminated with toxic metals, coal fly ash and zeolites prepared from coal fly ash have been widely used [9–14]. There is an appreciable amount of literature available on the preparation of synthetic zeolites from coal fly ash [12–18].

Coal fly ash, powdered particulate matter generated as a

combustion by-product in thermal power stations that utilize pulverised coal, is mainly composed of oxides of silicon and aluminium. Pulverised coal is fed into dry bottom boilers, most commonly used in thermal power stations, and approximately 80 % of all its ash is fly ash conveyed by flue gases [19]. In accordance with ASTM G618, fly ash falls into two broad classes – C and F [20]. This classification is based on the total amount of oxides of silicon, aluminium, and iron present. Class C fly ash is obtained from the combustion of geologically younger sub-bituminous or lignite coal while class F is obtained from much older bituminous or anthracite coal. According to ASTM G618 classification, the sum of SiO₂, Al₂O₃, and Fe₂O₃ is up to 50 % for class C and 70 % for class F [20]. The chemical composition of coal fly ash (CFA) varies with geographical location and the coal source but the commonality is the predominance of SiO₂ and Al₂O₃. The phases in fly ash typically include crystalline structures like mullite, hematite, magnetite, and quartz [1,16].

Due to the close semblance in terms of composition of CFA to volcanic materials, fly ash can be used to synthesize zeolites. Zeolites are 3D aluminosilicate frameworks with porous crystalline structures that have wide ranging usage in the fields of adsorption, catalysis, and ion exchange [18,21–26]. Zeolite types from CFA include Linde type A zeolite (LTA), FAU-types (zeolite X, Y), zeolite P, and chabazite [1,14,27–29]. To synthesize zeolites from CFA, the conventional methods involve the use of alkaline solutions to dissolve the varied

* Corresponding author.

E-mail address: i.joseph@mmu.ac.uk (I.V. Joseph).

<https://doi.org/10.1016/j.jeece.2020.103895>

Received 5 December 2019; Received in revised form 12 March 2020; Accepted 23 March 2020

Available online 27 March 2020



2213-3437/© 2020 Elsevier Ltd. All rights reserved.

Appendix 3 (Paper 3)



Article

FAU—Type Zeolite Synthesis from Clays and Its Use for the Simultaneous Adsorption of Five Divalent Metals from Aqueous Solutions

Ifeoma V. Joseph , Lubomira Tosheva , Gary Miller and Aidan M. Doyle

Department of Natural Sciences, Manchester Metropolitan University, Chester Street, Manchester M1 5GD, UK; g.miller@mmu.ac.uk (G.M.); a.m.doyle@mmu.ac.uk (A.M.D.)

* Correspondence: i.joseph@mmu.ac.uk (I.V.); l.tosheva@mmu.ac.uk (L.T.)

Abstract: In this research, a vermiculite-kaolinite clay (VK) was used to prepare faujasite zeolites via alkaline fusion and hydrothermal crystallisation. The optimal synthesis conditions were 1 h fusion with NaOH at 800 °C, addition of deionised water to the fused sample at a sample to deionised water mass ratio of 1:5, 68 h of non-agitated ageing of the suspension, and 24 h of hydrothermal treatment at 90 °C. The efficacy of the prepared faujasite was compared to raw clay and a reference zeolite material through adsorption experiments of aqueous solutions containing five divalent cations—Cd, Co, Cu, Pb, and Zn. The results showed that in the presence of competing cations at concentrations of 300 mg L⁻¹ and adsorbent loading of 5 g L⁻¹, within the first 10 min, about 99% of Pb, 60% of Cu, 58% of Cd, 28% of Zn, and 19% of Co were removed by the faujasite prepared from clay. Two to four parameter nonlinear adsorption isotherms were used to fit the adsorption data and it was found that overall, three and four parameter isotherms had the best fit for the adsorption process.

Keywords: clay; faujasite; adsorption; nonlinear isotherm; heavy metals; zeolite synthesis



Citation: Joseph, I.V.; Tosheva, L.; Miller, G.; Dyk, A.M. FAU—Type Zeolite Synthesis from Clays and Its Use for the Simultaneous Adsorption of Five Divalent Metals from Aqueous Solutions. *Materials* 2021, 14, 3738. <https://doi.org/10.3390/ma14133738>

Academic Editors: Miquel A. Cambor and Soenra Espósito

Received: 29 April 2021

Accepted: 30 June 2021

Published: 3 July 2021

Publisher's Note: MDPI stays neutral with regard to jurisdictional claims in published maps and institutional affiliations.



Copyright © 2021 by the authors. Licensee MDPI, Basel, Switzerland. This article is an open access article distributed under the terms and conditions of the Creative Commons Attribution (CC BY) license (<https://creativecommons.org/licenses/by/4.0/>).

1. Introduction

Clay minerals, ubiquitous to environments with sediments, are phyllosilicates from sedimentary and weathering formations. Two-dimensional layers of tetrahedral (SiO₄) and octahedral (AlO₆) structural sheets characterise them. A 1:1 layer arrangement indicates repeating single tetrahedral and octahedral units found in kaolinites, while 2:1 arrangement represents two tetrahedral units for each octahedral unit found in smectites (montmorillonites), vermiculite, and illites [1–3]. The reported mineralogy of clays include calcites, smectites, illites, kaolinites, halloysites, quartz, feldspar, and montmorillonite [1,2]. There is an appreciable literature on the use of clays like bentonite [3–5], kaolinite [7–9], montmorillonite [7,8,10], halloysite [11,12], and clay composites [7,13,14] for the removal of heavy metals in aqueous solutions. Due to their abundance in nature, these clays offer cheaper alternatives in purifying water contaminated with heavy metals. Such metals in drinking water can cause debilitating and sometimes terminal conditions.

Clay minerals are predominantly composed of aluminosilicates, which suggests that they may be suitable raw materials for zeolite syntheses. Faujasite (FAU) zeolites, hydrated aluminosilicates used as molecular sieves or ion exchange media [15–17], have been prepared for applications ranging from the adsorption of gases [18] to catalysis and the removal of pollutants in water [19–23]. The synthesis of faujasite zeolites has been reported for clays such as illite [23,24], kaolin [25,26], and montmorillonite [24]. The prevalent synthesis method is the pre-alkaline fusion with hydrothermal treatment, factors that influence the synthesis include the alkaline concentration and the ratio of liquid to solid in the precursor [24].

This study investigates the synthesis of faujasite zeolite adsorbents from vermiculite-kaolinite clays via alkaline fusion and hydrothermal treatment and its application in the